

Surface Nanoscale Axial Photonics (SNAP) for Optofluidics

Tabassom Hamidfar

A Thesis
In the Department
of
Physics

Presented in Partial Fulfillment of the Requirements
For the Degree of
Doctor of Philosophy (Physics) at
Concordia University
Montréal, Québec, Canada

December 2018

© Tabassom Hamidfar, 2018

**CONCORDIA UNIVERSITY
SCHOOL OF GRADUATE STUDIES**

This is to certify that the thesis prepared

By: Tabassom Hamidfar

Entitled: Surface Nanoscale Axial Photonics (SNAP) for Optofluidics

and submitted in partial fulfilment of the requirements for the degree of

Doctor of Philosophy (Physics)

complies with the regulations of the University and meets the accepted standards with respect to originality and quality.

Signed by the final examining committee:

_____	Chair
Dr. Chantal David	
_____	External Examiner
Dr. Claudine Allen	
_____	External to Program
Dr. John Xiupu Zhang	
_____	Examiner
Dr. Lazlo Kalman	
_____	Examiner
Dr. Christophe Grova	
_____	Supervisor
Dr. Pablo Bianucci	

Approved by _____
Dr. Valter Zazubovits, Graduate Program Director

February 5, 2019 _____
Dr. André Roy, Dean
Faculty of Arts and Science

ABSTRACT

Surface Nanoscale Axial Photonics (SNAP) for Optofluidics

Tabassom Hamidfar, Ph.D.

Concordia University, 2018

Sensing with optical whispering gallery modes (WGMs) is a rapidly developing detection method in modern microfluidics research. This method explores the perturbations of spectra of WGMs propagating along the wall of an optical microresonator to characterize the liquid medium inside it. Out of the many available types of WGM microresonators, the surface nanoscale axial photonics (SNAP) platform enables fabrication of resonant ultralow loss photonics structures at the surface of an optical fiber with unprecedented precision currently approaching 0.1 angstroms.

In this work, first we explore a new technique for the creation of SNAPs, by using a regular hydrogen-oxygen torch, which requires less equipment than current techniques. The transmission spectra shows that light can be fully localized by pulling a fiber, with very low loss resonant modes. We then present the first demonstration of a platform with potential for microfluidic sensing based on SNAP microresonators fabricated in silica capillary fiber with ultra-thin walls by local annealing with a focused CO_2 laser and internal etching with hydrofluoric acid. This demonstration paves the groundwork for advanced microfluidic sensing with SNAP microresonators.

Finally, we show that light circulating in a silica microcapillary can be fully localized by evanescent coupling to a water droplet forming a high Q-factor microresonator. The discovered phenomenon suggests a novel method for microfluidics sensing and a new type of tunable resonant microfluidic-based photonic devices.

Acknowledgements

PhD is not about getting a degree, it is a journey; it is like a long hiking trail that is full of sceneries. It has lots of ups and downs, but teaches you how to overcome the challenges in life. It teaches you perseverance. It teaches you as long as you put one foot in front of the other foot, you are getting somewhere and it is the life. You can not finish this hiking trail without the support of people. First and foremost, I would like to express my deepest gratitude to my supervisor, Prof. Pablo Bianucci for his guidance and support throughout the course of this project. His patience, enthusiasm, and encouragement fueled my motivation and pushed me farther than I thought I could go. Thank you for trusting me and giving me the opportunity to be the first member of your group. I have learned a lot from you.

I am extremely grateful to Prof. Misha Sumetskey, for accepting me in his lab at Aston Institute of Photonics Technologies (AIPT), Birmingham, UK. I much appreciate all his help, kind support, and his gracious hospitality during my visit to Aston. Working with him was great. I am also indebted to Dr. Artemiy Dmitriev, Dr. Kirill Tokmakov, and Dr. Dashiell Vitullo for their technical support and assistance in the experimental work at AIPT. Sincere thanks to Dr. Brian Mangan, and Dr. Robert Windeler, from OFS Laboratories, USA, for providing technical equipment, and insightful comments on this project.

I would like to thank all my fellow research group members, Kathleen, Mathieu, Rajni, and Amalia, for making my experience at Concordia pleasant and cheerful. A special thank you to Tugba who was always a great friend. Many thanks to Marie-Anne Cheong Youne for her kindness and assistance with departmental matters.

My special thanks to my husband and best friend, Amir, for his endless love and encouragement. His valuable suggestions and priceless support have been very important to me. Thank you for making each day better than the last. Finally, I am thankful to my parents, Parvin and Abbas, and my lovely little brother, Toumaj, for supporting me at all times. It was so hard being thousands of kilometers away from you all these years.

I would like to the gratefully acknowledge the financial support of the Concordia University through the J.W. McConnell Memorial Graduate Fellowship, and Lorraine Gosselin Scholarship. Financial support during my visit from AIPT was provided in part by Concordia Graduate Mobility Award and Aston University.

To my parents and to Amir, my husband...

Contents

List of Figures	ix
List of Tables	xiii
List of Abbreviations	xiv
1 Chapter 1: Introduction	1
1.1 Dissertation Organization	8
2 Chapter 2: Surface Nanoscale Axial Photonics (SNAP)	10
2.1 Background	10
2.1.1 Optical Whispering Gallery Modes	10
2.1.2 Free spectral range	12
2.1.3 Quality factor	12
2.1.4 Maxwell's equations	14
2.2 Surface Nanoscale Axial Photonics (SNAP)	15
2.3 Step-Profile Fiber	16
2.4 Quantum Analogy	21
2.4.1 Analogy of guided optical modes and quantum mechanics	21
2.4.1.1 Guided optical waves - Helmholtz equation	21
2.4.1.2 Quantum mechanics - Time-independent Schrödinger equation	22
2.4.2 SNAP theory	24
2.4.2.1 "Quantum theory" of light in SNAP devices	29
2.5 Coupling light	31
2.6 Current Fabrication Methods of SNAP	32
2.7 SNAP Spectrogram	34
3 Chapter 3: SNAP induced by pulling a fiber	37
3.1 Fabrication	38
3.2 Characterization	39
3.3 Results	42
3.4 Summary	49

4 Chapter 4: SNAP at a capillary fiber	50
4.1 Fabrication	51
4.1.1 Fabrication of the micro-capillary	51
4.1.2 Fabrication of the tapered fiber	52
4.1.3 Fabrication of SNAP microresonator	53
4.2 Characterization	53
4.3 Etching	54
4.4 Results	56
4.5 Summary	62
5 Chapter 5: Localization of light in an optical microcapillary induced by a droplet	64
5.1 Observation of an Optical Microresonator Induced by a Droplet	65
5.2 Theory of Cutoff Wavelengths and Quantization of Slow WGMs	68
5.3 Interpretation of the Experimental Observations	74
5.4 Evaporation of the Droplet and Concomitant Effects	77
5.5 Summary	80
6 Chapter 6: Conclusions and Outlook	82
Bibliography	84
Appendix A Data Collecting	95
Appendix B Data Processing	99
B.1 extract-intensity-to-matrix.py	99
B.2 concatenate-two-matrix.py	101
B.3 Mathematica script	102
Appendix C Supporting Content	104
C.1 Expanded Experimental Data and Processing Details	104
C.2 Semiclassical Quantization Rule For WGMs in the Droplet-Induced Microresonator	107

List of Figures

1.1	a. Speed in free space or optical fiber. b. Speed in photonic circuit. c. Different photonic circuits used in slowing light [44].	4
1.2	Illustration of SNAP slow light [44].	5
1.3	An optical biosensor based on a straight waveguide (left) and one based on a WGM (right).	6
1.4	a. A SNAP Sensor. b. WGM shifts from λ_1 to λ_2 in response to binding of the target biomolecules to SNAP capillary microresonator interior surface [57].	7
2.1	Whispering Gallery Mode (WGM) propagation inside a cavity.	11
2.2	Different types of WGM resonators, a. Silica microsphere whispering gallery resonators [11]. b. Microtoroid resonators [11]. c. Microring resonators [11]. d. Microdisk resonators [11].	11
2.3	Definition of quality factor of mode.	12
2.4	Typical transmission spectrum of a 22 μm SNAP microresonator.	14
2.5	Schematic of a hollow Surface Nanoscale Axial Photonics (SNAP) device.	16
2.6	Section of a step-profile fiber. $n(\rho)$ is the refractive index profile and ρ is radius of the core.	17
2.7	Index profile of a step-index fiber.	17
2.8	Solution of the 1D Helmholtz equation for a step-index dielectric waveguide.	22
2.9	Time-independent Schrödinger solution in one-dimension.	23
2.10	SNAP devices, a. WGM bottle microresonator [28]. b. Concave fiber waist [28]. c. Monotonic variation of fiber radius [28].	30
2.11	Coupling of the light from a microfiber (MF) to a hollow SNAP resonator.	31
2.12	Spectra of a SNAP resonator, at different range of wavelength. a. $\Delta\lambda = 86.13nm$. b. $\Delta\lambda = 10.26nm$. c. $\Delta\lambda = 2.55nm$	32
2.13	a. First fabrication method of SNAP device with IR (CO_2 laser) beam exposure [30]. b. Second fabrication method of SNAP devices with UV beam exposure [30].	33
2.14	Third fabrication method of SNAP device with femtosecond laser [34].	34
2.15	A schematic of characterization of SNAP with sub-angstrom precision.	35
2.16	a. An example of collecting the spectrum at several points along the fiber. b. corresponding SNAP spectrogram in 2D.	36
3.1	Optical microscopic image of a microfiber.	38
3.2	An optical microscopic image of an optical fiber with radius of 125 μm and a tapered fiber.	38

3.3	Position spectrogram of a fiber after mechanical stripping and cleaning, before any further processing.	39
3.4	Overview of the SNAP microresonator characterization station. Details are given in Table 3.1.	40
3.5	A schematic of the characterization set-up of a SNAP device.	40
3.6	An optical microscopic image of a typical our microresonator with radius of $\sim 20 \mu m$ and a tapered fiber.	42
3.7	Optical microscopy images captured from the video (https://youtu.be/N0ghwZeIm8Q) recorded during scanning a SNAP resonator with a microfiber from wavelength $935.5 nm$ to $920.5 nm$ at $0.6 nm/s$ a. 18 sec, and b. 24 sec.	43
3.8	Position spectrograms along $7 mm$ of the pulled fiber before passing the torch. The spatial resolutions of the scans was $10 \mu m$	44
3.9	Position spectrograms along $7 mm$ of the pulled fiber after extra annealing. The spatial resolutions of the scans was $10 \mu m$	45
3.10	a-b. Optical microscope image of the pulled fiber and a tapered fiber before passing the torch and after extra annealing, respectively. The thin black arrows in Figure 3.8 and 3.9 indicate the position corresponding to each image.	45
3.11	Normalized transmission response of the fabricated SNAP at its central position.	46
3.12	Magnified spectral region of the spectrum plot showing a single group of modes.	46
3.13	Detail of the resonance of the mode indicated by the red ellipse in Figure 3.12.	47
3.14	Transmission spectra for different separations between the resonator and tapered fiber. The gap decreases in the upward direction, and the top spectrum corresponds to the resonator and microfiber being in physical contact. The red arrow indicates the trace closest to critical coupling.	48
4.1	Scanning $7.5mm$ of surface of the capillary with a tapered fiber.	52
4.2	A schematic of fabrication method of SNAP with CO_2 laser beam.	52
4.3	Surface plot of spectra of the fabricated SNAP resonator measured with $20\mu m$ resolution along the capillary axis [105].	54
4.4	The surface plots of the transmission power spectra show the effect of power of laser on the surface of a capillary. a. Four SNAP resonators is produced with the laser power of 15%, 16%, 14%, and 13%. They have the same radiation time= $0.5s$, the relaxation time= $10s$, and the distance between each position of pulse= $70\mu m$. b. The power of laser was higher than the melting temperature of silica, the surface of capillary is deformed.	54
4.5	Typical glass transition volume-temperature dependence, t_{gs} is the glass transition temperature for slow cooling, t_{gf} corresponds to the glass transition temperature for fast cooling, and t_m is the melting temperature. Figure is from [106].	55
4.6	The optical microscope image of the cross-section of the silica microcapillary used in the experiment.	55
4.7	Overview of etching process. Details are given in Table 4.1.	56
4.8	A schematic of etching process.	57
4.9	Surface plots of spectra of the fabricated SNAP microresonator measured with $20\mu m$ resolution along the capillary axis. a. After etching, empty capillary, $P = 0$ (bottom) and $P = 1$ (top). b. After etching, capillary filled with water, $P = 0$ (bottom) and $P = 1$ (top) [104].	58

4.10	Illustration of a capillary fiber coupled to an input-output microfiber. The capillary is processed with a CO_2 laser beam and, internally, with hydrofluoric acid. Inset: magnified cross section of the capillary wall (not to scale) [104].	59
4.11	Surface plots of spectra of the fabricated SNAP microresonator. a. After etching, empty capillary, showing fundamental $P = 0$ radial series. b. After etching, capillary filled with water, showing the fundamental $P = 0$ radial series [105]. . .	60
4.12	a. Cutoff wavelength as a function of internal ERV for the quantum numbers indicated on the plot. b. Dependencies shown in (a) magnified and shifted along the vertical axis [104].	60
4.13	a. Cutoff wavelength as a function of internal ERV for the empty and water-filled capillaries for the quantum numbers indicated on the plot. b. Dependencies shown in 4.13(a) magnified and shifted along the vertical axis. Curves shown in 4.12(b) and 4.13(b) are compared by horizontal translation into the darker rectangles. [104].	61
4.14	a. Parabolic approximation of the cutoff wavelength for the empty (black curve) and water-filled (blue curve) capillary. Dashed red curve is the difference of these curves. b. The restored internal ERV. The solid, dashed, and dotted curves correspond to $\lambda_w - \lambda_e$ equal to 0.05 nm , 0.04 nm , and 0.06 nm , respectively [104].	62
5.1	The optical microscope image of the cross section of the silica microcapillary used in the experiment. This image was used to determine the radius of the capillary and the thickness of its wall.	66
5.2	The optical microscope image of a water droplet inside the capillary. The droplet meniscuses caused by the surface tension are clearly seen.	66
5.3	Illustration of the experiment. The input-output taper with a micron-diameter waist (microfiber) is positioned normally to the capillary. The microfiber excites WGMs which propagate along the microcapillary wall and sense the droplet. . .	67
5.4	a. Surface plot of the transmission power spectra collected by the input-output microfiber translated along the microcapillary with a droplet inside. The spectral (vertical axis) and spatial (horizontal axis) resolutions of the scan were 1.3 pm and $2 \text{ }\mu\text{m}$, respectively. The central part of the plot indicates the region where the droplet was situated. b. and c. Surface plots of the calculated transmission power spectra corresponding to the stationary droplet with the initial (b) and final (c) dimensions which were obtained for a single cutoff wavelength using Eqs. 5.2-5.4. The initial and final dimensions were taken from the experimental plot (a) at axial coordinates z_1 and z_2 [Fig. 5.3] when the measurement of the droplet region started and finished.	68
5.5	Cutoff wavelengths with the azimuthal quantum number $m = 364$ and radial quantum numbers $p = 0, 1, 2, 3, 4, 5$ for the silica microcapillary with external radius $r_{ext} = 68 \text{ }\mu\text{m}$ as a function of the microcapillary internal radius r_{int} . The solid and dashed curves correspond to the empty and water-filled microcapillary, respectively.	70
5.6	The distribution of cutoff wavelengths (dots) for the TE-polarized WGMs having $p = 0, 1, 2, 3, 4, 5$ in the bandwidth $1540 \text{ nm} < \lambda < 1550 \text{ nm}$. The corresponding azimuthal quantum numbers m are shown next to each of the dots.	71

5.7	A sample surface plot of transmission power spectra calculated using Eqs. 5.2, 5.3, and 5.4 for the water-induced shift of the cutoff wavelength equal to 1 nm and microfiber-capillary coupling parameters indicated in the text.	73
5.8	a.-c. Magnified spectral region of the surface plot 5.4(a) and the theoretical models of the droplet similar to those shown in 5.4(b) and 5.4(c) but for a different cutoff wavelength.	75
5.9	The resonance of the droplet-induced microresonator measured at the node indicated at the spectral plot 5.8(a).	76
5.10	Magnified spectral region of the surface plot 5.8(a) containing the pathway of resonances with the axial quantum number $q = 12$ which was used for the analysis of the droplet evaporation.	77
C.1	The surface plot of the transmission power spectra in the bandwidth from 1539 nm to 1549 nm . The spectral (vertical axis) and spatial (horizontal axis) resolutions of the scan were 1.3 pm and $2\text{ }\mu\text{m}$, respectively.	105
C.2	Illustration of matching the theoretical and experimental data. The width of the resonator is determined by the comparison of single resonance pathways. The height of the resonator is determined by fitting the positions of all eigenvalues corresponding to the selected cutoff wavelength.	106

List of Tables

1.1	SNAP vs. photonic technologies developed previously [29, 35–37]	3
2.1	The guided optical waves and Quantum mechanics	24
3.1	Components of characterization system	41
3.2	Resonator properties	44
4.1	Components of the etching set-up	56

List of Abbreviations

1D	One Dimension
2D	Two Dimensions
AFM	Atomic Force Microscopy
CO₂	Carbon Dioxide
FSR	Free Spectral Range
FWHM	Full Width Half Maximum
HE or EH	Hybrid Mode
HF	Hydrofluoric Acid
IR	Infrared
MF	Micro Fiber
OSA	Optical Spectrum Analyzer
Q	Quality Factor
SEM	Scanning Electron Microscopy
SMF	Single Mode Fiber
SNAP	Surface Nanoscale Axial Photonics
TE	Transverse Electric
TEM	Transmission Electron Microscopy
TF	Tapered Fiber
TM	Transverse Magnetic
UV	Ultraviolet
WGM	Whispering Gallery Modes

Chapter 1

Introduction

Optical microresonators have been receiving considerable attention, owing to their remarkable optical properties. Because of the optical confinement at the microscale, there is an enhancement of the electromagnetic field inside the resonator which has led to the straightforward observation of high quality factor resonances in the spectra. This makes them suitable for technological applications in various fields such as photonics and biosensing.

Micro-scale optical microresonators based on whispering galley modes (WGMs) are dielectric structures that confine light through total internal reflection. Thanks to their low losses, they show high enhancement of their internal fields [1]. Research and development of them has grown significantly over the last several decades finding applications in telecommunications [2–5], fabrication of microlasers [6–10], quantum electrodynamics [11, 12], quantum networks [13, 14], microfluidics [15–18], optomechanics [19, 20], and other fields of science and engineering. These microresonators are usually fabricated in the form of spheres, toroids, bottles, bubbles, cylinders, disks, and capillaries (see e.g., Refs [2, 3, 11, 15, 21]).

Similar to the acoustic WGMs, optical WGMs propagate very close to the surface of optical microresonators. This fact has both positive and negative consequences for applications. On the one hand, since WGMs are isolated from the microresonator core, thermal and electrical tuning devices can be included into interior part of the microresonator without degrading its quality factor [22, 23]. Of special interest is the development of microfluidic optomechanics based on

liquid-filled microcapillaries, which is also based on the effect of isolation of WGMs from the liquid inside the resonator [24, 25].


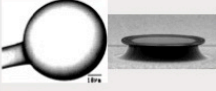

Alternatively, coupling between WGMs and the interior of the microresonator is critical for the development of ultra-precise capillary microfluidic sensors [15, 18, 26, 27]. Researchers fabricate optical microcapillaries having very narrow (a few microns thick) walls, which allow WGMs to evanescently penetrate through the internal capillary surface and probe the interior medium. It is expected that these microfluidic sensors, similar to WGM microresonators sensing the environment at their peripheral surface [16], can achieve breakthrough single-molecule sensitivity.

Out of the many available types of WGM microresonators, the **surface nanoscale axial photonics (SNAP)** platform enables fabrication of resonant photonic structures at the surface of an optical fiber with unprecedented precision currently approaching 0.1 angstroms [28]. The idea of SNAP consists in exploring whispering gallery modes (WGMs) which slowly propagate along the surface of an optical fiber. For this reason, these modes are slow and their axial speed and propagation constant are small. As a result, the distribution of light propagating in the form of a WGM along an optical fiber surface can be fully controlled by the exceptionally small nanoscale variation of the effective fiber radius [29].

In this case of a capillary fiber, it is of great interest to investigate how the spatial and temporal variation of the media adjacent to the internal capillary surface affect the spectrum of the SNAP resonator created at the capillary wall. In particular, it is important to find out if it is possible to determine the internal effective radius variation of the capillary from the measure spectra, as was done for the outer radius in SNAP [30].

The idea of producing SNAP devices was first published by M. Sumetsky and J. M. Fini in 2011 [28, 31]. A SNAP resonator confines light by means of an effective radius variation (ERV) in a cylindrically symmetric dielectric structure. The effective radius is defined as the product of the radius of the structure and the refractive index of the material, $r_{eff}(z) = r(z)n(z)$, where r is the radius of the structure and n its refractive index. Thus, an ERV can be introduced in an optical fiber by causing a change in either its radius or its refractive index. The ERVs needed to produce good optical confinement are on the order of tens of nanometers. They initially demonstrated two methods of fabrication based on the modification of an ERV for a variety of glass and photosensitive fibers with CO₂ laser treatment [30] and UV beam exposures

TABLE 1.1: SNAP vs. photonic technologies developed previously [29,35–37]

Platform	illustration	Dimension of elements	Propagation loss	Fabrication accuracy
Photonic crystals		1 μm	0.01 dB/cm	10 nm
Silica micro resonator		10 μm	0.0001 dB/cm	100 nm
Surface nanoscale axial photonics		10 μm	0.0001 dB/cm	0.1 nm

[32], which we explain them in detail in the next chapter. Recently, using a CO₂ laser, more sophisticated structures such as resonators with parabolic and semi-parabolic profiles [4] have been demonstrated. It has also been discovered lately that light confinement can be induced temporarily in silica capillaries through joule heating of a specially patterned metal wire inside [33], or using femtosecond laser pulses [34].

SNAP devices are particularly interesting because of their low optical losses. They are made of silica, which has low absorption and a smooth surface that reduces the scattering of light. Table 1.1 summarizes the properties of SNAP devices as compared to prior photonic devices. The advantages of a SNAP device include attributes such as robust whispering gallery modes which are localized inside of the fiber and properties of silica such as roughness of the surface and low material losses. Moreover, because of the micrometer dimensions and low attenuation coefficients of SNAP, these photonic devices can be considered as a suitable platform for miniature integrated photonic circuits.

The characteristic dimensions of individual SNAP elements can potentially be as small as $10\mu\text{m}$. While dimensions of this scale are equal to or greater than the dimensions of previous devices, such as silica microresonators or photonic crystals, the propagation loss of SNAP devices can be up to two orders of magnitude smaller than that of those devices. Also, the fabrication accuracy of SNAP devices can be significantly better than previous technologies.

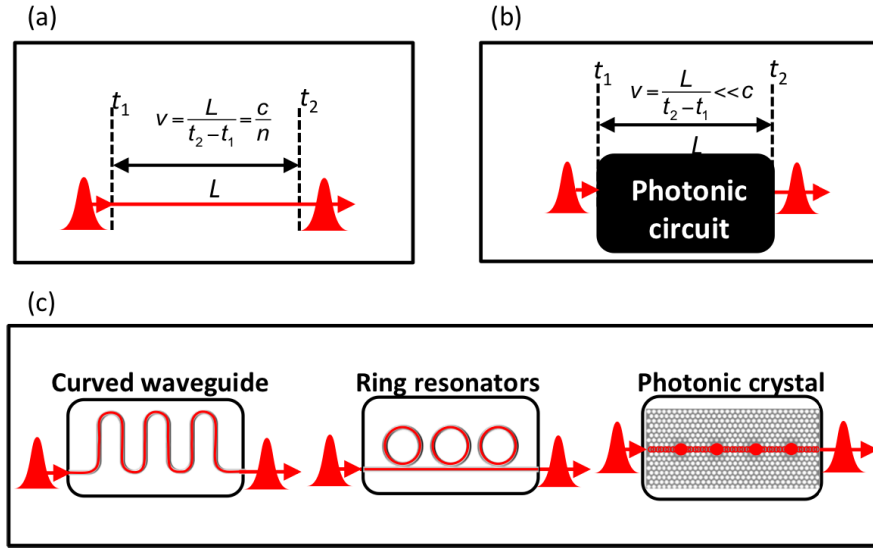


FIGURE 1.1: **a.** Speed in free space or optical fiber. **b.** Speed in photonic circuit. **c.** Different photonic circuits used in slowing light [44].

Due to the flexibility and ultra-low loss of SNAP platforms, which lead to the creation of high-quality WGM microresonators, they show great promise as photonic micro-devices in many applications like switching, filtering, lasing, sensing with high precision, slow light delay lines [38], buffers and signal processors [39], frequency comb generators [40], and optomechanical devices [41]. These structures could also be used to investigate Anderson localization [42] and tunneling [43] in optical contexts. The main potential applications of the SNAP platform include:

Slow light

SNAP can be better than any other slow light devices previously suggested [44]. First of all, we define slow light as: when a regular pulse propagates in the free space of an optical fiber, the speed is determined by the speed of light c divided by refractive index n , as shown in Figure 1.1(a). We can make effectively the speed of light smaller. Of course, we can not change the fundamental constant c , but photonic circuits that slow down light can be created. The size of the photonic circuit is small, so that the the speed of light is determined by the size L divided by the time light spend in this photonic circuit (see Figure 1.1(b)). Several examples of this circuits

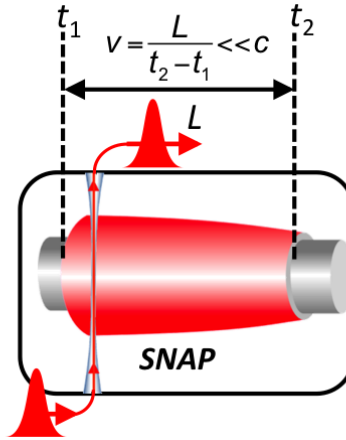


FIGURE 1.2: Illustration of SNAP slow light [44].

are shown in Figure 1.1(c) [45]. We can curve the waveguide and of course the effective speed of light is smaller because it has to cover a long distance there. We can use a ring resonator for the same reason, and also we can use photonics crystals. Scientists are very interested in this technology, because by using these approaches they can create very small different optical devices such as optical delay lines, photonics sensors, microfluidic sensors, and so.

But the problem is that technology is still not precise enough and dispersion, bandwidth, and loss of light are factors limiting the use of these slow light devices [46]. Thus, about 10 years ago, scientists understood these approaches are not satisfactory and the interest on slow light decreased significantly. Instead, SNAP can be suggested as a new approach [4]. While the fabrication precision of a SNAP platform is two order of magnitude more precise than that with other achieved technologies, the transmission loss of SNAP fibers is two orders of magnitude smaller than any other microphotonic technology developed to date.

Sensing with high precision

Optical WGMs microresonators in the form of microspheres [26, 47], microbubble [48, 49], microrings [50, 51], or microdisks [37, 52] are an emerging biological or chemical sensing technology

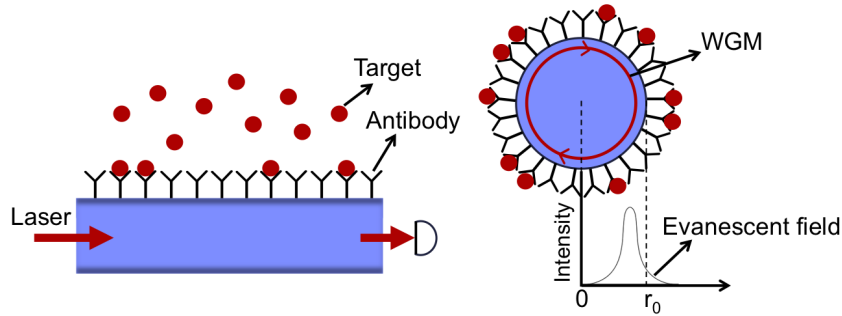


FIGURE 1.3: An optical biosensor based on a straight waveguide (left) and one based on a WGM (right).

that has been under intensive investigation in the past decade. Compared to a straight waveguide sensor, a WGMs microresonator can deliver sensing performance much better while using orders of magnitude less surface area and sample volume. Figure 1.3 shows an optical biosensor based on a straight waveguide and a WGM microresonator. Biorecognition molecules, such as antibodies, are frozen onto the surface of the waveguide. They interact with the evanescent field of the laser extending into the medium surrounding the waveguide. When targets are captured, the refractive index near the waveguide surface changes and causes modifications in the optical signal of the output detector. Since the light passes through the waveguide once, and the sensing signal is gathered outside of the waveguide, a long waveguide is needed to detect small quantities of biomolecules [53].

On the other side, the light in the WGMs resonators interacts repeatedly with the biomolecules on the surface of the microresonator through the evanescent field. The effective interaction length of a WGMs resonator is related to the quality factor, not the physical length of the sensor and it is defined by [54]

$$L_{\text{eff}} = \frac{Q\lambda}{2\pi n} \quad (1.1)$$

where n is the refractive index of the resonator and λ is wavelength. As a WGM resonator, the SNAP capillary resonator performs sensing by detecting the refractive index changes inside of the capillary. The change of refractive index can be produced by the binding of the biomolecules

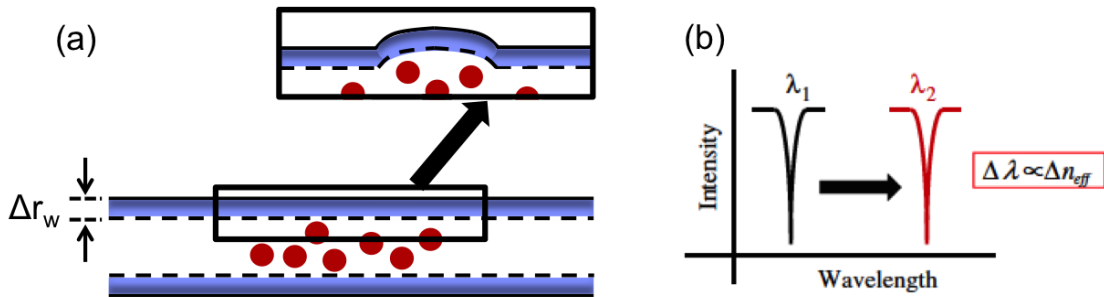


FIGURE 1.4: **a.** A SNAP Sensor. **b.** WGM shifts from λ_1 to λ_2 in response to binding of the target biomolecules to SNAP capillary microresonator interior surface [57].

to the sensor surface (see Figure 1.4(a)) or the change of bulk solution inside the capillary [55]. The WGM spectral position is related to the refractive index through the resonant condition [56]

$$m\lambda = 2\pi r n_{eff} \quad (1.2)$$

where m is an integer that describes the azimuthal quantum number, λ is the resonant wavelength, r is the capillary radius, and n_{eff} is the effective refractive index experienced by the WGMs. Equation 1.2 shows that resonance wavelength happens when an integer multiple of that wavelength matches the circumference. When the target biomolecules are captured to the interior surface of SNAP capillary, the refractive index near the SNAP surface is modified, thus n_{eff} changes, which leads to the shift in the WGM spectral position, as shown in Figure 1.4(b) [57].

$$\frac{\Delta \lambda}{\lambda} \approx \frac{\Delta n}{n} \quad (1.3)$$

Therefore, by directly or indirectly monitoring the spectral shift of WGM, it is possible to obtain information about the binding of biomolecules interaction on the interior surface of the SNAP resonator [58]. To investigate the sensitivity of a capillary sensor, some other parameters are required such as wall thickness of the capillary [53], operating wavelength [26], resonator size [59], and so.

Microfluidic

Microfluidic sensing with optical WGMs circulating along the uniform capillary has been proposed and demonstrated in Ref. [26] and developed in numerous publications [15, 18]. White, Oveys, and Fan [26] proposed and demonstrated a fused silica capillary with a few micron thick wall acting as a WGM resonator sensor of the refractive index of liquid carried by the capillary. In their first demonstration and follow up publications [8, 15], an axially uniform silica capillary coupled to a transverse microfiber or planar waveguide was explored. Sensing of fluid inside the capillary was performed locally at the position of the transverse waveguide and was based on the measurement of variation of a single resonance. Employing a SNAP resonator at the capillary surface allows to significantly advance this method. In particular, it enables the detection of changes, which happen away from the waveguide position along the length of the resonator by controlling the variation of resonant spectra of this resonator [38]. In fact, this approach suggested potentially enables the reconstruction of the spatial distribution of refractive index of fluid flowing inside the capillary from the resonator spectrum and simultaneous sensing and manipulation of fluid components.

1.1 Dissertation Organization

The present research work is directed towards the introduction of SNAP microresonators for optofluidics. The thesis comprises 6 chapters. Chapter 1 (the present chapter) provides a general introduction, and the thesis outline.

The following chapter will present a brief review of the theoretical background of SNAP device and SNAP theory, including an analogy to quantum mechanics concerning the behavior of the light in a SNAP, common methods of SNAP fabrication, and SNAP spectrograms. The following three chapters are dedicated to specific SNAP topics.

In chapter 3, we introduce a new low-cost method to fabricate SNAP optical microresonators in an optical fiber by pulling it using the flame brush technique. We characterize the resulting resonators and find that they can host tens of axial modes with very high quality factors.

We will present in chapter 4 a demonstration of SNAP microresonators fabrication at the surface of an optical capillary fiber, and how to reduce the wall thickness to achieve sensitivity to the capillary inside.

In chapter 5, we combine the ideas of SNAP devices at a surface of a capillary fiber and WGM microfluidic sensing platforms, showing that control over the WGMs propagating along the microcapillary can be performed only by nonuniformities of the liquid.

Finally, the last chapter will cover the main conclusion, summarize this work, as well as the suggestions for future research.

Chapter 2

Surface Nanoscale Axial Photonics (SNAP)

In this chapter, a theoretical description of surface nanoscale axial photonics is presented before introducing our experimental works and results in the following chapters. First, a brief overview of some concepts of resonators is given. We then introduce the theory of light in a cylindrical step-profile structure, including an analogy to Quantum Mechanics, as well as the description of the light in SNAP resonators, and common fabrication methods. Finally we briefly talk about SNAP spectrograms.

2.1 Background

In this section, we describe some commonly used aspects of an optical microresonators, including whispering gallery modes (WGMs), quality (Q-)factor, free spectral range (FSR), and Maxwell equations. These features will help us to describe our resonator.

2.1.1 Optical Whispering Gallery Modes

A whispering gallery mode (WGM) is a type of wave that can travel inside a convex surface. They were first discovered as acoustic waves in the dome of St. Paul's Cathedral in London, and

then mathematically described by Lord Rayleigh more than 100 years ago [60]. When the light enters a convex surface with a refractive index higher than that of the surrounding medium, it is trapped inside the cavity and guided around by optical total internal reflection at the interface between the cavity and its surrounding area (see Figure 2.1). These microresonators can have different shapes and geometries like toroid, sphere, ring or disk (see Figure 2.2).

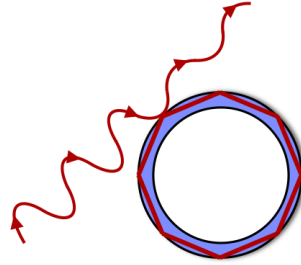


FIGURE 2.1: Whispering Gallery Mode (WGM) propagation inside a cavity.

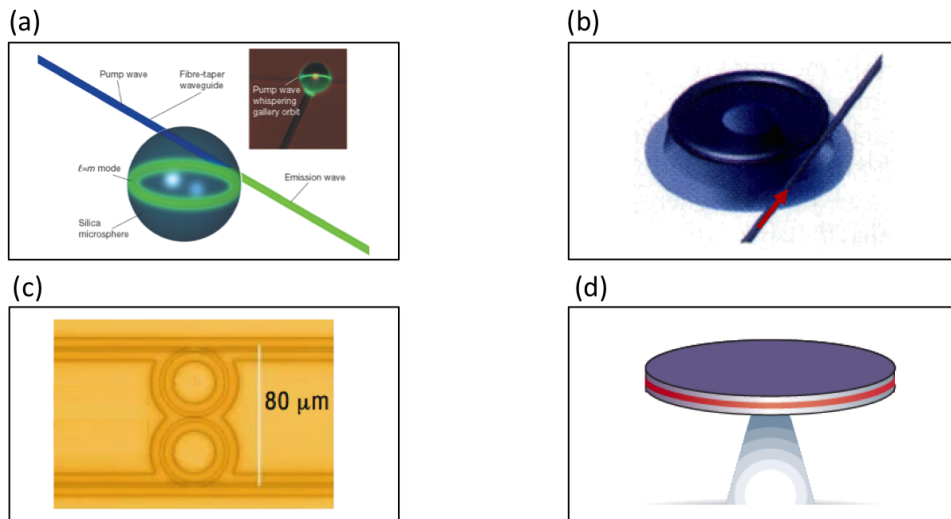


FIGURE 2.2: Different types of WGM resonators, **a.** Silica microsphere whispering gallery resonators [11]. **b.** Microtoroid resonators [11]. **c.** Microring resonators [11]. **d.** Microdisk resonators [11].

In silica glass fibers, due to their smooth surface, very low absorption loss (less than 7 dB/km [61]), and small material attenuation (10^{-3} pm [29]) WGMs can stay confined for long times. Only certain wavelengths will interfere constructively and build up a modal field. These wavelengths are known as resonances and are mathematically described by Equation 1.2.

2.1.2 Free spectral range

The azimuthal free spectral range of a resonator is defined as the frequency or wavelength spacing between two adjacent modes, for example λ_{m+1} and λ_m .

$$FSR_{(\lambda)} = 2\pi r n_{eff} \left(\frac{1}{m} - \frac{1}{m+1} \right) \approx \frac{\lambda^2}{2\pi r n_{eff}} \approx \frac{\lambda^2}{\text{Optical path length}} \quad (2.1)$$

or it can be written as $FSR_{(\nu)} = c/2\pi r n_{eff}$. We can see that when the radius of microcavity decreases, the FSR increases.

2.1.3 Quality factor

Generally, the quality factor (also known as Q-factor) is a dimensionless parameter related to the loss of energy in an oscillatory system. This parameter shows the efficiency of light confinement inside a resonator. It is defined as the resonance wavelength over the full width half maximum (FWHM) of the mode (see Figure 2.3). A high quality factor means that the rate of energy loss is lower and that the magnitude of the field inside is stronger [62].

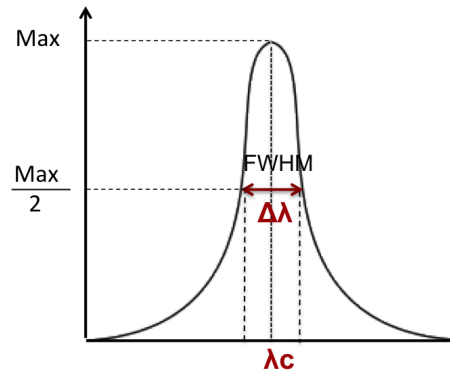


FIGURE 2.3: Definition of quality factor of mode.

$$Q = \frac{\text{Resonance wavelength } (\lambda_c)}{\text{Full width half maximum of mode } (\Delta\lambda)} \quad (2.2)$$

In an optical resonant structure, the Q-factor is proportional to the decay time of the mode ($Q = \omega\tau$), which in turn is inversely related to the losses rate, extrinsic and intrinsic [63]. The extrinsic loss is due to coupling of light out, and can be expressed as

$$Q_{ext} = \frac{2\pi N}{K} \quad (2.3)$$

where N is the mode number and K is the coupling coefficient. When the microcavity is coupled to a single mode waveguide, increasing the coupling will reduce the quality factor [64]. As a result the total quality factor is made up of these two components as $Q^{-1} = \Sigma Q_{int,i}^{-1} + Q_{coup}^{-1}$. The intrinsic quality factor is determined by [65]

$$\frac{1}{Q} = \frac{1}{Q_{rad}} + \frac{1}{Q_{s.s.}} + \frac{1}{Q_{cont}} + \frac{1}{Q_{mat}} \quad (2.4)$$

where Q_{rad} is the radiation loss, $Q_{s.s.}$ the surface scattering loss, Q_{cont} the contaminant loss, and Q_{mat} the material loss.

The radiation loss (Q_{rad}) is due to the fact that the field bends inside the curved cavity. Thus this loss can be reduced with increasing the size of the microcavity. The surface scattering loss ($Q_{s.s.}$) depends on the quality of the process of fabrication. The fabrication of SNAP microresonator is based on the mechanism of surface tension of silica optical fiber, which makes smooth surfaces and leads to reduce this loss. The contaminant loss (Q_{cont}) is introduced by the surface contaminants or adsorption of impurities. This loss can be reduced by fabricating the microcavities in a very clean surroundings. The material absorption loss (Q_{mat}) is the dominant loss for a large microcavity with smooth and clean surfaces. This loss is significantly dependent on the wavelength and refractive index of the microcavity and can be estimated as [66]

$$Q_{mat} = \frac{2\pi n}{\alpha\lambda} \quad (2.5)$$

where n is the refractive index, α is the attenuation coefficient, and λ is the resonant wavelength. In order to reduce the loss and consequently increase the quality factor, choosing a suitable wavelength becomes more important. For example 1550 nm is the most commonly

used wavelength in optical communication systems due to the very low absorption loss of silica fiber ($4.6 \times 10^{-6} \text{ cm}^{-1}$), around 1500 nm [67]. However for aqueous systems, when a microcavity is in contact with water, 1550 nm is not an appropriate wavelength, since water has the high attenuation coefficient of 10.8 cm^{-1} at this wavelength, at room temperature [68]. The minimum attenuation coefficient of water (around $2 \times 10^{-4} \text{ cm}^{-1}$) is reported near 475 nm [69].

A typical resonance spectrum of a SNAP microresonator with diameter of $22 \mu\text{m}$ is shown in Figure 2.4. The free spectral range of the SNAP should be around 12.1 nm , while the quality factor is around 10^6 .

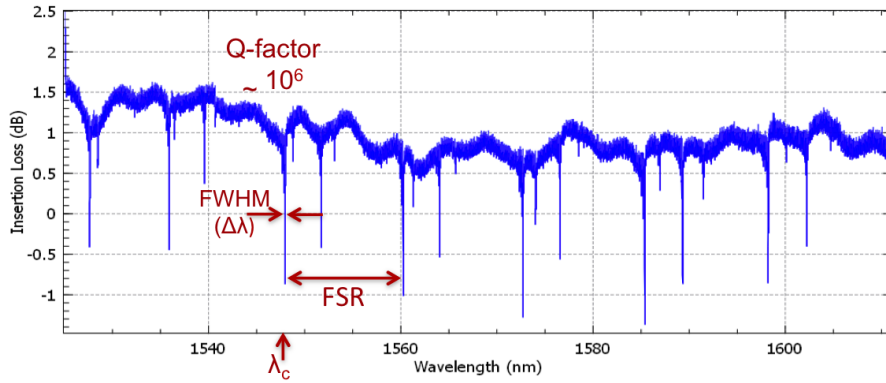


FIGURE 2.4: Typical transmission spectrum of a $22 \mu\text{m}$ SNAP microresonator.

2.1.4 Maxwell's equations

For a theoretical description of how an electromagnetic wave propagates through an optical fiber, we have to look at Maxwell's equations. By assuming harmonic time dependence in Maxwell's equations, the Helmholtz equation for waves can be obtained. Modes are defined as the possible solutions of the Helmholtz equation. In a homogeneous and isotropic dielectric medium Maxwell's equations are defined as

$$\nabla \times \vec{E} = -\mu \frac{\partial \vec{H}}{\partial t}, \quad \nabla \times \vec{H} = \epsilon \frac{\partial \vec{E}}{\partial t} \quad (2.6)$$

$$\nabla \cdot \vec{E} = 0, \quad \nabla \cdot \vec{H} = 0 \quad (2.7)$$

where μ is the magnetic permeability ($\mu = \mu_r \mu_0$) and ϵ is the electric permittivity of the material ($\epsilon = \epsilon_r \epsilon_0$). Taking the curl of equation 2.6 and assuming a harmonic time dependence for the field, the Helmholtz equation can be derived (details can be found in [70])

$$(\nabla^2 + k^2)\Psi = 0 \quad \Psi = \vec{E}, \vec{H} \quad (2.8)$$

Where $k^2 = \omega^2 \mu \epsilon$. Considering that $\omega = \frac{kc}{n}$, we can write

$$\mu \epsilon = \frac{n^2}{c^2} \quad (2.9)$$

where n is the refractive index of the material.

2.2 Surface Nanoscale Axial Photonics (SNAP)

Surface Nanoscale Axial Photonics (SNAPs) devices, a new generation of silica-based WGMs resonators with low losses and high quality factors, consist of a regular capillary optical fiber with smooth variation of its radius and equivalent variation of its refractive index [71]. In Figure 2.5 SNAP shows as extreme bubbles but this variation of radius is of the order of a few nanometers. The dependence of external and internal radii of the capillary, $r_{int}(z) = r_{int}^{(0)} + \Delta r_{int}(z)$ and $r_{ext}(z) = r_{ext}^{(0)} + \Delta r_{ext}(z)$, are assumed to be adiabatically slow and the refractive index is defined as

$$n(\rho, z) = \begin{cases} n_{int}, & 0 < \rho \leq r_{int}(z), \\ n_{cap}, & r_{int}(z) < \rho \leq r_{ext}(z), \\ n_{ext}, & r_{ext}(z) < \rho. \end{cases} \quad (2.10)$$

and the effective radius variation can be given as

$$\Delta r_{eff}(z) = r_0 \Delta n_f(z) + n_{f0} \Delta r(z) \quad (2.11)$$

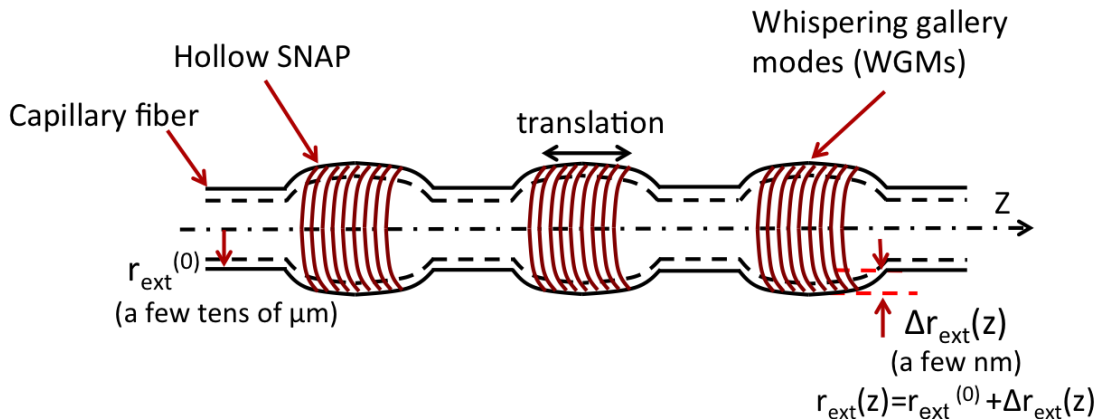


FIGURE 2.5: Schematic of a hollow Surface Nanoscale Axial Photonics (SNAP) device.

In standard optical fibers, light with a wavelength of λ is guided along the fiber's core. The propagation constant of the light is defined as $\beta_0(\lambda) = \frac{2\pi n_{f0}}{\lambda}$ and the speed of light is $v_0 = \frac{c}{n_{f0}}$. The SNAP platform is based on whispering gallery mode which allows the light slowly propagate along the capillary z -axis and circulate around its surface. So, due to this direction of light propagation in SNAP, the axial propagation is naturally slow ($\beta \ll \beta_0(\lambda)$) and the axial speed of the modes is slower than the speed of the light in regular fibers (i.e. $v \ll v_0$) [72]. In addition, the propagation of the light is restricted to the region of the capillary fiber containing the radius variation and light can not escape.

SNAP devices are particularly interesting because of the ultra-low losses, which lead to ultra-high quality factor. They are made of silica, which has low absorption and smooth inner and outer walls surfaces that reduces the scattering of light.

2.3 Step-Profile Fiber

The step-profile fiber is shown in Figure 2.6. This profile is an optical fiber waveguide with a circularly homogeneous cross-section, consists of an unbounded core with uniform refractive index n_{co} , surrounded by an unbounded cladding with uniform refractive index of n_{clad} and the core radius of r [80–82]. The mathematical model of a step-profile fiber is shown in Figure 2.7. The refractive index profile is expressed as

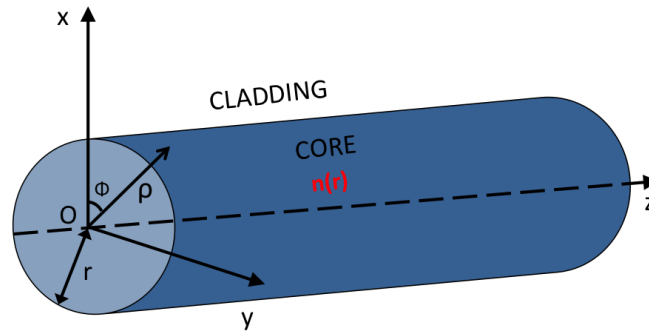


FIGURE 2.6: Section of a step-profile fiber. $n(\rho)$ is the refractive index profile and ρ is radius of the core.

$$n(\rho) = n_{co}, \quad 0 \leq \rho < r; \quad n(\rho) = n_{clad}, \quad r < \rho < \infty \quad (2.12)$$

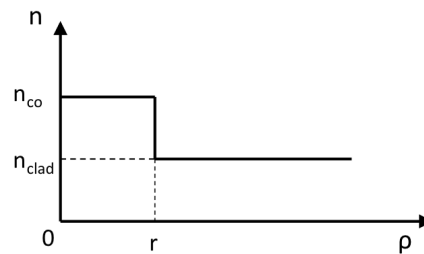


FIGURE 2.7: Index profile of a step-index fiber.

The fiber axis corresponds to the z -axis. We continue this section with a solution of Helmholtz equation for this waveguide. For a general waveguide with no free charge sources, the Helmholtz equation $(\nabla^2 + k^2)\Psi = 0$, $\Psi = \vec{E}, \vec{H}$) represents an eigenvalue problem for k with eigenfunctions $\vec{E}(\vec{r}, \vec{k})$. Here, the eigenfunctions are called modes of the field. A time-dependent solution of this equation for harmonic fields in free space is a plane wave

$$\vec{E}(\vec{r}, t) = \vec{E}_0 \exp(i(\vec{k} \cdot \vec{r} - \omega t)) \quad (2.13)$$

In the cylindrical coordinates (ρ, ϕ, z) , the fields can be represented with z as the **longitudinal** propagation direction and (ρ, ϕ) as the **transverse** coordinates

$$\mathbf{E}(\rho, \phi, z) = \mathbf{e}(\rho, \phi)\exp(ik_z z); \quad \mathbf{H}(\rho, \phi, z) = \mathbf{h}(\rho, \phi)\exp(ik_z z) \quad (2.14)$$

where k_z is the propagation constant in z -axis. In cylindrical coordinates, the gradient operator is given by $\nabla = (\hat{\rho}\partial_\rho + \hat{\phi}^1\partial_\phi + \hat{z}\partial_z)$. When considering the field propagating along the z -axis of an optical fiber, the cylindrical symmetry of the fiber allows us to express the Helmholtz equation as

$$\left(\frac{\partial^2}{\partial\rho^2} + \frac{1}{\rho}\frac{\partial}{\partial\rho} + \frac{1}{\rho^2}\frac{\partial^2}{\partial\phi^2} + \frac{\partial^2}{\partial z^2}\right)\Psi + k^2\Psi = 0 \quad (2.15)$$

where Ψ denotes e_z or h_z and where \vec{k} is the propagation vector and $|k| = 2\pi/\lambda$. There is an approximation we can make to simplify solving this equation. We can assume that propagation in our system is based on WGMs; the field along the z -axis has a very slow variation, thus $\partial_z^2 = 0$. So in cylindrical coordinates, the Helmholtz equations become

$$\left(\frac{\partial^2}{\partial\rho^2} + \frac{1}{\rho}\frac{\partial}{\partial\rho} + \frac{1}{\rho^2}\frac{\partial^2}{\partial\phi^2} + k_T^2\right)\mathbf{e}_z(\rho, \phi) = 0 \quad (2.16)$$

and

$$\left(\frac{\partial^2}{\partial\rho^2} + \frac{1}{\rho}\frac{\partial}{\partial\rho} + \frac{1}{\rho^2}\frac{\partial^2}{\partial\phi^2} + k_T^2\right)\mathbf{h}_z(\rho, \phi) = 0 \quad (2.17)$$

as a 2D eigenvalue differential equation, and where the transverse wave number k_T is

$$k_T^2 = k^2 - k_z^2 = \omega^2\mu\epsilon(\rho_T) - k_z^2 \quad (2.18)$$

Using coordinate separation into with radial and azimuthal separation as $\mathbf{e}_z(\rho, \phi) \propto R(\rho)\Phi(\phi)$ and $\mathbf{h}_z(\rho, \phi) \propto R(\rho)\Phi(\phi)$, leads to second order differential equations

$$\left(\frac{\partial^2}{\partial\phi^2} + m^2\right)\Phi(\phi) = 0 \quad (2.19)$$

$$\left(\frac{\partial^2}{\partial \rho^2} + \frac{1}{\rho} \frac{\partial}{\partial \rho} + k_T^2 - \frac{m^2}{\rho^2}\right)R(\rho) = 0 \quad (2.20)$$

where m is constant.

The harmonic azimuthal independent solutions for Equation 2.19 are

$$\Phi(\phi) = \sin(m\phi) \quad \Phi(\phi) = \cos(m\phi) \quad (2.21)$$

where m is an integer number, equal to or greater than zero and indicates the number of nodes of the field.

The radial Equation 2.20 can be simplify to the form of Bessel's differential equation. The general linear solution of this Equation inside a cylindrical waveguide (e.g. the core of an optical fiber) for any m , where $2m$ indicates the nodes number of the field, is defined by the Bessel function of the first kind [83]

$$R_{\rho < r}^m(\rho) = A_m J_m(k_T \rho) \quad (2.22)$$

Outside of the core, the boundary condition for an infinite cladding assuming $k_z < n_{clad}k$ require us to use combinations of the Bessel functions, known as the first and second kind of Hankel functions

$$R_{\rho > r}^m(\rho) = B_m H_m^{(1)}(k_T \rho) + C_m H_m^{(2)}(k_T \rho) \quad (2.23)$$

where

$$H_m^{(1)}(k\rho) = J_m(k\rho) + iY_m(k\rho), \quad H_m^{(2)}(k\rho) = J_m(k\rho) - iY_m(k\rho) \quad (2.24)$$

Definition of the boundary conditions leads to the eigenvalue equation. Each eigenvalues corresponds to a precise radial mode number of p . Thus each mode is defined by two mode numbers

of p and m , the radial mode number, and azimuthal mode number. The eigenvalue equation for HE_{pm} and EH_{pm} and whispering gallery modes with a propagation constant of β and a wave number of $k = 2\pi/\lambda$ with radius of ρ_0 is given by

$$\left(F_{1m}(U) + F_{2m}(W) \right) \left[F_{1m}(U) + \frac{n_{\text{clad}}^2}{n_{\text{co}}^2} F_{2m}(W) \right] = \left[\frac{m\beta}{kn_{\text{co}}} \right]^2 \left[\frac{V}{UW} \right]^4 \quad (2.25)$$

where

$$F_{1m}(x) = \frac{1}{xJ_m(x)} \frac{dJ_m(x)}{dx}, \quad F_{2m}(x) = \frac{1}{xH_m^{(2)}(x)} \frac{dH_m^{(2)}(x)}{dx} \quad (2.26)$$

where U and W are defined by

$$U = r(k^2 n_{\text{co}}^2 - \beta^2)^{1/2}; \quad W = r(k^2 n_{\text{clad}}^2 \beta^2)^{1/2} \quad (2.27)$$

and V is defined as $V = kr(n_{\text{clad}}^2 - n_{\text{co}}^2)^{1/2}$. In the zero propagation constant, Equation 2.25 can split into two equations. The TE modes is given by:

$$F_{1m}(U_0) + F_{2m}(W_0) = 0 \quad (2.28)$$

and for TM modes we have:

$$F_{1m}(U_0) + \frac{n_{\text{clad}}^2}{n_{\text{co}}^2} F_{2m}(W_0) = 0 \quad (2.29)$$

where $U_0 = n_{\text{co}}kr$, and $W_0 = n_{\text{clad}}kr$.

2.4 Quantum Analogy

In this section, we discuss formal analogies between the guided wave optics and quantum mechanics. We will subsequently explain the theory of SNAP by presenting a solution of Helmholtz's equation for a capillary fiber.

2.4.1 Analogy of guided optical modes and quantum mechanics

We present an analogy between the Helmholtz equation and Schrödinger's equation. To simplify the discussion, we consider the one-dimensional form of both equations. The similarity between physical equations allows us to understand better the behavior of the light at the surface of a SNAP device.

2.4.1.1 Guided optical waves - Helmholtz equation

The general solution for waveguide modes or electric field along z -direction is

$$E_z(x, z) = E_z(x)e^{i\beta z} \quad (2.30)$$

$E_z(x)$ is a transverse eigenfunction of a guided mode profile that propagates along the z -axis of a dielectric step-index waveguide with a core dimension of $(2d)$. For distances between (d) and $(-d)$, the refractive index is equal to n_1 (the core refractive index) and for distances greater than (d) or less than $(-d)$, the refractive index is equal to n_2 , the cladding refractive index. In this configuration, we can write the Helmholtz equation as

$$\begin{aligned} \left[\frac{d^2}{dx^2} + k_T^2 \right] E_z &= \left[\frac{d^2}{dx^2} + (k^2 - k_z^2) \right] E_z = \left[\frac{d^2}{dx^2} + \omega^2 \mu \epsilon(x) - k_z^2 \right] E_z \\ &= \left[\frac{d^2}{dx^2} + k_0^2 n^2(x) - k_z^2 \right] E_z = 0 \end{aligned} \quad (2.31)$$

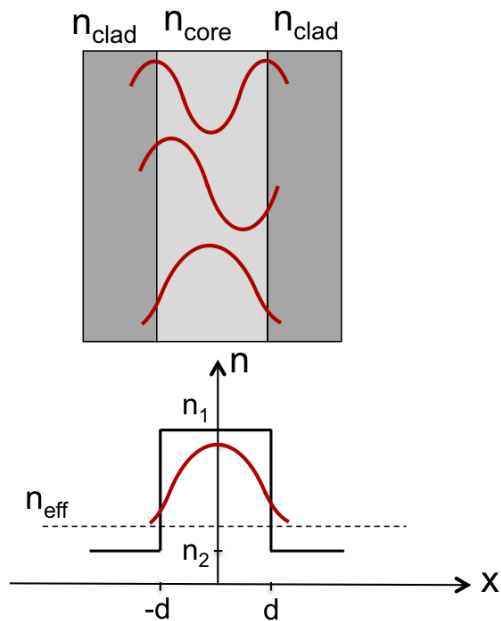


FIGURE 2.8: Solution of the 1D Helmholtz equation for a step-index dielectric waveguide.

The eigenvalue $k_T = k^2 - k_z^2$ is the transverse propagation constant, where k_z is the longitudinal propagation state, also known as β , $|k|^2 = \omega^2 \mu \epsilon(x)$, and $k_0^2 n^2$ is x -sectional index profile.

Figure 2.8 shows the solution to the one-dimensional Helmholtz equation in a step-index dielectric waveguide. The figure is interesting for three reasons. First, it shows only discrete propagation constant (β) values are possible. Second, higher order modes have more nodes ($E_z(x) = 0$). Third, longer waveguides with higher index contrast supports more modes. For guided modes

$$n_{\text{clad}} < n_{\text{eff}} < n_{\text{core}} \quad (2.32)$$

2.4.1.2 Quantum mechanics - Time-independent Schrödinger equation

On the other hand, a time-independent Schrödinger solution for the wavefunction $\Psi(r)$ with an eigenvalue energy of E for a particle of mass m in a potential well is shown in Figure 2.9.

As you can see here, for distances less than $(-d)$ and greater than d , the potential is V_2 , and for distances equal to or less than d and $(-d)$, it equals V_1 . The corresponding time-independent Schrödinger equation in one-dimension is written as:

$$\left[\frac{-\hbar^2}{2m} \frac{d^2}{dx^2} + V(x) - E \right] \Psi = 0 \quad (2.33)$$

with wavefunctions (energy eigenstates)

$$U(x, t) = \Psi(x) e^{-i\frac{E}{\hbar}t} \quad (2.34)$$

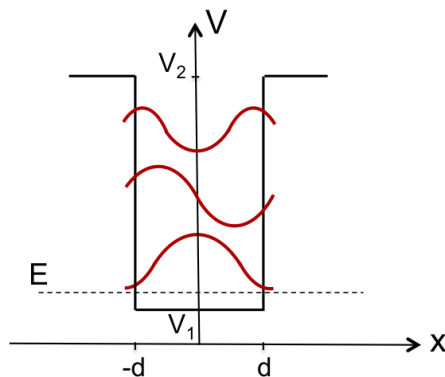


FIGURE 2.9: Time-independent Schrödinger solution in one-dimension.

Where $\Psi(x)$ is time-independent wave function. Now, by comparing Equations 2.33 and 2.31, we can conclude that the potential $V(x)$ in Schrödinger's equation is equivalent to $-n^2(x)$ in the Helmholtz equation, while the energy (eigenvalue) E is equivalent to the propagation constant along the z-axis, k_z^2 . In a 1d potential well, the energies are quantized, meaning that only discrete energy values are allowed. Also, wave functions with higher energy have more nodes ($\psi(x) = 0$), and deeper and wider potential wells gives more bounded states. For bounded states

$$V_2 < E < V_1 \quad (2.35)$$

This analogy is summarized in table 2.1.

TABLE 2.1: The guided optical waves and Quantum mechanics

Guided wave	Quantum mechanics
Helmholtz equation in a waveguide $\left[\nabla + k_0^2 n^2(x) - \beta^2 \right] E_z = 0$	1D time independent Schrödinger equation $\left[\frac{-\hbar^2}{2m} \frac{d^2}{dx^2} + V(x) - E \right] \Psi = 0$
$E_z(x)$: x -sectional optical mode	$\Psi(x)$: time-independent wavefunction
$k_0^2 n^2(x)$: x -sectional index profile	$V(x)$: potential energy
β^2 : propagation constant	E : energy (eigenvalue)
Electric field along z -direction $E_z(x, z) = E_z(x) e^{i\beta z}$	Time-dependent wavefunction $U(x, t) = \Psi(x) e^{-i\frac{E}{\hbar}t}$
Discretized propagation constant - β values	Discretized energy levels - states
Transverse standing wave for confined photon	Transverse standing wave for bound particle
Longer with higher index contrast waveguide, contains more modes	Broader and deeper potential well contains more bounded states
Higher order modes supports more nodes ($E = 0$)	Wavefunction with higher energy supports more nodes ($\Psi = 0$)
Guided modes: $n_{clad} < n_{eff} < n_{core}$	Bond states: $V_1 < E < V_2$

2.4.2 SNAP theory

Let's go back to Equation 2.15. We consider that $\Psi \propto \exp(im\varphi) \exp(i\beta z)$ along the azimuthal direction, thus $\partial_z^2 = -\beta^2$ and $\frac{1}{\rho^2} \partial_\varphi^2 = -\frac{m^2}{\rho^2}$, where m is the discrete azimuthal quantum number and β is the propagation constant. These assumptions allow us to rewrite the equation in the form of Bessel's differential equation

$$\partial_\rho^2 \Psi + \frac{1}{\rho} \partial_\rho \Psi + \left(k^2 - \frac{m^2}{\rho^2} - \beta^2 \right) \Psi = 0 \quad (2.36)$$

which is the general equation of the Helmholtz equation in cylindrical coordinate. Following this brief background, we can now explain SNAP theory. There are several approximations that we can apply to a SNAP device possessing a nanoscale variation in radius. We first assume that the field is propagating inside the wall of a SNAP capillary fiber along the z -axis. Our second assumption is to suppose that there are no input or output waveguides in a capillary fiber, so that the propagating field is based on the whispering gallery modes inside the wall of

a SNAP capillary fiber. The WGMs considered are labeled by the azimuthal quantum number m , radial quantum number p , and the axial quantum number q . In SNAP microresonator, the axial component is not variable, but its amplitude of them are very sensitive to bridge of the the fiber. Finally, we consider the propagation of light to be adiabatic. This signifies that the effective radius variation of a SNAP varies slowly without perturbing the mode shape so that the scale of the propagating light does not change. In cylindrical coordinates (z, ρ, φ) , the field distribution is defined as [71]

$$E_{mpq}(z, \rho, \varphi) = \exp(\pm im\varphi)Q_{mp}(\rho)\Psi_{mpq}(z) \quad (2.37)$$

where $\Psi_{mpq}(z)$ is the distribution of the WGMs along the z -axis. If we apply this equation to the Helmholtz equation, we can write

$$(\nabla^2 + k^2)\exp(\pm im\varphi)Q_{mp}(\rho)\Psi_{mpq}(z) = 0 \quad (2.38)$$

To simplify this equation for cylindrical waveguides, we can use a transversal (x, y) and longitudinal (z) field decomposition. As shown in Equation 2.18 the propagation constant (k) is written as $k^2 = k_T^2 + k_z^2$, where k_T and k_z are the transverse and longitudinal propagation constants, respectively. For a lossless propagating wave inside the wall of a capillary fiber, we can consider $k_z = \beta$. The slowness of WGMs is manifested in the small value of their $\beta(z)$, or, equivalently in the proximity of their wavelength λ to the cutoff wavelength. The fact that the cutoff wavelengths of the WGMs with very large azimuthal quantum numbers m correspond to the zero propagation constant, $\beta = 0$, does not contradict to the well-known relation $k_{mp}n_{ext} < \beta < k_{mp}n_{cap}$ for small m [84]. As a result, we can write

$$k^2 = k_T^2 + \beta^2 \quad (2.39)$$

Therefore, Equation 2.38 will be

$$\nabla^2(\Psi_{mpq}(z)Q_{mp}(\rho)\exp(\pm im\varphi)) + (k_T^2 + \beta^2)\Psi_{mpq}(z)Q_{mp}(\rho)\exp(\pm im\varphi) = 0 \quad (2.40)$$

Then

$$\begin{aligned} & \Psi_{mpq}(z) \nabla_{\perp}^2 (Q_{mp}(\rho) \exp(\pm im\varphi)) + (Q_{mp}(\rho) \exp(\pm im\varphi)) \frac{d^2 \Psi}{dz^2} \\ & + K_T^2 (\Psi_{mpq}(z) Q_{mp}(\rho) \exp(\pm im\varphi)) + \beta^2 (\Psi_{mpq}(z) Q_{mp}(\rho) \exp(\pm im\varphi)) = 0 \end{aligned} \quad (2.41)$$

We can split Equation 2.41 and rewrite it as

$$\begin{aligned} & \frac{1}{Q_{mp}(\rho) \exp(\pm im\varphi)} \left[\nabla_{\perp}^2 (Q_{mp}(\rho) \exp(\pm im\varphi)) + K_T^2 \right] \Psi_{mpq}(z) \\ & + \frac{1}{Q_{mp}(\rho) \exp(\pm im\varphi)} \left[\frac{d^2}{dz^2} + \beta^2 \right] \Psi_{mpq}(z) = 0 \end{aligned} \quad (2.42)$$

By solving the equation above, we will find the one-dimensional Schrödinger equation to be

$$\frac{d^2 \Psi_{mpq}}{dz^2} + \beta^2(\lambda, z) \Psi_{mpq} = 0, \quad \beta^2(\lambda, z) = E(\lambda) - V(z) \quad (2.43)$$

where the effective energy, which is proportional to deviation of the wavelength from the cut-off wavelength, is calculated as

$$E(\lambda) = -k^2 \frac{\Delta\lambda}{\lambda_0} \quad (2.44)$$

and the effective potential of the wave is proportional to the variation of radius and refractive index or the variation of the effective radius, thus

$$V(z) = -2k^2 \left[\frac{\Delta r(z)}{r_0} + \frac{\Delta n(z)}{n_0} \right] = -2k^2 \left[\frac{\Delta r_{eff}(z)}{n_0 r_0} \right] \quad (2.45)$$

where $k = \frac{2\pi n_0}{\lambda_0}$.

The expression for the propagation constant of a slow WGM can be derived using the first order perturbation theory [85]. The solution of Helmholtz equation in the axially symmetric optical capillary fiber in the cylindrical coordinates (ρ, z, φ) as Equation 2.37 where function $Q_{mp}(\rho, \lambda)$ satisfies the differential equation [84]

$$\frac{d^2 Q_{mp}(\rho, \lambda)}{d\rho^2} + \frac{1}{\rho} \frac{dQ_{mp}(\rho, \lambda)}{d\rho} + \left(\left(\frac{2\pi n(\rho)}{\lambda(z)} \right)^2 - \frac{m^2}{\rho^2} - \beta_{mp}^2(\lambda) \right) Q_{mp}(\rho, \lambda) = 0 \quad (2.46)$$

where $n(\rho)$ is the radial distribution of the refractive index. For WGMs having $m \gg 1$, the cutoff frequencies λ_{mp} correspond to the vanishing propagation constant.

$$\beta_{mp}(\lambda_{mp}) = 0 \quad (2.47)$$

We rewrite Equation 2.46 as

$$\mathbf{L}Q_{mp}(\rho, \lambda) = \beta_{mp}^2(\lambda)Q_{mp}(\rho, \lambda)$$

$$\mathbf{L} = \frac{d^2}{d\rho^2} + \frac{1}{\rho} \frac{d}{d\rho} + \left(\frac{2\pi n(\rho)}{\lambda} \right)^2 - \frac{m^2}{\rho^2} \quad (2.48)$$

It is seen from Equation 2.48 that $\beta_{mp}^2(\lambda)$ is the eigenvalue of the operator \mathbf{L} . Consequently, from Equation 2.47, functions $Q_{mp}(\rho, \lambda_{mp})$ are the eigenfunctions of the operator

$$\mathbf{L}_{mp}^{(0)} = \frac{d^2}{d\rho^2} + \frac{1}{\rho} \frac{d}{d\rho} + \left(\frac{2\pi n(\rho)}{\lambda_{mp}} \right)^2 - \frac{m^2}{\rho^2} \quad (2.49)$$

and have zero eigenvalues. Here we are interested in the situation when the variation of the cutoff wavelength, $\lambda_{mp}^{(cut)}(z) - \lambda_{mp}^{(0)}$, and the deviation of the radiation wavelength from the cutoff, $\lambda - \lambda_{mp}^{(cut)}(z)$, are small. This condition is satisfied for the small variation of radii, $\Delta r_{int}(z)$ and $\Delta r_{ext}(z)$, and for the evanescent values of $Q_{mp}(\rho, z)$ near the internal wall surface. Under these assumptions, for small $\beta_{mp}(\lambda)$ we have

$$\mathbf{L} = \mathbf{L}_{mp}^{(0)} + \Delta\mathbf{L}_{mp}^{(0)},$$

$$\Delta\mathbf{L}_{mp}^{(0)} = \left(\frac{2\pi n(\rho)}{\lambda}\right)^2 - \left(\frac{2\pi n(\rho)}{\lambda_{mp}}\right)^2 \approx \frac{2(2\pi n(\rho))^2}{\lambda_{mp}^3}(\lambda_{mp} - \lambda) \quad (2.50)$$

Using Equation 2.50, we can find eigenvalues $\beta_{mp}^2(\lambda)$ in the first order of the perturbation theory [86]

$$\begin{aligned} \beta_{mp}^2(\lambda) &= \left\langle Q_{mp}(\rho, \lambda_{mp}) | \Delta\mathbf{L}_{mp}^{(0)} | Q_{mp}(\rho, \lambda_{mp}) \right\rangle \\ &= \frac{8\pi^2}{\lambda_{mp}^3} \left\langle Q_{mp}(\rho, \lambda_{mp}) | \Delta\mathbf{L}_{mp}^{(0)} | Q_{mp}(\rho, \lambda_{mp}) \right\rangle (\lambda_{mp} - \lambda) \end{aligned} \quad (2.51)$$

where functions $Q_{mp}(\rho, \lambda_{mp})$ are normalized, $\left\langle Q_{mp}(\rho, \lambda_{mp}) | Q_{mp}(\rho, \lambda_{mp}) \right\rangle = 1$. Since $Q_{mp}(\rho, \lambda_{mp})$ is localized in the region of the capillary wall where $n(\rho) = n_{cap} = const$, we can ignore the contribution of evanescent parts of $Q_{mp}(\rho, \lambda_{mp})$ in Equation 2.51 which is simplified to

$$\beta_{mp}^2(\lambda) = \frac{8\pi^2}{\lambda_{mp}^3} n_{cap}^2 (\lambda_{mp} - \lambda) \quad (2.52)$$

Finally to simplify solving the Helmholtz equation in an optical capillary fiber, we can assume that propagation in our system is based on WGMs which are localized along the capillary axis. The slowness of WGMs is manifested in the small value of their propagation constant, β , or, equivalently, in the proximity of their wavelength λ to cutoff wavelength $\lambda_{mp}^{(cut)}(z)$. Then equation (Eq. 2.46) is simplified to the following equation independent of wavelength λ

$$\partial_\rho^2 Q_{mp} + \frac{1}{\rho} \partial_\rho Q_{mp} + \left(\left(\frac{2\pi n(\rho, z)}{\lambda_{mp}} \right)^{(cut)(z)} - \frac{m^2}{\rho^2} \right) Q_{mp} = 0 \quad (2.53)$$

The general linear solution of this equation is defined by

$$Q_{m,p}(\rho, z) = \begin{cases} AJ_m(k_{mp}n_{int}\rho), & 0 < \rho \leq r_{int}(z), \\ BJ_m(k_{mp}n_{cap}\rho) + CY_m(k_{mp}n_{cap}\rho), & r_{int}(z) < \rho \leq r_{ext}(z), \\ DH_m(k_{mp}n_{ext}\rho), & r_{ext}(z) < \rho. \end{cases} \quad (2.54)$$

Here $k_{mp} = 2\pi/\lambda_{mp}^{(cut)}$, function $J_m(x)$ and $Y_m(x)$ are Bessel functions, and parameters A, B, C and D are determined from continuity of $Q_{mp}(\rho, z)$ and its derivative over ρ by applying electromagnetic boundary conditions. The solution of Equation 2.54 with the refractive index profile determined by Equation 2.10 allows us to express the cutoff wavelength, $\lambda_{mp}^{(cut)}(z)$, through the external and internal radii, $r_{ext}(z)$ and $r_{int}(z)$.

2.4.2.1 “Quantum theory” of light in SNAP devices

SNAP devices can be divided into three different regimes, which are illustrated in Figure 2.10. The position of energy, (E), indicates the structure of a SNAP device similar to the three basic phenomena of quantum mechanics [86]. Here, it is proportional to the wavelength detuning from the resonator. The point z_1 shows the position of a microfiber along a SNAP fiber.

The first regime exhibits a bottle microresonator [87], which corresponds to a quantum well in quantum mechanics and the potential is proportional to the negative change of the effective radius variation. When the microfiber is located in this regime, it leads to formation of the excited WGMs. The modes are restricted between tuning points of z_{t1} and z_{t2} at different series of wavelength, resulting in the formation of discrete states in this regime. At the point z_1 , the amplitude of resonance transmission is proportional to the amplitude of the WGM [28]. Also, if the microfiber is located at the node of WGM, no coupling occurs and the WGMs will be dark. These points are shown in Figure 2.10 as a dark state. Due to the effective radius variation of the SNAP device, waves which are launched in positive and negative directions along the SNAP device are reflected at the turning points z_{t1} and z_{t2} , resulting in constructive interference [88].

The second regime shows a shallow concave fiber waist, which corresponds to a potential barrier. If the energy is greater than the potential, corresponding to an energy found above the barrier, the WGMs excited in the SNAP device will not be localized. If the energy is less than the

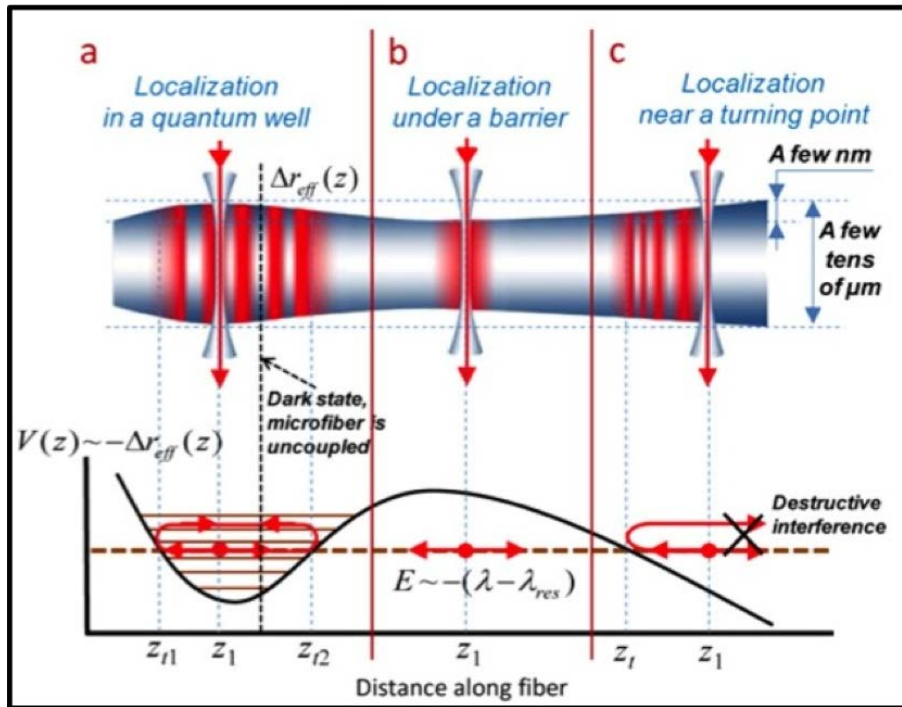


FIGURE 2.10: SNAP devices, **a.** WGM bottle microresonator [28]. **b.** Concave fiber waist [28]. **c.** Monotonic variation of fiber radius [28].

potential, corresponding to an energy found below the barrier, the amplitudes of the excited WGMs will exponentially decay from point z_1 .

If the effective radius variation is equal to zero (implying a uniform fiber), the WGMs are delocalized. As a result, the excited WGMs in a uniform fiber radiate out along the axis of the fiber. However, we rarely see a resonant mode due to the self-interference of these Gaussian beams that occurs when they are rotating close to the surface. Also, the quality factor of this resonant mode is at least 2.5 times smaller than the equivalent modes in a spheroidal microresonator [89].

Finally, in the third regime, the radius of the SNAP device monotonically increases close to the point of z_1 . In this regime, the excited WGMs propagating in the direction of decreasing radius (i.e. the negative direction along the SNAP device) from point z_1 will interfere with the WGMs reflected from the turning point of z_t and, from the other side, the excited WGMs which propagate in the positive direction will undergo destructive interference. Therefore, the propagation of light is launched between the turning point z_t and the point z_1 in this regime [90].

2.5 Coupling light

In general, coupling describes the process of energy transfer from one medium to another. In optics, when two or more optical waveguides, such as optical fibers, are placed in close proximity, coupling is achieved. In this situation, the evanescent field generated by one of the fibers reaches the other fibers before decaying completely [73]. Evanescent field couplers have various geometries such as prism [65, 74], tapered fiber [75, 76], planar waveguide [77, 78] and etc. Coupling to microcavity through a tapered fiber has several advantages such as relatively simple fabrication, and controlling the coupling efficiency by changing the microfiber thickness. Since for microfluidic application, low loss of power and high efficient coupling are important, evanescent coupling through an optical microfiber is used.

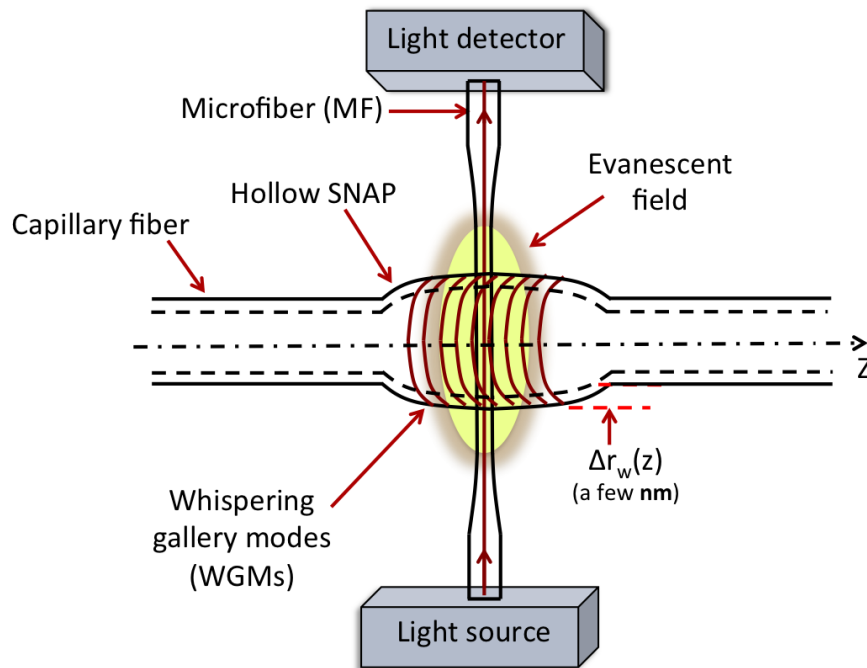


FIGURE 2.11: Coupling of the light from a microfiber (MF) to a hollow SNAP resonator.

As is shown in Figure 2.11, for coupling the light in the SNAP we are using a tapered fiber as a waveguide which generates a strong evanescent field [79]. The tapered fiber has a subwavelength waist and it was fabricated from a conventional single-mode fiber after stripping the polymer coating. The tapering method, which include pulling the fiber with two linear stages, was similar to flame-brushing method developed for the fabrication of biconical tapers softened in flame. We

sent the light from a laser through the tapered fiber, with the light coming out of the waveguide sent to an optical spectrum analyzer for analyzing. When the SNAP is close to the tapered fiber, the fiber's evanescent field produced propagating wave modes in the SNAP microresonator. As a result, the light is coupled from the microfiber to the SNAP microresonator and whispering gallery modes are excited. When we observe the transmission at different wavelengths, we can see the transmission drops when a resonant mode is excited (see Figure 2.12).

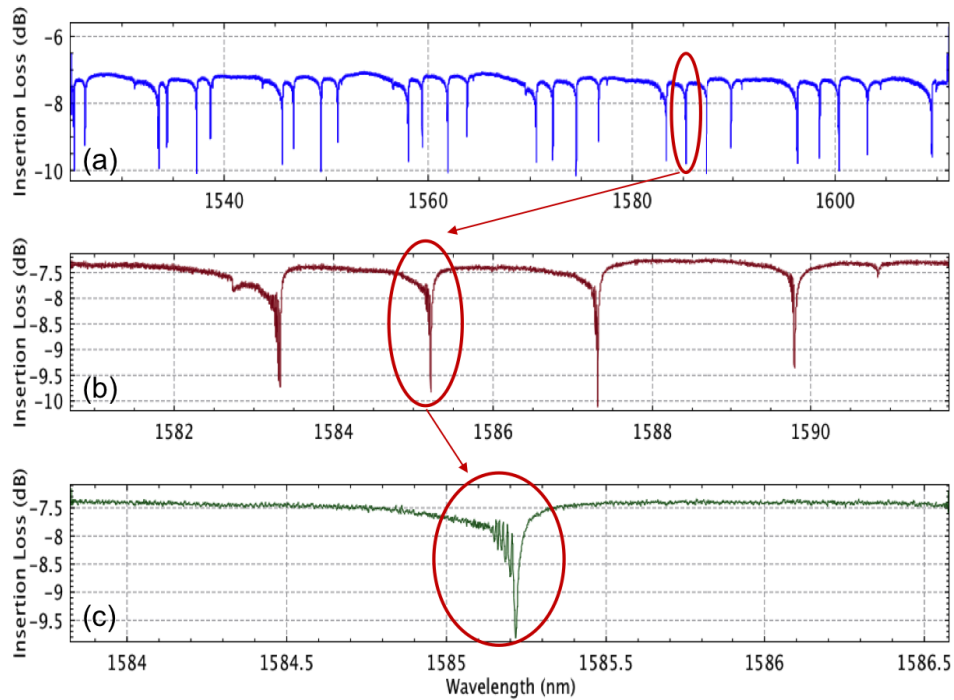


FIGURE 2.12: Spectra of a SNAP resonator, at different range of wavelength. **a.** $\Delta\lambda = 86.13nm$. **b.** $\Delta\lambda = 10.26nm$. **c.** $\Delta\lambda = 2.55nm$.

More details about tapered fibers and their fabrication can be found in [70].

2.6 Current Fabrication Methods of SNAP

Three techniques were originally introduced for the fabrication of SNAP device; IR beam exposure, UV beam exposure [91] and femtosecond laser [34].

IR beam exposure

The first method is based on modification of the density and refractive index of the tapered fiber material by annealing. In this set-up, a fiber is first tapered to a small diameter $10 - 50 \mu m$. A CO_2 laser beam is then focused on the surface of the tapered fiber (see Figure 2.13(a)). Due to absorption of the laser light, heating causes a local annealing of the fiber, resulting in changes in the density and refractive index of the fiber. This method is applicable for a variety of glass fibers [92].

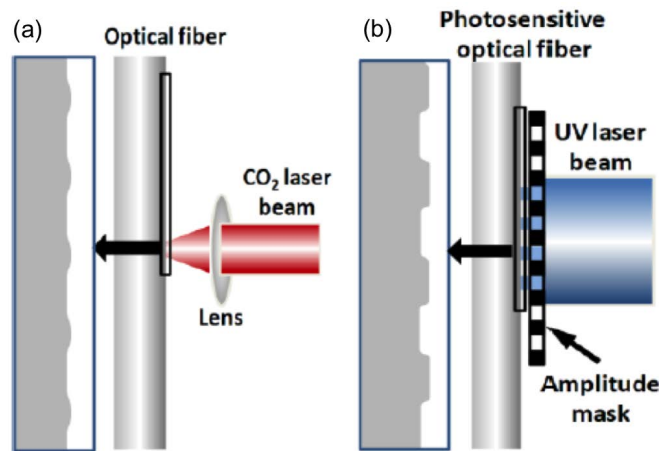


FIGURE 2.13: **a.** First fabrication method of SNAP device with IR (CO_2 laser) beam exposure [30]. **b.** Second fabrication method of SNAP devices with UV beam exposure [30].

UV beam exposure

This method is based on the modification of the refractive index and density of a fiber by UV beam exposure. A photosensitive Germanium (Ge)-doped, coreless tapered fiber is needed. An excimer laser beam with a wavelength of 248 nm is radiated to the fiber through an amplitude mask with the desired pattern of a $300 \mu m$ period (see Figure 2.13(b)). The bottle microresonators created by this method are very shallow, with an axially asymmetric effective radius variation of 0.5 nm .

Due to formation of GeOHC at around 240 nm , this kind of fiber demonstrates substantial absorption at UV wavelengths [93], showing significant attenuation. As a result, the effective radius variation at the front fiber surface is different than the effective radius at the back fiber surface. In spite of this, the UV beam exposure method allows for a very accurate variation of the fiber's effective radius.

Femtosecond laser

This new method is based on the femtosecond laser and does not rely on relaxation of the remaining stress inside of a fiber. In this technique, the powerful electromagnetic field of the ultra-short femtosecond pulse is using a nonlinear optical interaction in the medium. A micrometer volume of the focal point of the laser can confine this optical interaction. Thus, the modified area induced by this technique inside of the fiber can be much smaller than the spot size of light on the surface of the fiber in the previous methods.

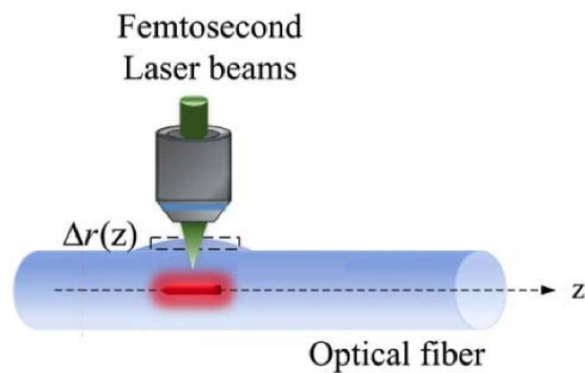


FIGURE 2.14: Third fabrication method of SNAP device with femtosecond laser [34].

In this set-up, a femtosecond laser pulse with $\lambda = 520 \text{ nm}$ and duration of 350 fs is focused on an optical fiber with radius of $40 \text{ }\mu\text{m}$ [94]. Results show that this method can improve the fabrication precision and reduce errors of the effective radius variation. This fabrication is applicable for various type of materials [95].

2.7 SNAP Spectrogram

After fabrication, we characterize our SNAP by using the method of characterization with sub-angstrom precision [96]. Because of the cylindrical geometry of microfibers and SNAP devices, common methods of characterization such as atomic force microscopy (AFM), transmission electron microscopy (TEM), or scanning electron microscopy (SEM) are not applicable.

The experimental set-up is shown schematically in figure 2.15. In this method, a light source and a light detector are connected to the microfiber directly. The microfiber is placed in a

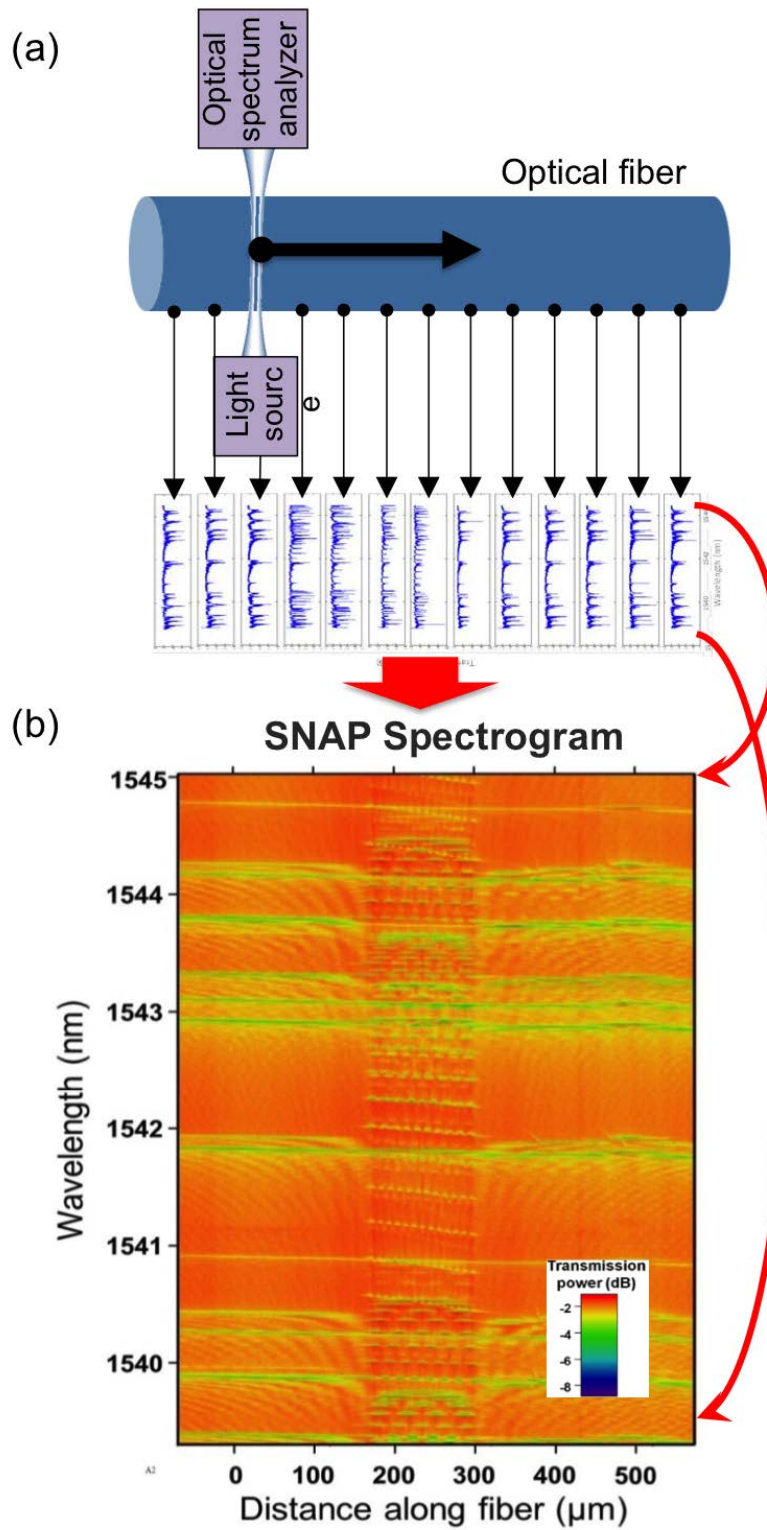


FIGURE 2.16: **a.** An example of collecting the spectrum at several points along the fiber. **b.** corresponding SNAP spectrogram in 2D.

Chapter 3

SNAP induced by pulling a fiber

In this chapter, we re-purpose the well-established flame brush method for pulling optical fibers [97] into a technique for the creation of SNAP resonators. This is similar to the recently demonstrated creation of parabolic SNAP resonators by pulling a fiber using a laser-heated furnace [98]. Although current fabrication methods are accurate in producing the desired variation of effective radius, they require specialized equipment and supplies that might not be easily available, such as a CO₂ laser or photosensitive fibers.

We show that it is possible to lift these requirements, allowing for the creation of SNAP resonators in any facility already equipped with a basic flame brush set-up. We characterize the resonators resulting from our fabrication by evanescent spectroscopy, using a tapered optical fiber for coupling. The transmission spectra show that light can be fully localized by just pulling a fiber using a flame, and that the created resonators can host very low loss resonant modes. To further characterize the resonators we also evaluate the transmission spectrum for different gap separations between the resonator and tapered fiber.

3.1 Fabrication

The starting stock for the fabrication of SNAP resonators is conventional single-mode optical fiber (Corning *SMF-28E+* in our case) with an initial diameter of 125 μm . WGMs are probed in the fiber by physically contacting a microfiber at a 90-degree angle. The microfiber, shown

in Figure 3.1, is fabricated from the same stock fiber, and has a biconical taper with a diameter at the waist estimated to be in the order of $1 \mu\text{m}$ [99]. Unless otherwise indicated, the tapered optical fiber was positioned in physical contact with the SNAP resonator. Details of microfiber fabrication can be found in [70].

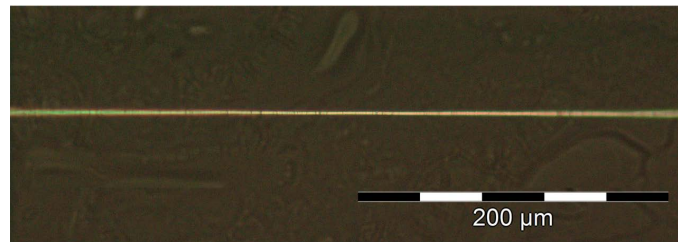


FIGURE 3.1: Optical microscopic image of a microfiber.

Before fabrication, the protective polymer buffer is removed mechanically from a section of the fiber. The stripped length is around 20 mm . The bare fiber is then cleaned with a wipe wet with isopropyl alcohol to remove dust and any remnants of the buffer coating. After stripping and cleaning, the fiber is scanned with a microfiber to ensure that the polymer jacket was completely removed without damage to the glass surface. Figure 3.2 shows a microscopic image of a tapered fiber on the top of the optical fiber.

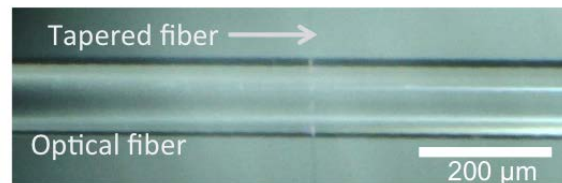


FIGURE 3.2: An optical microscopic image of an optical fiber with radius of $125 \mu\text{m}$ and a tapered fiber.

The WGM spectra of the cleaned section of fiber were measured at microfiber positions spaced by $10 \mu\text{m}$ in a 50 nm bandwidth (1550 nm to 1600 nm) along the fiber axis. In order to increase the efficiency of the process, we use an AutoHotkey script to collect the data (See Appendix A). Also, we write Python scripts to plot our spectra (See Appendix B). Figure 3.3 shows the results of these measurements. The transmission spectrum as a function of the microfiber position (the position spectrogram) shows straight lines, corresponding to WGMs in a glass cylinder, with a free spectral range (FSR) of 4.38 nm . Using that

$$FSR = \frac{\lambda^2}{(n\pi D)} \quad (3.1)$$

where D is the fiber diameter and we assume that the refractive index is $n = 1.46$, we find that the measured FSR is consistent with the expected fiber diameter of $125 \mu m$. The fact that the lines denoting the absorption due to the WGMs in the fiber are straight indicate that the diameter of the fiber is essentially constant [96] and that the mechanical stripping did not create significant damage in the fiber surface. The small perturbations that can be observed in the spectra are most likely due to a combination of laser jitter and possible small remainders of the polymer coating.

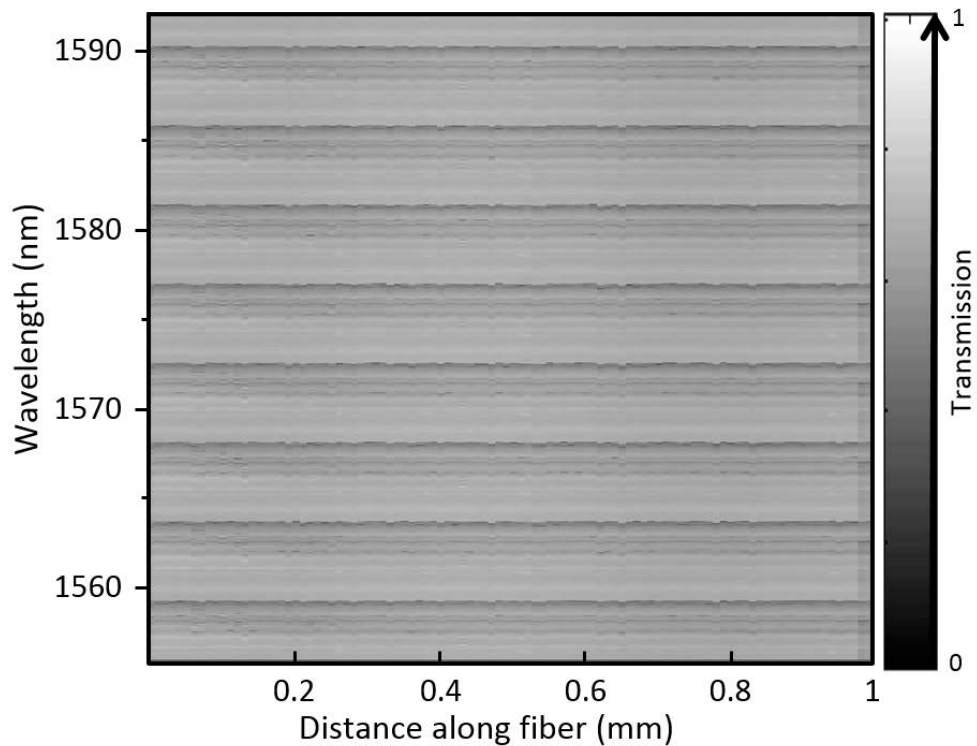


FIGURE 3.3: Position spectrogram of a fiber after mechanical stripping and cleaning, before any further processing.

3.2 Characterization

Figure 3.4 shows the set-up used to characterize our device; each component is introduced in Table 3.1. A schematic of the experimental set-up is shown in Figure 3.5.

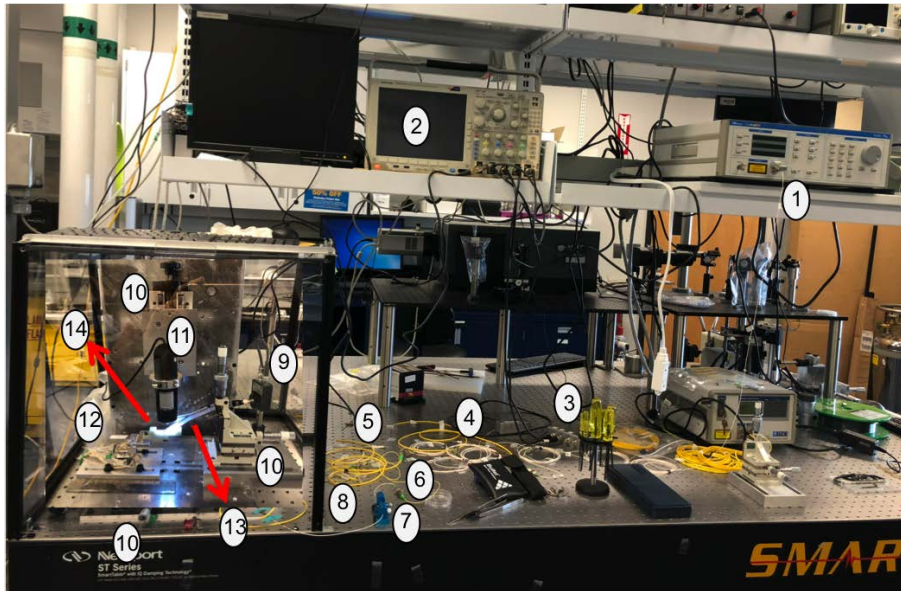


FIGURE 3.4: Overview of the SNAP microresonator characterization station. Details are given in Table 3.1.

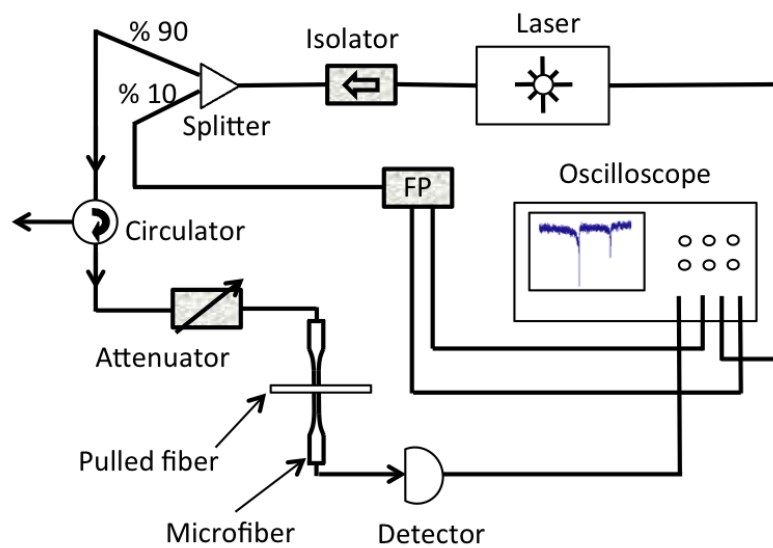


FIGURE 3.5: A schematic of the characterization set-up of a SNAP device.

TABLE 3.1: Components of characterization system

number	Component	Company	Description
1	Tunable Laser	GN-Nettest	<i>TUNICS-plus 3644HE-15</i>
2	Oscilloscope	Tektronix	<i>MDO 4034</i>
3	Fabry-Perot Wavelocker	JDS Uniphase	<i>FPWL 211501100</i>
4	Splitter	Fiber Optics Communications Inc.	<i>C-WS-AL-05-S-1210-15-AP/AP</i>
5	Circulator	New Focus	<i>CIR10BN32N – 01</i>
6	Isolator	E-TEK	<i>IWDMA410CRV06</i>
7	Fiber Polarization Controller	OZ Optics	<i>FPC – 100</i>
8	Attenuator	OZ Optics	<i>172766 – 001</i>
9	Photo-diode Detector	Thorlabs	<i>PDA – 10CF</i>
10	Manually stages	Various	—
11	Optical microscope	Veho	<i>VMS – 460</i>
12	accurate stage	Micronix USA	<i>PPS – 20 ($\times 3$)</i>
13	TF holder	—	—
14	SNAP holder	—	—

To measure the resonant spectrum of WGMs, light is sent from a tunable laser (with a tuning range between 1500 nm and 1600 nm) through the microfiber. We use a manual polarization controller to match the polarization of the light in the microfiber to that of the resonant modes in the SNAP resonator. The output of the microfiber is collected at an amplified photodiode which is connected to a digital storage oscilloscope for data acquisition. The laser wavelength is scanned in a range typically going from 1550 nm to 1600 nm in order to capture more than one group of resonant modes.

In order to reduce the diameter of the fiber, increase the FSR, and induce light localizing structures, we use the flame brush technique with a hydrogen-oxygen flame. We use an oxyhydrogen torch (SRA-250 H₂O Hydrogen torch), whose flame temperature ranges between 1200°C and 1500°C, with an American wire gauge (AWG) 30 torch tip. The recipe and details of this fabrication is described in detail in [70]. We typically pull until the fiber diameter is near 20 μm , trying to minimize the resonator mode volume without incurring significant radiation losses [100].

Figure 3.6 shows the optical image of coupling light between one of our microresonators with a tapered fiber. Here, light is sent to the tapered fiber from a tunable laser (Toptica, with a tuning range between 815 nm and 855 nm).

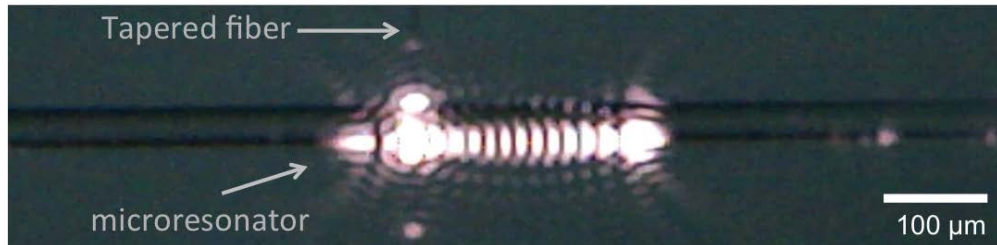


FIGURE 3.6: An optical microscopic image of a typical our microresonator with radius of $\sim 20 \mu m$ and a tapered fiber.

Figure 3.7 provides example time-lapse images of light coupling into a SNAP microresonator during scanning with a microfiber from wavelength 935.5 nm to 920.5 nm at 0.6 nm/s . The corresponding video may be viewed on youtube thorough: <https://youtu.be/N0ghwZeIm8Q>. Different modes occur in different positions along the SNAP microresonator which correspond to different dips on the transmission spectra.

3.3 Results

While it would be a reasonable assumption to consider that the tapering of the fiber would leave a smooth surface, the pulling process itself creates non-uniformities with an ERV large enough to provide complete localization of light [97]. Figure 3.8 shows the position spectrogram of a fiber pulled to a diameter of 22 μm . It can be seen from the data that light can be fully localized in at least four different positions along the pulled fiber.

Before focusing on the details of the light confinement that can be found on the pulled fiber, a different point is discussed. According to the analysis of the fabrication of SNAP resonators with a CO_2 laser, the localized heating with the laser releases some of the strain that is introduced during the fiber pulling [28]. This release of strain then results in the ERV that creates light confinement. It would then seem that a localized anneal with the torch may result in a similar process, creating a SNAP resonator in a predetermined position in the pulled fiber. We tried

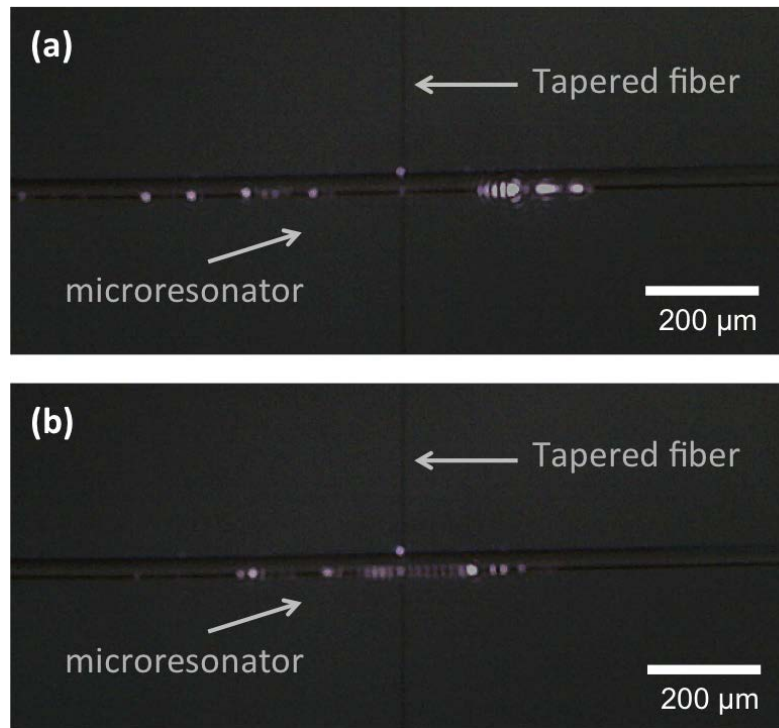


FIGURE 3.7: Optical microscopy images captured from the video (<https://youtu.be/NOghwZeIm8Q>) recorded during scanning a SNAP resonator with a microfiber from wavelength 935.5 nm to 920.5 nm at 0.6 nm/s **a.** 18 sec, and **b.** 24 sec.

this by briefly passing the torch under a specific position on the already pulled optical fiber. The resulting position spectrogram is shown in Figure 3.9.

The spectrogram shows clear changes in the region treated with the flame, where the spectrum loses any localization it may have had before the treatment. Figures 3.10(a) and 3.10(b) show the optical microscope image of the pulled fiber coupled to an input-output microfiber before and after passing the flame, respectively. A comparison of Figs. 3.10(a) and 3.10(b) shows that the localized treatment led to a deformation in the pulled fiber. We speculate that this is due to the flame excessively softening the glass, leading to a significant and unpredictable change in the local properties of the fiber that eliminates the previously seen optical confinement. Figure 3.9 shows that the regions not affected by the flame still show evidence of localization of light.

Let's now turn the attention to the characteristics of the optical confinement obtained right after the fiber pulling. Table 3.2 shows a summary of the characteristics of four SNAP resonators created by pulling the fiber. The first two SNAP resonators are close enough to interact with

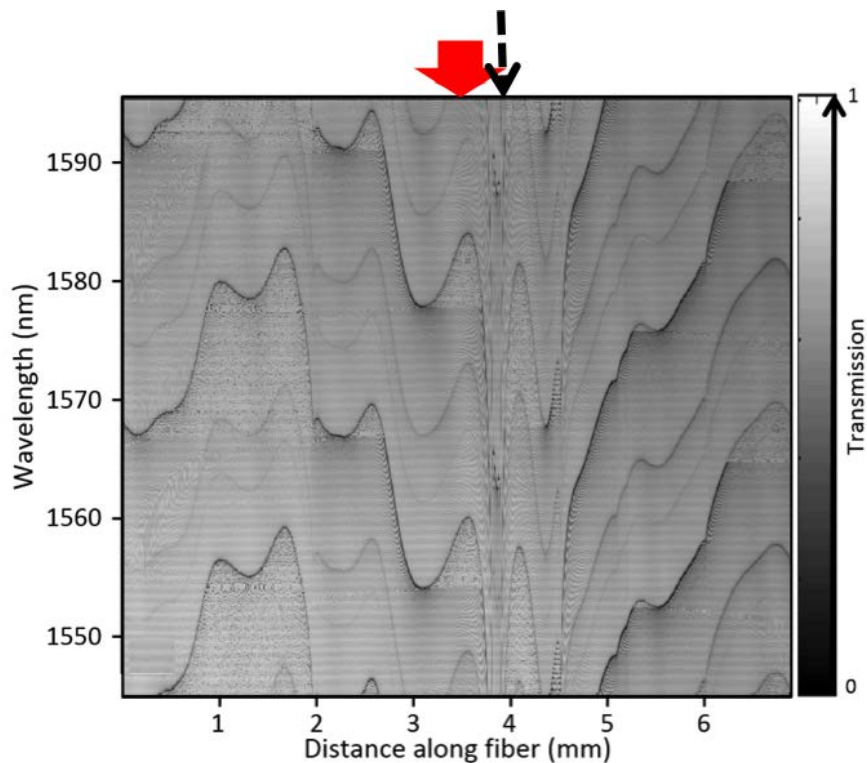


FIGURE 3.8: Position spectrograms along 7 mm of the pulled fiber before passing the torch. The spatial resolutions of the scans was 10 μm .

each other and make a single coupled-resonators system [92]. The effective radius variation and the extent of each SNAP resonator are also estimated. The height of the introduced ERV is estimated as $\Delta r_0 \sim \Delta \lambda_0 r_0 / \lambda_0$, where $\Delta \lambda_0$ is the spectral distance between the base and the peak of the SNAP, r_0 is the reference radius, and λ_0 is the wavelength near the mid-height of the SNAP in the spectrogram. For instance, the length of resonator number 4 was $\sim 0.58 \text{ mm}$. From Figure 3.8, the spectral width of this resonator is $\Delta \lambda_0 \sim 5.95 \text{ nm}$ at a radiation wavelength of $\lambda_0 \sim 1.56 \mu\text{m}$. The height of the introduced ERV is then estimated as $\Delta r_0 \sim 42.0 \text{ nm}$.

TABLE 3.2: Resonator properties

SNAP	Position [mm]	ERV Δr_0 [nm]	Extent [mm]
1	0.96	91.76	~ 1.56
2	1.63	110.77	~ 1.56
3	2.53	19.14	0.36
4	3.51	42	0.58

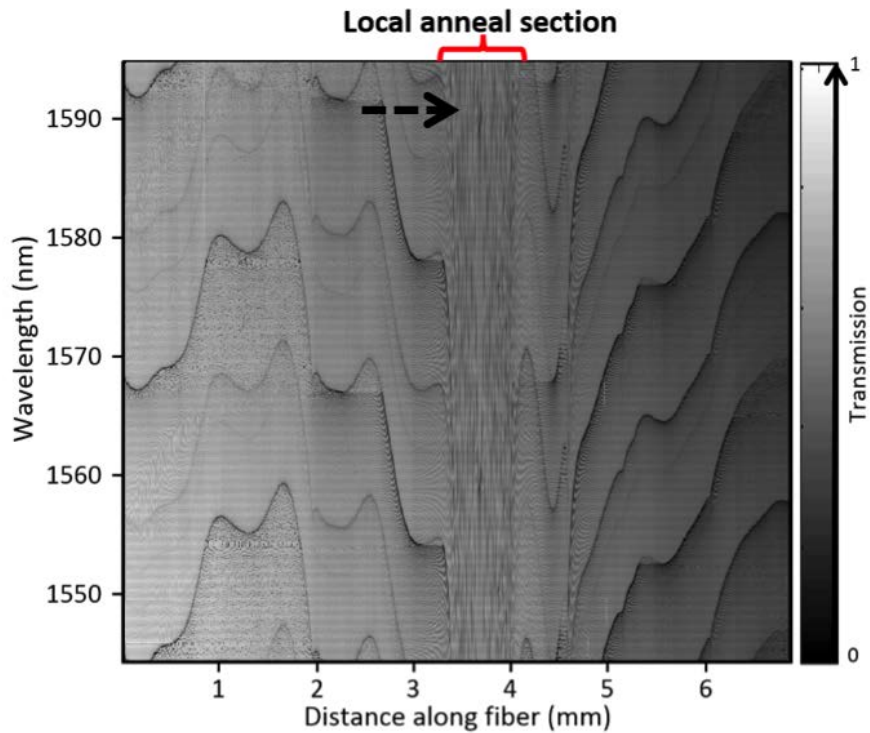


FIGURE 3.9: Position spectrograms along 7 mm of the pulled fiber after extra annealing. The spatial resolutions of the scans was 10 μm .

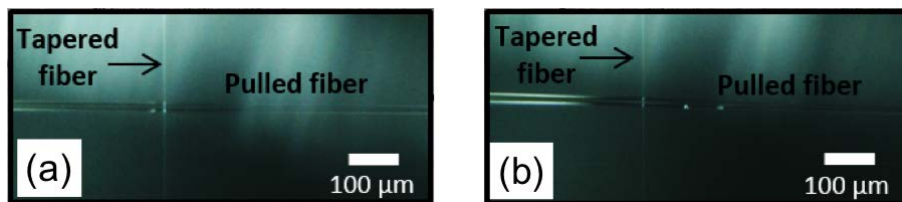


FIGURE 3.10: **a-b.** Optical microscope image of the pulled fiber and a tapered fiber before passing the torch and after extra annealing, respectively. The thin black arrows in Figure 3.8 and 3.9 indicate the position corresponding to each image.

We will concentrate now on one particular spectral slice, belonging to the SNAP resonator number 4, and marked by the red arrow in Figure 3.8. This spectrum is displayed in Figure 3.11, which clearly shows two groups of modes. The FSR calculated by the spectral separation between these groups of modes is $\sim 24.8 \text{ nm}$, consistent with our measured diameter of 22 μm .

In order to better understand the mode structure, we zoom into the first group of modes, changing the abscissa to frequency. The result is shown magnified in Figure 3.12. Many sharp lines, corresponding to different axial modes, in this magnified view can be observed. The

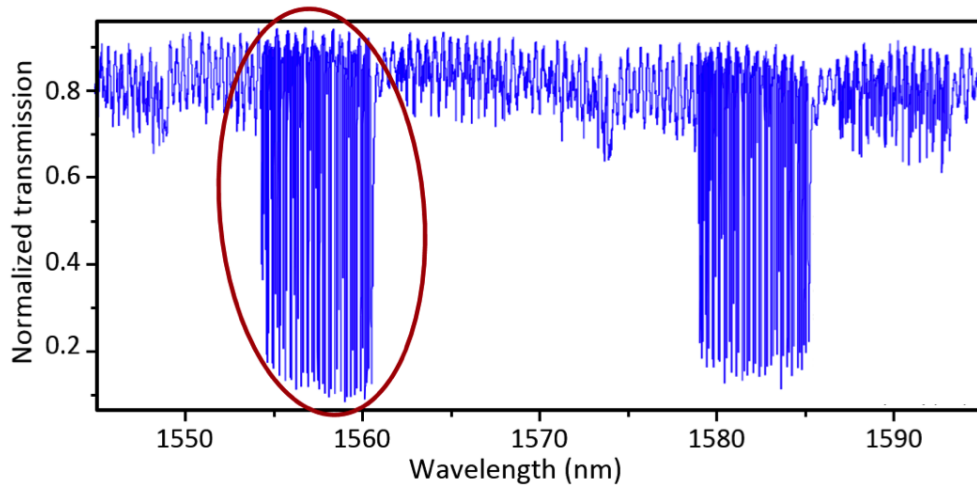


FIGURE 3.11: Normalized transmission response of the fabricated SNAP at its central position.

azimuthal quantum number (assuming the mode group to correspond to the fundamental radial mode) as $m \sim 2\pi nr_0/\lambda_0$, where n is the refractive index of the fiber can be estimated. For a silica fiber, $n = 1.46$ and we find $m \sim 65$. As the spectrum has been plotted as a function of frequency, it can be clearly appreciated that the spacing between the modes is not constant, becoming smaller at higher frequencies. This indicates the fact that our SNAP resonator does not possess a parabolic change in its ERV. This agrees with the observed shape of the resonator envelope in Figure 3.8, which is not symmetric respect to its central axis.

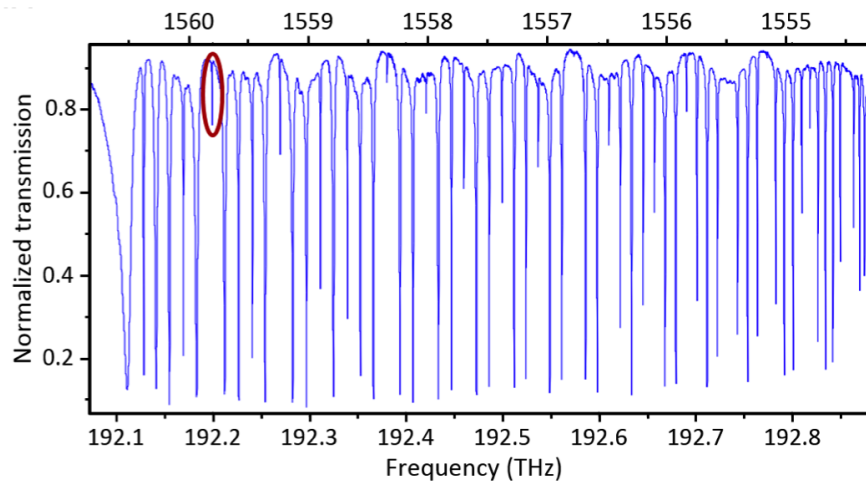


FIGURE 3.12: Magnified spectral region of the spectrum plot showing a single group of modes.

Finally, the quality factor of the narrowest resonant mode in the lower frequency side of the

spectrum, which is plotted in Figure 3.13 is estimated. The loaded quality factor of this mode has a value of 7.4×10^5 , which is very high.

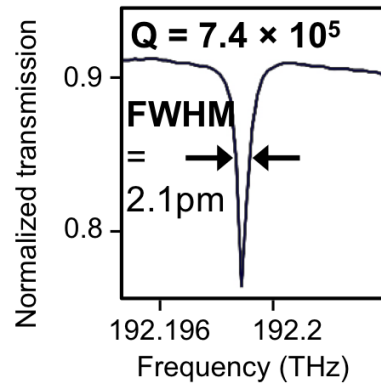


FIGURE 3.13: Detail of the resonance of the mode indicated by the red ellipse in Figure 3.12.

We also investigated the transmission spectrum for different gaps between the SNAP resonator and the microfiber for the first resonant mode in Figure 3.12 (at 192.112 THz or 1560.51 nm). This allows us to get a better view of the intrinsic characteristics of the mode, as well as determining the coupling regime when the microfiber and resonator are in contact. These spectra are shown in Figure 3.14, with the gap decreasing in the upward direction. It can be clearly seen that decreasing the gap leads to increased coupling, resulting in more absorption by the mode and therefore some broadening. As the gap decreases, the system reaches critical coupling and then goes into the overcoupling regime (where a small but consistent red-shift can be seen). Not long after the transition to the overcoupling regime, the gap has decreased enough for the microfiber to stick to the SNAP fiber and remain in physical contact with it. At this point, a maximum red-shift of 29 pm in the resonant mode can be observed, due to the contact between the fiber and resonator. The loaded Q factor closest to critical coupling is 10^5 , which corresponds to an intrinsic Q-factor for the mode of approximately 2×10^5 .

Considering the experimental characterization of the flame- formed SNAP resonators we can see that they can hold a large number of modes with very low optical losses, and the expected rich but understandable bottle-like mode structure [101], the formation of SNAP resonators is not as predictable as those methods using a localized treatment. Nevertheless, in our experience the pulling always induces at least one SNAP resonator with mode structures similar to those described here. Due to the variability, we would not recommend our method to make devices

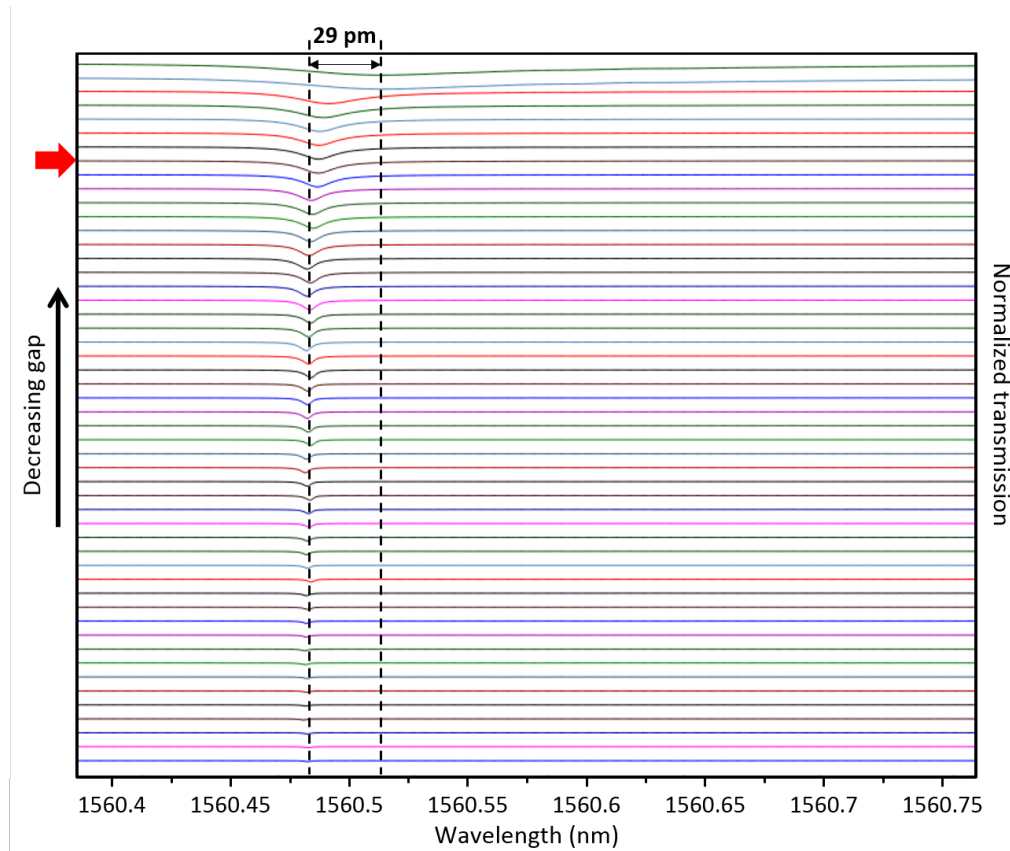


FIGURE 3.14: Transmission spectra for different separations between the resonator and tapered fiber. The gap decreases in the upward direction, and the top spectrum corresponds to the resonator and microfiber being in physical contact. The red arrow indicates the trace closest to critical coupling.

requiring specific positioning or geometry of the SNAP (like optical delay lines or frequency combs, in that case a laser heated furnace will produce more reproducible results [98]). The method will be much more useful for applications where only the presence of low-loss modes is required, without concern about the specific mode structure and dispersion, such as optical label-free sensing [102].

3.4 Summary

In summary, a very simple technique for inducing localization of light based on pulling a conventional single mode optical fiber have introduced. By using the flame brush technique with a

hydrogen-oxygen torch, and no other equipment, we made a number of SNAP microresonators in a fiber. This method is very straightforward and easy to replicate. SNAP spectrograms to estimate the number and spatial extent of the formed resonators have measured. By looking in detail at the mode structure in a fabricated SNAP resonator, we see that our flame-fabricated SNAPs have non-parabolic shapes, and that they have the potential to host very low loss resonant modes. The variation of the spectrum of a fabricated microresonator as we changed the separation between the resonator and the coupling microfiber has investigated, mapping the coupling regime from undercoupled to overcoupled. We believe that future development and optimization of this technique will allow for the fabrication of more complex SNAP resonator profiles with even higher Q-factors. Generally, a very simple, fast, and easy to implement method for the fabrication of very low loss microresonators has provided.

Chapter 4

SNAP at a capillary fiber

Hollow WGM resonators have been successfully explored in the context of sensing [103], since their open inside region allows for flowing gases or liquids that modify their optical properties. Most hollow WGM resonators are in the form of tubes, bottles, or spheres. The sensing platform developed in this chapter extends the surface nanoscale axial photonics (SNAP) platform to the case of thin-walled capillary fibers, including those filled with gas, liquid, or solid media. In particular, this approach based on coupling between WGMs and the interior of the thin-wall microresonator promises further improvements in the sensitivity and precision of capillary microfluidic sensors. The evanescent tail of a WGM localized inside the wall of a capillary microresonator penetrates into the interior region and can be used as a probe of the interior medium.

Here, we explore WGMs, which circulate inside the capillary wall and slowly propagate along the capillary axis for sensing the media adjacent to the internal capillary surface and, specially the nonuniformity of the internal surface itself. The wavelength of WGMs considered is very close to their cutoff wavelength. For this reason, the propagation constant of these modes is small and their speed along the capillary axis is slow [4]. It has been shown that the axial distribution of slow WGMs is sensitive to extremely small nanoscale variations of the optical fiber radius. In the case of a capillary fiber, it is of great interest to investigate how the spatial and temporal variations of the media adjacent to the internal capillary surface affect the spectrum of the SNAP resonator created at the capillary wall. It is important to find out if it is possible to

determine the internal effective radius variation of the capillary from the measured spectra, as was done for the outer radius in SNAP.

In this chapter, first, we explain briefly the fabrication process of the micro-capillary fiber, the fabrication technique that we used to make a tapered fiber from a single mode fiber and a SNAP microresonator on the surface of a capillary. We then describe the method used for the characterization of the SNAP devices. Finally, we describe the process of etching, followed by a presentation of some of our spectroscopy results.

Using a SNAP resonator at the capillary surface allows to significantly advance this method. In particular, this approach potentially enables the regeneration of the spatial distribution of refractive index of fluid flowing inside the core of the capillary from the resonator spectrum and consequently sensing and manipulation of fluid components, at the same time. The work presented in this chapter is adapted from the following publications [104] and [105]. This work was conducted at Aston Institute of Photonics Technologies (AIPT), Birmingham, UK.

4.1 Fabrication

Fabrication of the sample has three sections which are explained here.

4.1.1 Fabrication of the micro-capillary

The capillary fiber was drawn at OFS Laboratories from a tube-shaped preform fabricated of pure silica. The wall thickness of the capillary was controlled by the original dimensions of the tube and internal pressure introduced in the process of drawing. The capillary fiber was coated with a protective polymer. In this experiment, we removed the polymer coating in hot sulfuric acid and cleaned the extracted silica capillary in deionized water. After stripping the capillary, we scanned the surface of the capillary with a tapered fiber, to make sure the polymer jacket was completely removed. Figure 4.1 shows the measurements mode of the capillary surface. The method of measurement is explained in detail in section 3.2. We can see that we still have some remainders at the surface of the capillary. In particular they will disappear when we introduce a SNAP structure. The spectra resolution of the spectrum is $2\mu m$.

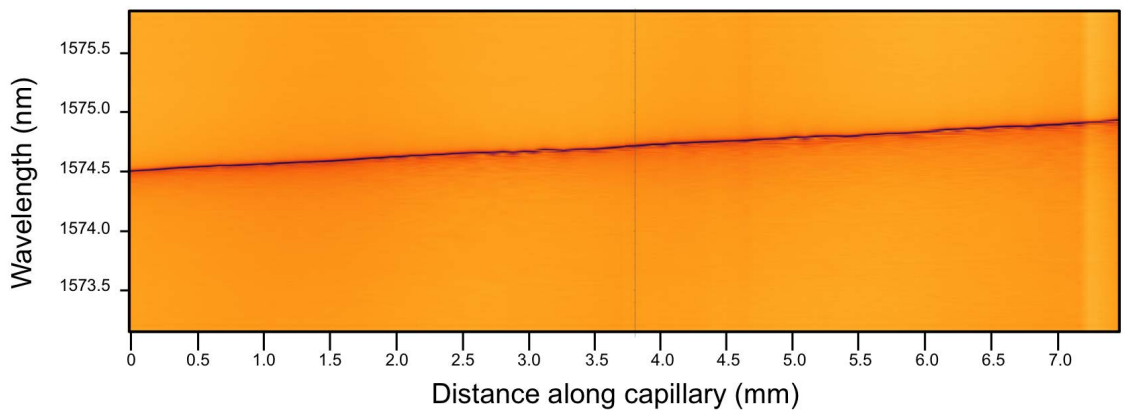


FIGURE 4.1: Scanning 7.5mm of surface of the capillary with a tapered fiber.

4.1.2 Fabrication of the tapered fiber

For a coupling the light in to the SNAP microresonator we are using a tapered fiber as a waveguide, which generates a strong evanescence field. The tapered fiber has a micron diameter waist, and it was fabricated from a conventional single mode fiber. First, we stripped the polymer coating from single mode fiber. Then we aligned it inside a sapphire capillary, while heating with the CO_2 laser. The tapering method, which included pulling the fiber with two linear stages, was similar to the flame-brushing method developed for the fabrication of bionically tapered fibers softened in flame, which we are using in our lab currently at Concordia University.

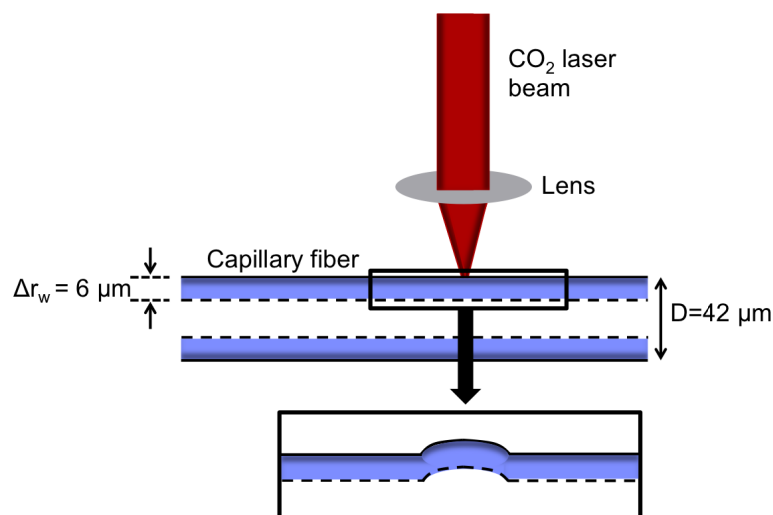


FIGURE 4.2: A schematic of fabrication method of SNAP with CO_2 laser beam.

4.1.3 Fabrication of SNAP microresonator

The fabrication is based on modification of the density and refractive index of the capillary fiber material. We are using a silica fiber capillary with external radius of $21\mu m$ and initial wall thickness of $6\mu m$. We focused the CO_2 laser beam on the surface of capillary. Figure 4.2 shows a schematic of this process. By a local annealing, when the strain is realized, we can make a nanoscale variation on the surface of the capillary.

Thus, we used this method and introduced an asymmetric SNAP microresonator at the capillary surface.

4.2 Characterization

We use the method which is described in 2.7 and we put the tapered fiber at different position along the capillary and measure the WGM spectra of the SNAP. Figure 4.3 shows the spectrum of our SNAP microresonator. At different spatial positions, we can observe distinct patterns in the spectra, corresponding to coupling to different axial modes. Here, the tapered fiber positions are spaced by $20\mu m$ along the capillary axis. From this Figure, we can infer an spatial extent of $300\mu m$ for the SNAP microresonator along the capillary. From Figure 4.3, the spectral width of resonator is $\Delta\lambda_0 = 0.15nm$ at a radiation wavelength of $\lambda_0 \approx 1.57nm$. The height of the introduced external effective radius variation (ERV) is estimated as $\Delta r_0 = \Delta\lambda_0 r_0 / \lambda_0 \approx 2nm$. The resonant spectra shown in this Figure has the azimuthal and radial quantum numbers of $m \approx 2\pi n_{cap} r_0 / \lambda_0$ and $P = 0$, respectively. For a silica capillary with $n_{cap} \approx 1.46$, we have $m \approx 122$.

The power of the laser beam and the radiation time of the laser pulse can play important roles in the process of producing a SNAP. If the power is low, the variation of the surface will be shallow, the spectral width of resonator will be small, and since the axial resonances are close to each other, it is not easy to distinguish them. A small change in the power of laser produces a significant change in the capillary surface (see Figure 4.4(a)). This can be explained by Figure 4.5 [106]. Silica is an amorphous (non-crystalline) material, and with increasing temperature, volume increases. Thus, the best power for making a SNAP is when the transition temperature

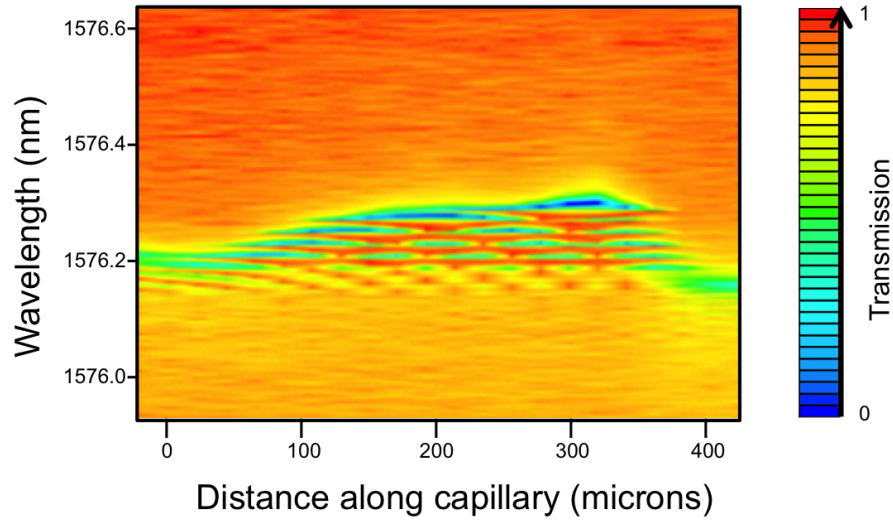


FIGURE 4.3: Surface plot of spectra of the fabricated SNAP resonator measured with $20\mu\text{m}$ resolution along the capillary axis [105].

is smaller than the melting temperature (t_m) of the silica. If the power of laser is too high, the capillary surface will be deformed (see Figure 4.4(b)).

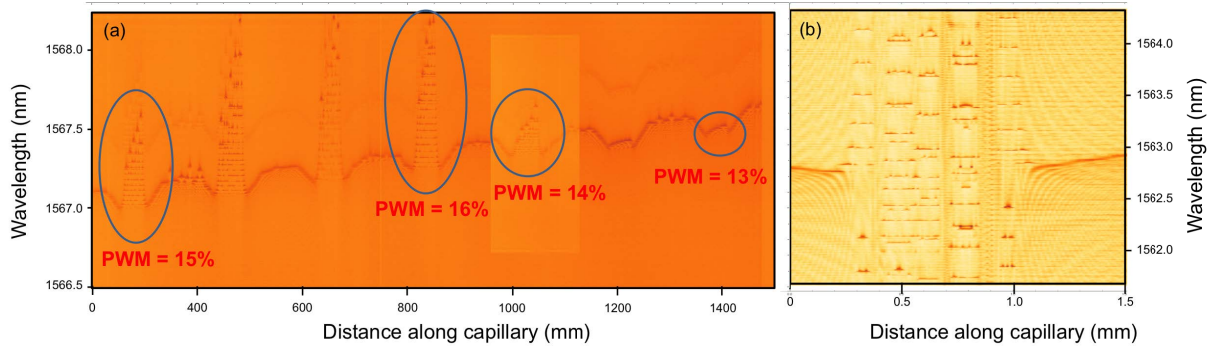


FIGURE 4.4: The surface plots of the transmission power spectra show the effect of power of laser on the surface of a capillary. **a.** Four SNAP resonators are produced with the laser power of 15%, 16%, 14%, and 13%. They have the same radiation time = 0.5s , the relaxation time = 10s , and the distance between each position of pulse = $70\mu\text{m}$. **b.** The power of laser was higher than the melting temperature of silica, the surface of capillary is deformed.

4.3 Etching

As we reviewed in the chapter 1, for the capillary with the original wall thickness of $6\mu\text{m}$ (see Figure 4.6), the WGM spectrum of the SNAP microresonator was not that much sensitive to

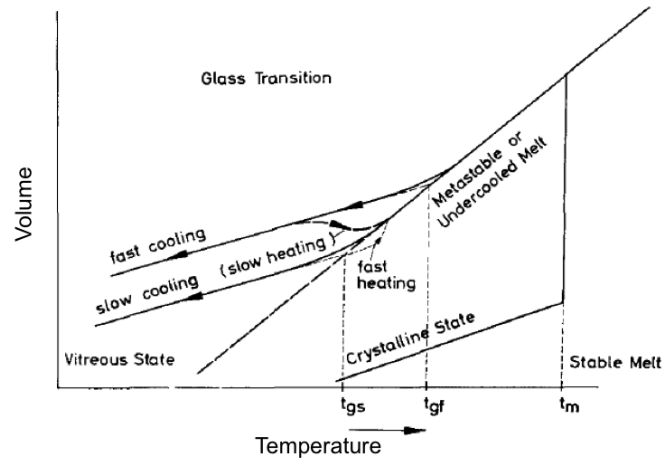


FIGURE 4.5: Typical glass transition volume-temperature dependence, t_{gs} is the glass transition temperature for slow cooling, t_{gf} corresponds to the glass transition temperature for fast cooling, and t_m is the melting temperature. Figure is from [106].

the presence of water, used as micro-fluid in our experiment. Thus, in order to enhance the sensitivity we etched the internal capillary surface with hydrofluoric acid to reduce the wall thickness, and simultaneously controlled the process of etching by monitoring the resonance spectrum.

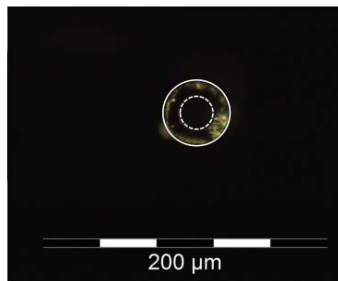


FIGURE 4.6: The optical microscope image of the cross-section of the silica microcapillary used in the experiment.

Figure 4.7 shows our etching set-up used to internally etch the capillary; each component is introduced in Table 4.1. A schematic of the etching set-up is also shown in Figure 4.8. The set-up consists of two containers and one syringe. We fill one of the containers with the dilute HF, put a tapered fiber close to the capillary and monitor the spectra in an optical spectrum analyzer (OSA). The syringe pump produces vacuum in the second sealed container, and therefore, the HF flows in the capillary. The whole process is done in the clean room, under the fume hood. The etching process is stopped after we observe a shift of the axial resonance modes in the

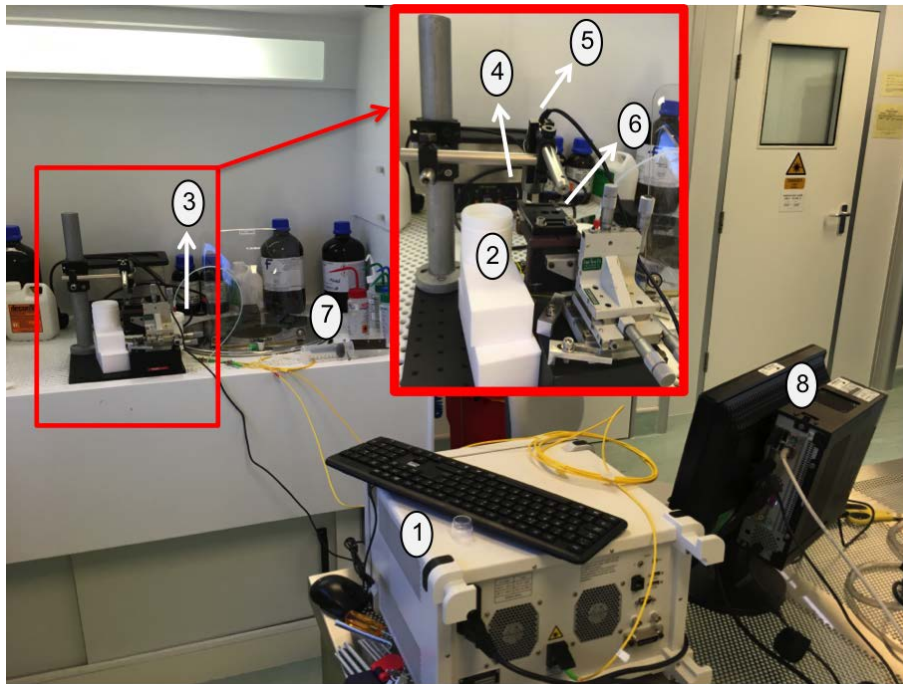


FIGURE 4.7: Overview of etching process. Details are given in Table 4.1.

TABLE 4.1: Components of the etching set-up

number	Component	number	Component
1	Apex analyzer	5	Optical microscope
2	HF container	6	Capillary fiber
3	Vacuum container	7	Syringe pump
4	Tapered fiber	8	Monitor

spectra as shown in the following video: https://www.youtube.com/watch?v=Zg1dbp_0LU8.

We remove the capillary from the HF container and put it in deionized water to rise inside and outside with water.

After the etching, we take a spectra of our etched capillary.

4.4 Results

Figure 4.9(a) shows the SNAP resonator spectra for the capillary after etching, which shows strong modifications. It is seen that the axial WGM resonances near to the cutoff wavelength

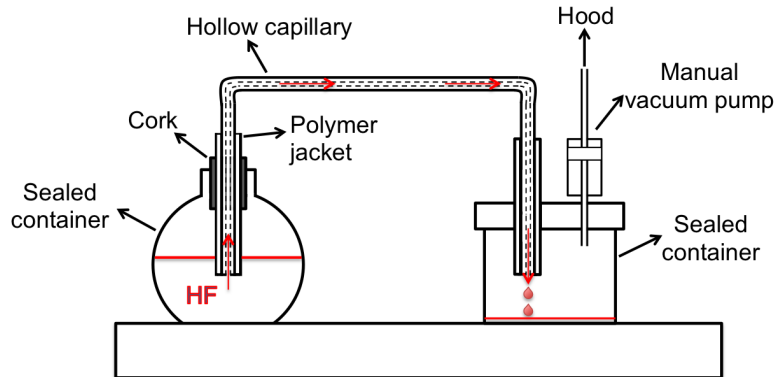


FIGURE 4.8: A schematic of etching process.

with the fundamental radial number series ($P = 0$, $q = 0, 1, 2, \dots$, bottom) experience relatively small distortion. However, the axial resonances of WGMs with a larger radial quantum number (hypothetically the $P = 1$ series, top) change dramatically. In addition, the $P = 0$ axial resonances are narrower, which means they are less lossy than the $P = 1$ resonances, due to the fact that they have less overlap with the internal surface of the capillary.

The dramatic shrinking of the $P = 1$ WGMs compared to the $P = 0$ WGMs along the axial direction can be explained by axial non-uniformities introduced by hydrofluoric etching. We suspect that the CO_2 laser annealing deforms the capillary wall as a whole. This deformation disturbs the hydrofluoric acid flow and leads to the creation of a bump of the capillary wall illustrated in the inset of Figure 4.10. While the $P = 0$ WGM series have small overlap with the internal wall surface and, therefore, are not noticeably sensitive to the appearance of this bump, it causes an evident additional localization of the $P = 1$ WGMs.

Now we fill our etched capillary with the water. Comparison of Figures 4.9(a) and 4.9(b) shows that filling the capillary with water led to a reduction in the separation between the axial series of resonances with different axial quantum numbers q clearly seen for the fundamental radial mode of $P = 1$ series. In our experiment, adding water introduced a shift of the SNAP microresonator spectrum by 0.13 nm for the first axial fundamental resonance $q = 0$. This shift is presumably due to mechanical deformation of the capillary pressurized by water.

When we zoom in the $P = 0$ radial resonances series (see Figures 4.11(a) and 4.11(b)), we notice that the separation of the resonant wavelength of the fundamental axial modes with $q = 0$ did

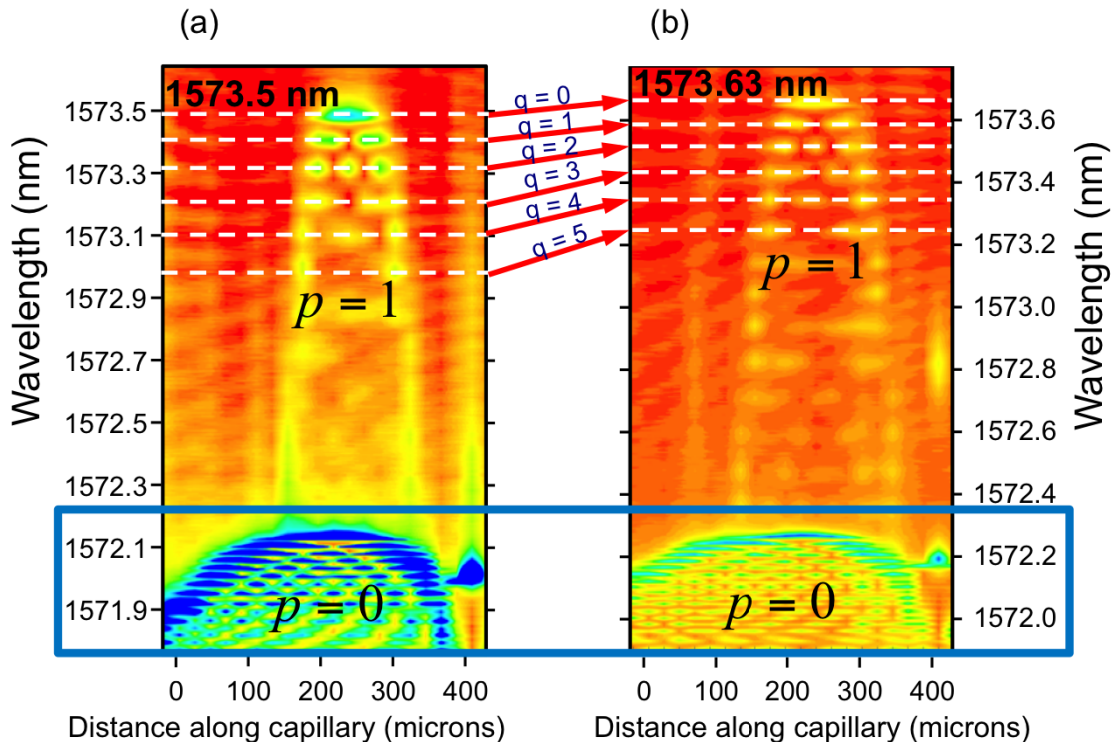


FIGURE 4.9: Surface plots of spectra of the fabricated SNAP microresonator measured with $20\mu m$ resolution along the capillary axis. **a.** After etching, empty capillary, $P = 0$ (bottom) and $P = 1$ (top). **b.** After etching, capillary filled with water, $P = 0$ (bottom) and $P = 1$ (top) [104].

not significant change.

This fact confirms, again, that the capillary wall thickness in the region of localization of fundamental axial WGMs was large enough. However, the effect of water on the resonance shift increased with axial quantum number q . As we expected, this shift is significantly smaller for the $P = 0$ series.

We used the developed theory in the section 2.4.2 to estimate the internal ERV, $r_{int}(z) = r_{int}^{(0)} + \Delta r_{int}(z)$, from the measured spectra of the SNAP resonator. We also numerically analyzed and compared the $p = 1$ resonances for the empty and water-filled capillaries shown in Figs. 4.9(a) and 4.9(b), respectively. The major contribution to the appearance of these resonances was caused by variation of the internal radius $r_{int}(z)$. Therefore, in our calculations, we neglected the variation of the external radius. Figure 4.12(a) compares the dependencies of the cutoff wavelength on the internal radius for $r_{int}(z) \equiv r_0 = 21.12 \mu m$, $n_{cap} = 1.46$, two azimuthal

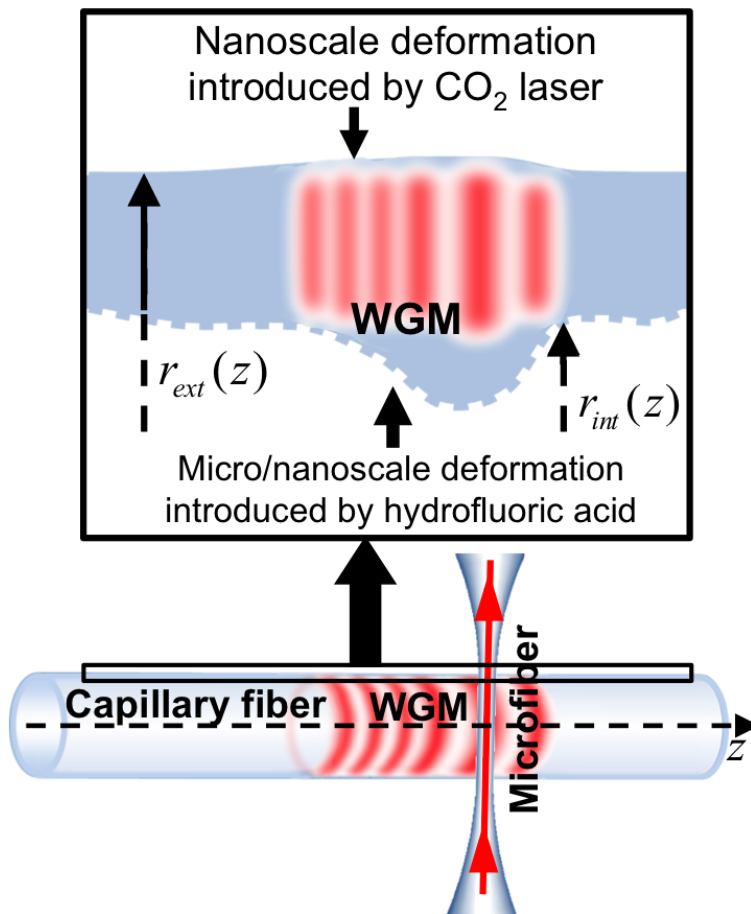


FIGURE 4.10: Illustration of a capillary fiber coupled to an input-output microfiber. The capillary is processed with a CO_2 laser beam and, internally, with hydrofluoric acid. Inset: magnified cross section of the capillary wall (not to scale) [104].

quantum numbers, $m = 113$ and $m = 105$, and three radial quantum numbers, $p = 0, 1, 2$. We suggest that our experimental situation can be approximated by the calculated behavior of the $m = 113, p = 0$ and $m = 105, p = 1$ series.

Figure 4.12(b) compares the deviations of dependencies shown in Figure 4.12(a) from their value $\lambda_{mpq}^{(0)}$ for a thick capillary ($r_{int} < 16 \mu m$) magnified to the nanometer wavelength scale of our interest. The curves in Figure 4.12(b) look remarkably similar and coincide with good accuracy after the horizontal translation into the darker rectangle in this figure. Thus, all of them can be defined by a common function $\Delta\lambda^{(cut)}(r_{int} + s)$ with the appropriate choice of shift s . Consequently, the internal ERV can be found as $\lambda_{mpq}^{(cut)} = \Delta\lambda^{(cut)}(r_{int} + s) + \lambda_{mpq}^{(0)}$. While the actual value of s is not important for the determination of *variation* of the internal radius,

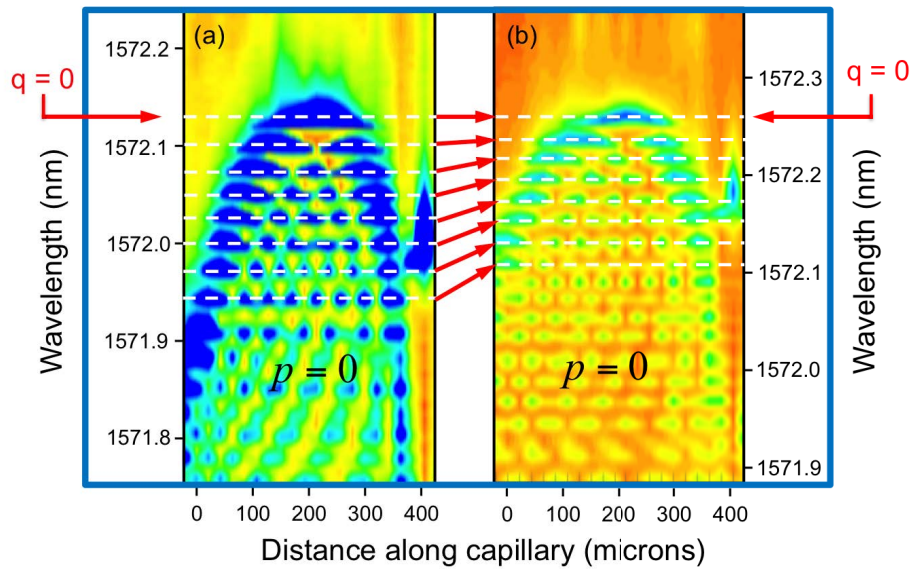


FIGURE 4.11: Surface plots of spectra of the fabricated SNAP microresonator. **a.** After etching, empty capillary, showing fundamental $P = 0$ radial series. **b.** After etching, capillary filled with water, showing the fundamental $P = 0$ radial series [105].

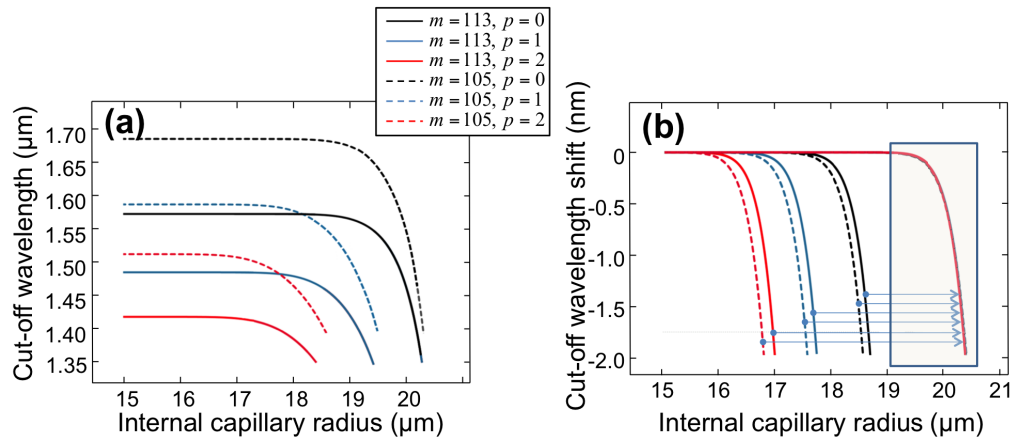


FIGURE 4.12: **a.** Cutoff wavelength as a function of internal ERV for the quantum numbers indicated on the plot. **b.** Dependencies shown in (a) magnified and shifted along the vertical axis [104].

the direct application of this result to our experiment is complicated because the accurate measurement of $\lambda_{mpq}^{(0)}$ is not possible.

To solve this problem, we proceed as follows. Figures 4.13(a) and 4.13(b) compare the behavior of cutoff wavelength with $m = 113$ and $q = 0, 1, 2$ for the empty capillary and the capillary filled with water. These dependencies, again, coincide with a good accuracy after horizontal

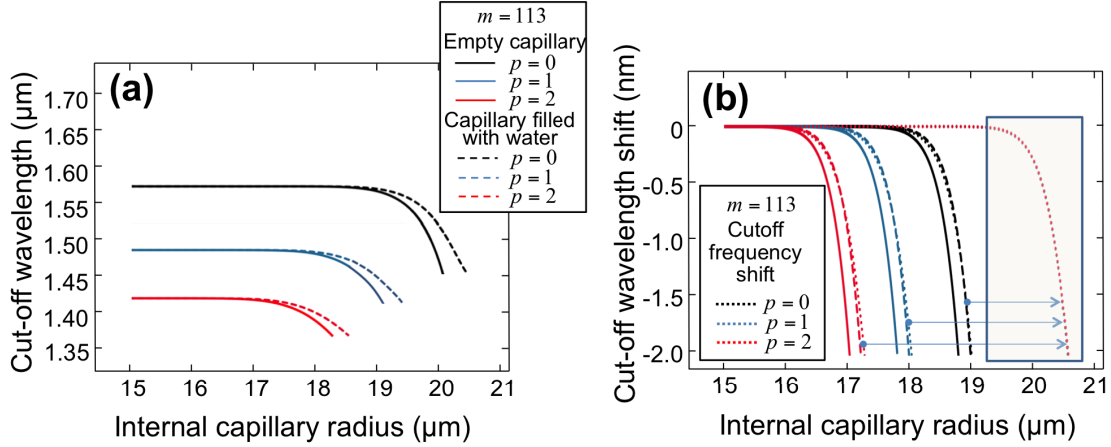


FIGURE 4.13: **a.** Cutoff wavelength as a function of internal ERV for the empty and water-filled capillaries for the quantum numbers indicated on the plot. **b.** Dependencies shown in 4.13(a) magnified and shifted along the vertical axis. Curves shown in 4.12(b) and 4.13(b) are compared by horizontal translation into the darker rectangles. [104].

translation [they are compared in the darker rectangles of Figures 4.13(a) and 4.13(b)]. In particular, the shift of the cutoff wavelength caused by filling the capillary with water is defined by a common function:

$$\widetilde{\Delta\lambda}^{(cut)}(r_{int} + s) = \lambda_{mpq}^{(cut)}(r_{int} + s)|_{water} - \lambda_{mpq}^{(cut)}(r_{int} + s)|_{empty} \quad (4.1)$$

which does not depend on $\lambda_{mpq}^{(0)}$. Thus, this function does not depend on the actual values of the azimuthal and radial quantum numbers m and p , respectively, which were not precisely determined from the experiment.

In both cases of empty and water-filled capillaries, we estimate the cutoff wavelength dependency corresponding to $p = 1$ spectral series in Figs. 4.9(a) and 4.9(b) by parabolas,

$$\lambda_{water}^{(cut)}(z) = \lambda_w - \gamma_w z^2 \quad (4.2)$$

and

$$\lambda_{empty}^{(cut)}(z) = \lambda_e - \gamma_e z^2 \quad (4.3)$$

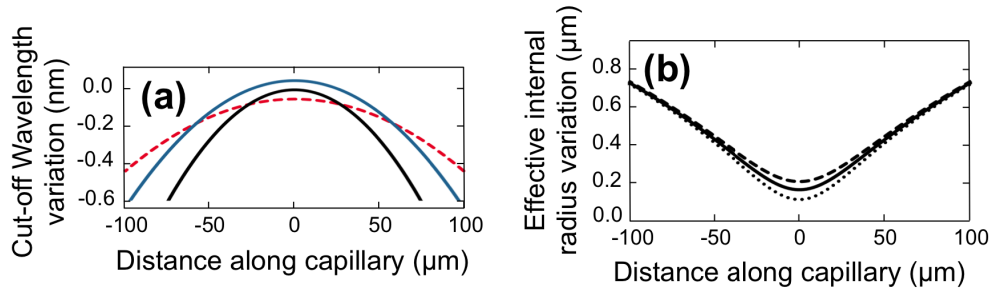


FIGURE 4.14: **a.** Parabolic approximation of the cutoff wavelength for the empty (black curve) and water-filled (blue curve) capillary. Dashed red curve is the difference of these curves. **b.** The restored internal ERV. The solid, dashed, and dotted curves correspond to $\lambda_w - \lambda_e$ equal to 0.05 nm , 0.04 nm , and 0.06 nm , respectively [104].

respectively. Here parameters $\gamma_{w,e}$ are expressed through the separation of resonances along the axial quantum number, $\delta\lambda_{w,e}$, as $\gamma_{w,e} = 2(\pi n_{cap} \delta\lambda_{w,e})^2 \lambda_0^{-3}$ [28]. From Figures 4.9(a) and 4.9(b), setting the top of the $p = 0$ resonance series as a reference (which, as noted above, has a negligible effect of water), we estimate $\delta\lambda_e \sim 0.01 \text{ nm}$, $\delta\lambda_w \sim 0.08 \text{ nm}$, and $\lambda_w - \lambda_e \sim 0.05 \text{ nm}$. Consequently, $\gamma_w = -1.1 \times 10^{-7} \mu\text{m}^{-1}$ and $\gamma_e = -6.9 \times 10^{-8} \mu\text{m}^{-1}$.

Figure 4.14(a) shows the dependencies $\lambda_{empty}^{(cut)}(z)$ and $\lambda_{water}^{(cut)}(z)$ (black and blue curves, respectively), which are translated into surface plots on Figs. 4.9(a) and 4.9(b) and show good agreement with the experiment. Finally, the black solid curve in Figure 4.14(b) shows the internal ERV $\Delta r_{int}(z)$ restored from the difference $\lambda_{water}^{(cut)}(z) - \lambda_{empty}^{(cut)}(z)$ [red dashed curve in Figure 4.14(a)] following Eq. 4.1.

This variation appears to be quite different from parabola and has the micrometer scale. In contrast, as it follows from the SNAP theory of a regular fiber [4, 29, 30], the same cutoff wavelength variation can be introduced by the external ERV $\Delta r_{ext}(z) = (\lambda_{empty}^{(cut)}(z) - \lambda_{mpq}^{(0)}(z))r_0/\lambda_0$, which has nanometer rather than micrometer scale.

4.5 Summary

In summary, we have developed a theory of a capillary SNAP platform and experimentally demonstrated a SNAP microresonator at the surface of a capillary that is sensitive to the presence of fluid inside the capillary. The resonator was created by local annealing of the capillary

with a focused CO₂ laser beam and internal etching with hydrofluoric acid. We investigated the variation of the spectra of fabricated microresonator resulted from thinning of the capillary wall and the presence of water inside the capillary. We determined the internal effective radius variation of the capillary from the spectra of the SNAP resonator measured experimentally.

We believe that the future development of the theory, which has been described in the section [2.4.2](#), will allow for the simultaneous determination of the internal and external effective radius variation of the capillary. In addition, we suggest that the developed approach will allow for the determination of the complex structure of microfluidic components adjacent to the internal capillary surface, e.g., the resonant structure of microparticles [\[107\]](#). Generally, this demonstration provides the groundwork for advanced microfluidic sensing with SNAP microresonators.

Chapter 5

Localization of light in an optical microcapillary induced by a droplet

As we show in previous chapter, light propagating in the form of a WGM along an optical fiber surface can be fully controlled by the exceptionally small nanoscale variation of the effective fiber radius [29]. In particular, the deformation of a fiber by just a fraction of a nanometer can completely localize WGMs and form a high quality-factor microresonator [28]. This means that the fiber radius variation sufficient for governing WGMs can be dramatically smaller than the wavelength of light. The technological platform based on this phenomenon — SNAP — demonstrates the fabrication of miniature resonant optical devices at the fiber surface with unprecedented sub-angstrom precision and ultralow loss [4, 29, 108].

The success of the work presented below is primarily based on the idea of bridging the SNAP platform [29] and WGM microfluidic sensing platform [26], which have much in common [38]. In fact, while SNAP considers WGMs controlled by nanoscale deformation of the *outer surface* of an optical fiber, similar control can be performed in microcapillaries by small and slowly varying *internal nonuniformities*. In the previous chapter, we showed that the introduction of SNAP resonators is possible by deformation of the external as well as the internal capillary surfaces [104].

Alternatively, here we consider liquid situated in a *uniform* microcapillary. We show that the control over the WGMs propagating along the microcapillary can be performed only by the

nonuniformities of the liquid. In particular, we demonstrate that a water droplet situated inside a silica microcapillary can fully localize WGMs and introduce a high quality-factor optical microresonator. The spectra of this resonator, measured with a microfiber translated along the capillary, presents a hierarchy of resonances that allow us to determine the size of the droplet and variation of its length due to the evaporation. The resolution of our measurements of this variation equal to 4.5 nm is only limited by the resolution of the optical spectrum analyzer used. Our discovery paves the way for the development of a novel comprehensive method for microfluidic sensing and a new type of tunable resonant microfluidic-based photonic devices. The work presented in this chapter was conducted at Aston Institute of Photonics Technologies (AIP T), Birmingham, UK. It is adapted from the following publications: [101] and [109].

5.1 Observation of an Optical Microresonator Induced by a Droplet

The microcapillary used in our experiment was prepared from a polymer-coated silica capillary fiber drawn at OFS Laboratories. Figure 5.1 shows the optical microscope image of the cross section of this capillary after the polymer coating was removed in hot sulfuric acid. From this image, the external and internal radii of the capillary were determined as $r_{int} = 61 \text{ }\mu\text{m}$ and $r_{ext} = 68 \text{ }\mu\text{m}$.

In our experiment, one end of a several-centimeters-long fiber was glued in into the needle of a syringe that was used to launch and position the water droplets inside the fiber. The other end was left open. The silica microcapillary was prepared by removing the coating from a few-centimeter section in the middle of this fiber. An optical microscope image of a sample droplet positioned inside the stripped section of the fiber is shown in Figure 5.2. It is seen that the droplet possesses the characteristic menisci introduced by the surface tension.

The idea of our experiment is illustrated in Figure 5.3. A biconical fiber taper with a micron-diameter waist (3-mm-length microfiber with diameter of $1.6 \text{ }\mu\text{m}$) was oriented normal to the capillary and connected to a LUNA optical spectrum analyzer (1.3 pm wavelength resolution).

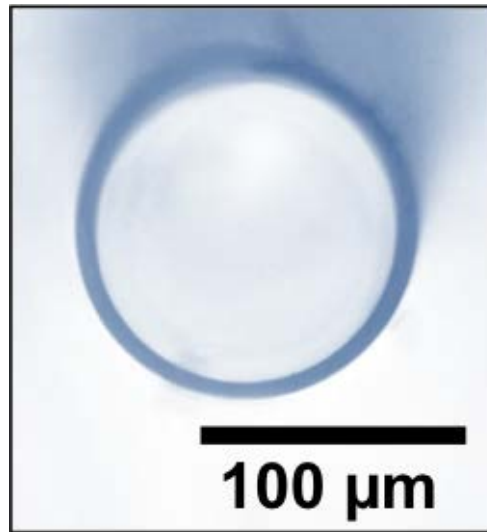


FIGURE 5.1: The optical microscope image of the cross section of the silica microcapillary used in the experiment. This image was used to determine the radius of the capillary and the thickness of its wall.

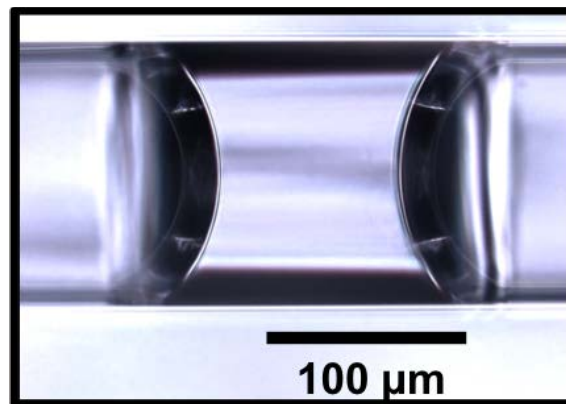


FIGURE 5.2: The optical microscope image of a water droplet inside the capillary. The droplet meniscuses caused by the surface tension are clearly seen.

The microfiber was translated along the capillary axis z and periodically placed in direct mechanical contact with the capillary to measure the transmission power $P(z, \lambda)$ as a function of the microfiber coordinate along the capillary z and wavelength λ [29].

Figure 5.4 shows the surface plot of transmission spectra $P(z, \lambda)$ collected in the bandwidth $1539.5 \text{ nm} < \lambda < 1545 \text{ nm}$ at points spaced by $2 \text{ }\mu\text{m}$ along the $600 \text{ }\mu\text{m}$ capillary section with the droplet in the middle. The spectra are found to be quasiperiodic in wavelength with a period of 3.92 nm (see Appendix C).

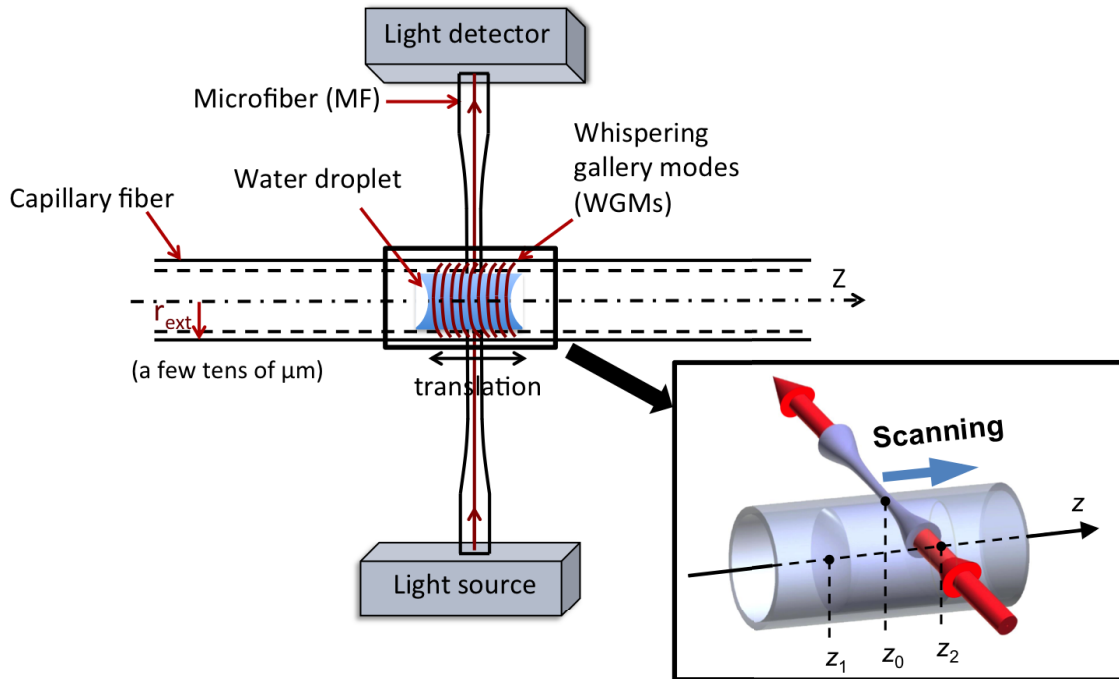


FIGURE 5.3: Illustration of the experiment. The input-output taper with a micron-diameter waist (microfiber) is positioned normally to the capillary. The microfiber excites WGMs which propagate along the microcapillary wall and sense the droplet.

The time of each measurement (including the time required for recording the spectrum and the time of translation of the microfiber between the measurement points) was $10s$. Consequently, the full time of recording of the spectra along the $600 \mu m$ capillary section was 50 min, while the measurements along the length of the droplet took around 11 min.

The spectral plot in Figure 5.4(a) clearly outlines the area where the water droplet is situated. As explained in the next section, the green pathways (dips) outside the droplet area correspond to the cutoff wavelengths of WGMs. Some of these pathways (e.g., those close to 1540.2 nm , 1540.9 nm , and 1541.8 nm) cross the droplet area unaffected. This means that the corresponding WGMs are not perturbed by the presence of the droplet. Other lines (e.g., those close to 1539.9 nm , 1540.5 nm , and 1543.3 nm) are interrupted in the droplet area, indicating that the corresponding WGMs are perturbed by the droplet. The interruption of these lines is accompanied by the appearance of additional resonances, which are explained by the full localization of the corresponding WGMs in the droplet area. The evanescent coupling of these WGMs to the water droplet causes the positive shifts of their cutoff wavelengths and the formation of a

high-quality factor microresonator. The position of resonances is in excellent agreement with the theory presented below.

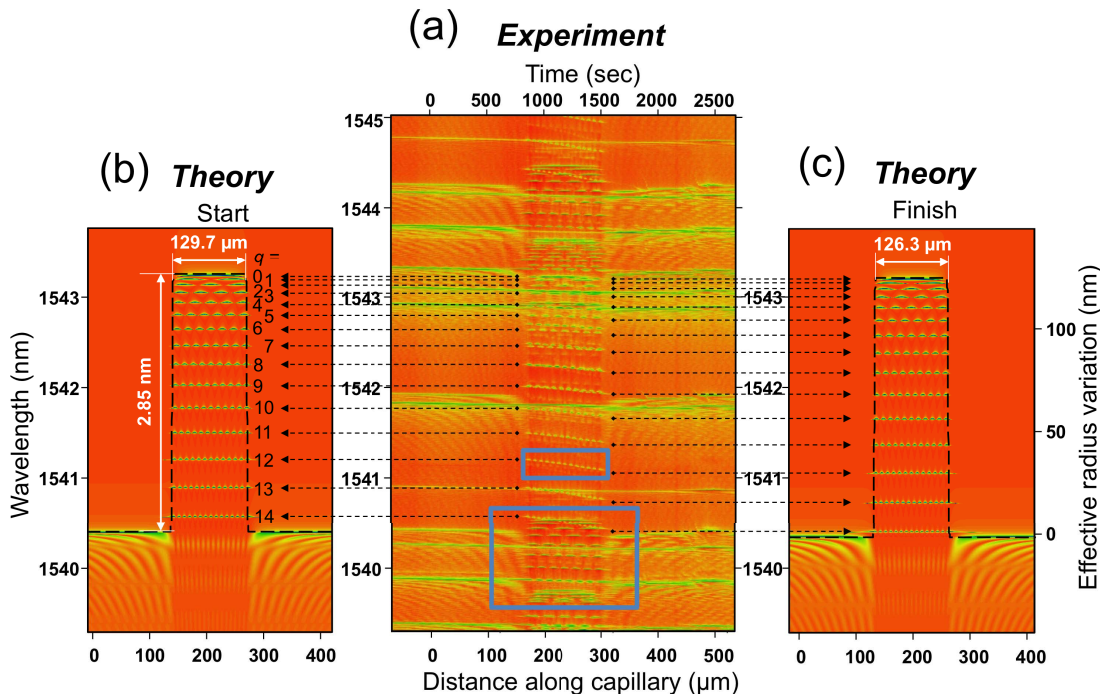


FIGURE 5.4: **a.** Surface plot of the transmission power spectra collected by the input-output microfiber translated along the microcapillary with a droplet inside. The spectral (vertical axis) and spatial (horizontal axis) resolutions of the scan were 1.3 pm and $2 \text{ }\mu\text{m}$, respectively. The central part of the plot indicates the region where the droplet was situated. **b.** and **c.** Surface plots of the calculated transmission power spectra corresponding to the stationary droplet with the initial (b) and final (c) dimensions which were obtained for a single cutoff wavelength using Eqs. 5.2-5.4. The initial and final dimensions were taken from the experimental plot (a) at axial coordinates z_1 and z_2 [Fig. 5.3] when the measurement of the droplet region started and finished.

5.2 Theory of Cutoff Wavelengths and Quantization of Slow WGMs

High-quality-factor optical resonance lines are commonly observed in the WGM spectra of optical fibers [15, 26, 27]. These resonances correspond to the so-called cutoff wavelengths of light λ_{mp} . Here m and p are the azimuthal and radial quantum numbers, which are numerate modes propagating in an axially symmetric and uniform fiber (in particular, a capillary fiber). The

expression for the electromagnetic field of these modes is factorized in cylindrical coordinates (z, ρ, φ) as [84]

$$E_{mpq}^{\pm}(z, \rho, \varphi) = \exp(\pm i\beta_{mp}(\lambda)z) \exp(im\varphi)Q_{mp}(\rho) \quad (5.1)$$

Here the slowness of WGMs is manifested in the small value of their propagation constant, $\beta_{mp}(\lambda)$, or, equivalently, in the proximity of their wavelength λ to the cutoff wavelength $\lambda_{mp}^{(cut)}(z)$. The fact that the cutoff wavelengths of the WGMs with very large azimuthal quantum numbers m correspond to the zero propagation constant, $\beta = 0$, does not contradict to the well-known relation $k_{mp}n_{ext} < \beta < k_{mp}n_{cap}$ for small m [84]. Also, the function $Q_{mp}(\rho)$ exponentially decreases outside the capillary for $\rho > r_{ext}$ and inside the capillary for $\rho < r_{int}$. The optical modes of our interest are the WGMs, which are adjacent to the optical fiber surface. At cutoff wavelengths λ_{mp} , the propagation constants of these modes approach zero, $\beta_{mp}(\lambda_{mp}) = 0$. The speed of propagation of WGMs with small $\beta_{mp}(\lambda)$ along the capillary axis is slow. It is due to the slowness of WGMs that they can be governed by angstrom-scale variations of the effective fiber radius employed in SNAP [29]. As explained below, a similar effective radius variation effect can be introduced by the shifts of cutoff wavelengths λ_{mp} caused by the evanescent coupling of WGMs to a water droplet inside a capillary fiber.

Figure 5.5(a) shows the dependencies of λ_{mp} for the silica microcapillary with the refractive index $n_{cap} = 1.46$ and external radius $r_{ext} = 68 \mu m$ as a function of internal radius r_{int} . The solid and dashed curves correspond to the empty and water-filled capillary, respectively. The external and internal radii, $r_{int} = 61 \mu m$ and $r_{ext} = 68 \mu m$, of the capillary used in our experiment are indicated by the vertical dashed lines. In calculations, we chose the azimuthal quantum number $m = 364$ so that the cutoff wavelength of the first WGM sensitive to water corresponds to the wavelength $\sim 1.54 \mu m$ close to the value of an experimental cutoff wavelength in Figure 5.4(a).

The noticeable shifts caused by the presence of water are found for the WGMs with radial quantum numbers $p \geq 2$. Specifically, for $p = 2, 3, 4$, and 5 these shifts are $0.003 nm$, $0.2 nm$, $1.1 nm$, $3.2 nm$, and $6.0 nm$, respectively. The characteristic behavior of evanescent field in the water-filled microcapillary can be found, e.g., in [26].

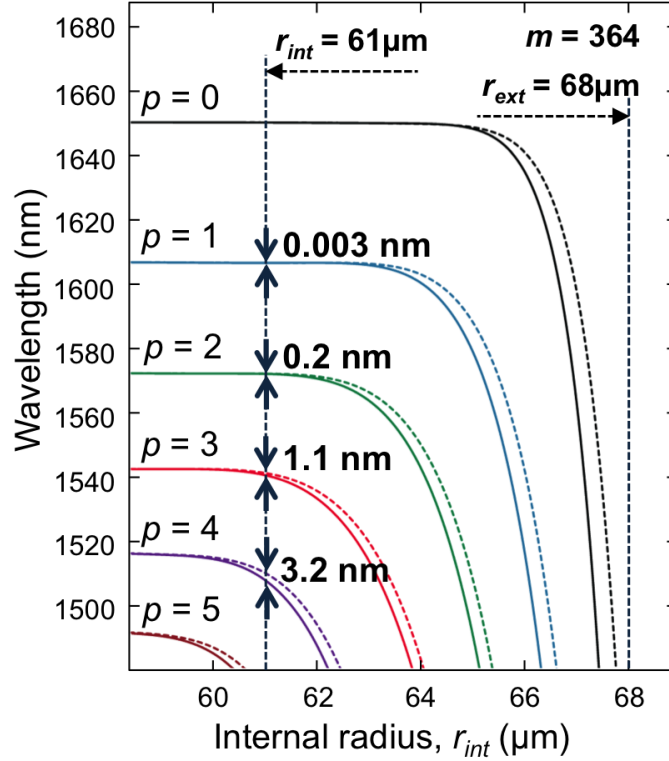


FIGURE 5.5: Cutoff wavelengths with the azimuthal quantum number $m = 364$ and radial quantum numbers $p = 0, 1, 2, 3, 4, 5$ for the silica microcapillary with external radius $r_{ext} = 68 \mu m$ as a function of the microcapillary internal radius r_{int} . The solid and dashed curves correspond to the empty and water-filled microcapillary, respectively.

Figure 5.6(b) shows the calculated cutoff wavelengths λ_{mp} for the transverse-electric (TE)-polarized WGMs with radial quantum numbers $p = 0, 1, \dots, 5$, which are situated in the bandwidth $1.54 \mu m < \lambda < 1.55 \mu m$ (see Appendix C). As we found above, the WGMs having frequencies λ_{mp} with small $p = 0$ and 1 are not affected by liquid. On the other hand, the WGMs with large $p \gg 1$, which strongly scatter from interfaces, may be undetectable due to their high attenuation. For this reason, the values λ_{mp} situated in the bandwidth $1.54 \mu m < \lambda < 1.55 \mu m$ are shown in Figure 5.6(b) for quantum numbers $p \leq 5$, which are presumably detected in our experiment. The corresponding azimuthal quantum numbers m ranging from 347 to 393 are shown in Figure 5.6(b) as well.

The cutoff wavelengths of the transverse magnetic (TM)-polarized WGMs, which are not shown

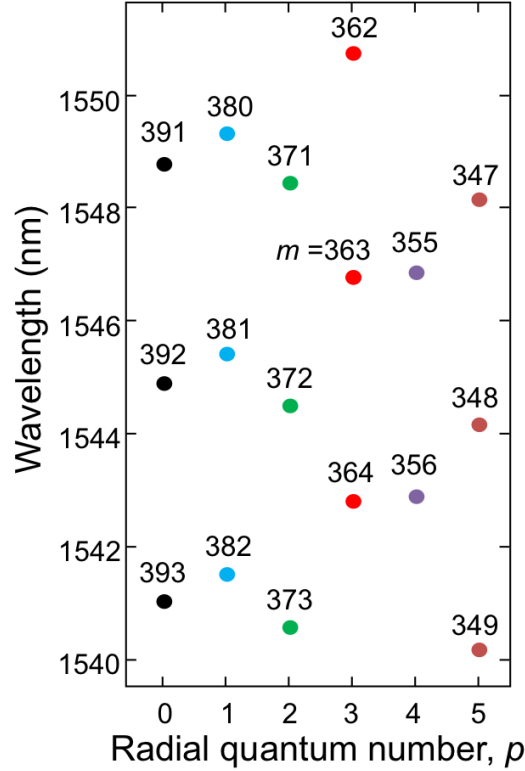


FIGURE 5.6: The distribution of cutoff wavelengths (dots) for the TE-polarized WGMs having $p = 0, 1, 2, 3, 4, 5$ in the bandwidth $1540 \text{ nm} < \lambda < 1550 \text{ nm}$. The corresponding azimuthal quantum numbers m are shown next to each of the dots.

in this figure, are known to have significantly smaller quality-factors than those of the TE-polarized WGMs due to scattering from the surface and bulk nonuniformities [66]. The distribution of the cutoff wavelengths in Figure 5.6(b) is in a reasonable quantitative agreement with that of the measured resonant wavelengths in Figure 5.4(a).

The appearance of a microresonator induced by a water droplet is explained as follows. In the vicinity of cutoff wavelengths, the propagation constant is small and can be determined in the first order of the perturbation theory as

$$\beta_{mp}^{(a),(w)}(\lambda) = 2^{3/2} \pi n_{cap} (\lambda_{mp}^{(a),(w)})^{-3/2} (\lambda_{mp}^{(a),(w)} - \lambda)^{1/2} \quad (5.2)$$

where n_{cap} is the refractive index of the capillary material and superscript indices (a) and (w) correspond to the air-filled and water-filled capillaries, respectively. This equation is identical

to Equation 2.52 in section 2.4.2.

From Equation 5.2, the propagation constant is real for wavelengths $\lambda < \lambda_{mp}^{(a),(w)}$ and pure imaginary for $\lambda > \lambda_{mp}^{(a),(w)}$. Assume that the cutoff wavelength $\lambda_{mp}^{(a)}$ of the empty capillary experiences a relatively small positive perturbation and becomes equal to $\lambda_{mp}^{(w)}$ after the capillary is filled in with water. Then, for the wavelength λ , which is close to $\lambda_{mp}^{(a)}$ and $\lambda_{mp}^{(w)}$, the expressions for propagation constants in the water-filled and empty capillary can be calculated from Equation 5.2.

In our approximation, the relatively small perturbation of the WGM dependence on the radial coordinate in $Q_{mp}(\rho)$ due to the presence of water can be neglected. Then, the behavior of WGMs along the microcapillary with a droplet inside is determined by the one-dimensional wave equation,

$$\frac{d^2 \Psi_{mp}}{dz^2} + \beta_{mp}^2(\lambda, z) \Psi_{mp} = 0 \quad (5.3)$$

where $\beta_{mp}(\lambda, z) = \beta_{mp}^{(w)}(\lambda, z)$ inside the droplet region, $z_1 < z < z_2$ [Fig. 5.3(c)], and $\beta_{mp}(\lambda, z) = \beta_{mp}^{(a)}(\lambda, z)$ outside it. Substitution of expressions for the propagation constants from Eq. 5.2 into Eq. 5.3 makes Eq. 5.3 equivalent to the Schrödinger equation for the rectangular quantum well [110].

In particular, it becomes obvious that WGMs with wavelengths $\lambda_{mp}^{(a)} < \lambda < \lambda_{mp}^{(w)}$ can be localized by the droplet. These modes are oscillatory in the droplet region (here $\beta_{mp}(\lambda, z)$ is real) and exponentially decay outside it (here $\beta_{mp}(\lambda, z)$ is pure imaginary). The quantization rule for these modes is similar to the quantization rule for the rectangular quantum well. The transmission amplitude through the microfiber placed in contact with the capillary at point z is expressed through the Green's function of Equation 5.3, $G(z, z, \lambda)$ as [71]

$$A(z, \lambda) = A_0 - \frac{i|C|^2 G(z, z, \lambda)}{1 + DG(z, z, \lambda)} \quad (5.4)$$

Here constants A_0 , $|C|$, and D are the microfiber capillary coupling parameters, which are usually determined experimentally.

As an example, Figure 5.7 shows the surface plot of the transmission power $P(z, \lambda) = |A(z, \lambda)|^2$ for our microcapillary having $r_{int} = 61 \mu m$ and $r_{ext} = 68 \mu m$ with a water droplet of $100 \mu m$ length inside. The transmission power $P(z, \lambda)$ shown in Figure 5.7 is found for the characteristic microfiber capillary coupling parameters $A_0 = 0.8 - 0.1i$, $|C|^2 = 0.02 \mu m^{-1}$, and $D = 0.02 + 0.025i \mu m^{-1}$ [71].

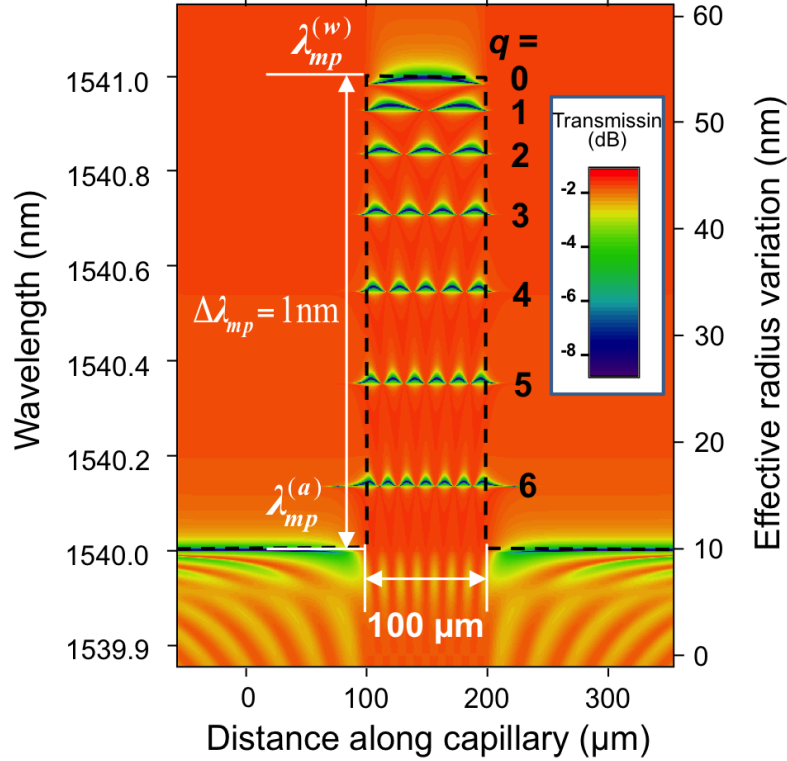


FIGURE 5.7: A sample surface plot of transmission power spectra calculated using Eqs. 5.2, 5.3, and 5.4 for the water-induced shift of the cutoff wavelength equal to 1 nm and microfiber-capillary coupling parameters indicated in the text.

The cutoff wavelength of the empty capillary is set to $\lambda_{mp}^{(a)} = 1540 \text{ nm}$, close to one of the cutoff wavelengths observed in our experiment [Fig. 5.4(a)]. Approximating the behavior of the $p = 3$ cutoff wavelength in Figure 5.5, we assume that this wavelength increases by $\Delta\lambda_{mp} = 1 \text{ nm}$ and becomes $\lambda_{mp}^{(w)} = 1.541 \mu m$ in the droplet region. The introduced cutoff wavelength profile [bold black dashed line in Figure 5.7] corresponds to a quantum well in Equation 5.3 and, equivalently, to an optical microresonator. The right-hand-side vertical axis in Figure 5.7 is the effective radius variation determined from the cutoff wavelength variation by the rescaling equation $\Delta r_{mp}/r_{ext} = \Delta\lambda_{mp}/\lambda_{mp}^{(a)}$. The horizontal resonance pathways in Figure 5.7 with interchanging

nodes and antinodes correspond to the axial eigenvalues of this microresonator with quantum numbers $q = 0, 1, \dots, 6$. In analogy to the bottle microresonators induced by the external radius variation [29], this microresonator can be called a *droplet-induced bottle microresonator*.

5.3 Interpretation of the Experimental Observations

The surface plot of the experimental spectra in Figure 5.4(a) exhibits several series of resonance pathways. Some of pathways cross the droplet region without visible perturbation. As explained above, they correspond to the cutoff wavelengths with small radial quantum numbers $p < 2$. Other pathways experience a break in the droplet region, which is accompanied by the appearance of series of resonance lines with interchanging nodes and anti-nodes. The behavior of each of these series, taken separately, is similar to that in the numerical example of a droplet-induced bottle resonator shown in Figure 5.7. To clarify this, we consider two examples.

The first example corresponds to the behavior of the cutoff wavelength which is close to 1540.44 nm outside the droplet. This wavelength experiences a positive shift of 2.85 nm in the region of the droplet. The shift introduces a microresonator containing 15 eigenvalues with axial quantum numbers $q = 0, 1, \dots, 14$ indicated on the theoretical 2D plots of transmission power in Figs. 5.4(b) and 5.4(c) described below. Based on calculations shown in Figure 5.5, we suggest that the radial quantum number of these eigenvalues is equal to $p = 4$.

As noted above, the process of characterization of the microresonator region took around 11 min. During this time the droplet became smaller in length due to evaporation. It is well known from quantum mechanics that the decrease of the length of the rectangular quantum well (resonator) leads to the growth of the separation between its eigenvalues [110]. For this reason, the pathways indicating the axial eigenvalues in Figure 5.4(a) have a small negative slope. As shown in the next section, the measurement of this slope allows us to detect the variation of the droplet size with nanometer precision.

Figures 5.4(b) and 5.4(c) show the results of our theoretical characterization of the droplet using Eqs. 5.2, 5.3, and 5.4, which fit the experimental spectra before and after measurements (see Appendix C). The theoretical as well as experimental pathways with axial quantum numbers q

indicated in Figure 5.4(b) consist of $q + 1$ anti-nodes. The agreement between the positions of wavelength resonances found theoretically and their positions found experimentally is excellent.

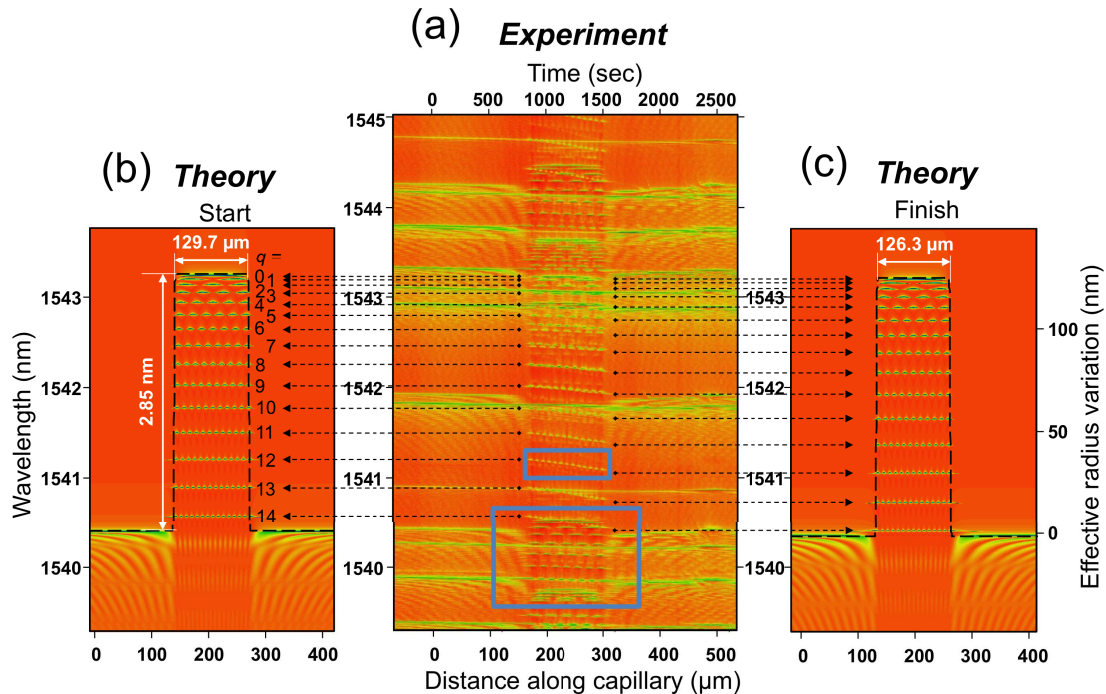


FIGURE 5.8: **a-c.** Magnified spectral region of the surface plot 5.4(a) and the theoretical models of the droplet similar to those shown in 5.4(b) and 5.4(c) but for a different cutoff wavelength.

In the second example, we consider a 2D spectral fragment magnified in Figure 5.8(a). Here the cutoff wavelength equal to 1539.88 nm outside the droplet is shifted by 0.7 to 1540.58 nm in the droplet region. Based on calculations presented in Figure 5.5, we suggest that the radial quantum number of this cutoff wavelength is $p = 3$. Our numerical modeling shown in Figs. 5.8(b) and 5.8(c) precisely confirms the length of the droplet L equal to 129.7 and $126.3 \mu\text{m}$ before and after its characterization, which has been initially calculated in the first example.

Finally, Figure 5.9 shows that the quality factor of the induced microresonator is remarkably large, $\sim 5 \times 10^5$.

Before the full stabilization of the droplet, it was translated along the originally dry capillary from right to left. As the result, tiny micro-islands of water adjacent to the internal capillary surface were left behind at the right-hand-side of the droplet. Examination of resonance pathways outside the droplet in Figure 5.4(a) allows us to distinguish between the perturbations caused

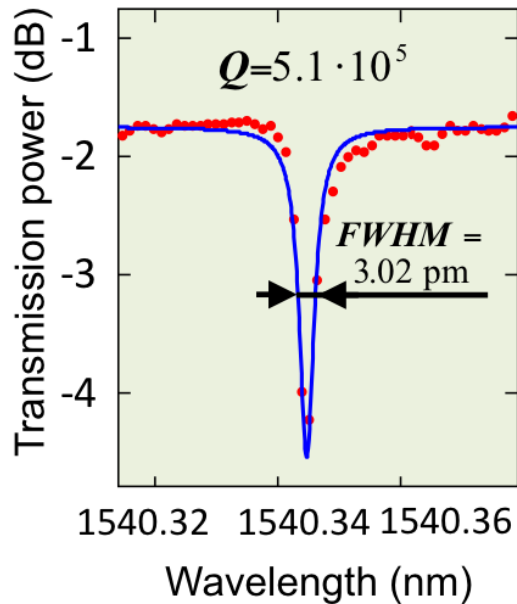


FIGURE 5.9: The resonance of the droplet-induced microresonator measured at the node indicated at the spectral plot 5.8(a).

by outside contamination, which disturbs all pathways similarly, and perturbations caused by the water islands situated inside the capillary. As discussed above, the latter disturb the pathways with relatively large radial quantum numbers p and has negligible effect on pathways with $p < 2$.

For example, the pathway close to $\lambda = 1540.9 \text{ nm}$, which crosses the droplet unperturbed and presumably has $p = 0$, is straight everywhere except the disturbance near $z = 500 \text{ }\mu\text{m}$. Since this disturbance is replicated in all other pathways, we suggest that it is caused by perturbations of the external capillary surface. However, the pathway close to $\lambda = 1540.5 \text{ nm}$ is straight at the left hand of the droplet and, unlike the pathway at $\lambda = 1540.9 \text{ nm}$, is corrugated at its right-hand side. For this reason, we suggest that these corrugations are caused by water islands inside the capillary.

5.4 Evaporation of the Droplet and Concomitant Effects

Due to the evaporation of the droplet in the process of its characterization, the successive measurements comprising the 2D plot in Figure 5.4(a) present the spectra of the microresonator continuously reducing in length. For this reason, in contrast to the purely horizontal resonance pathways in theoretical plots in Figs. 5.4(b), 5.4(c), 5.8(b), and 5.8(c), the resonance pathways in the droplet region of experimental Figure 5.4(a) are tilted. Analysis of the behavior of these tilted pathways allows us to determine the variation of the droplet length with exceptionally accurate nanometer precision.

Figure 5.10 shows the magnified fraction of the 2D plot in Figure 5.4(a), which includes the resonance pathway corresponding to axial quantum number $q = 12$ consisting of 13 anti-nodes. The most accurate measurement of the immediate wavelength eigenvalue of the microresonator is achieved at the nodes of this pathway, which correspond to the minimum coupling between the excited WGM and input-output microfiber.

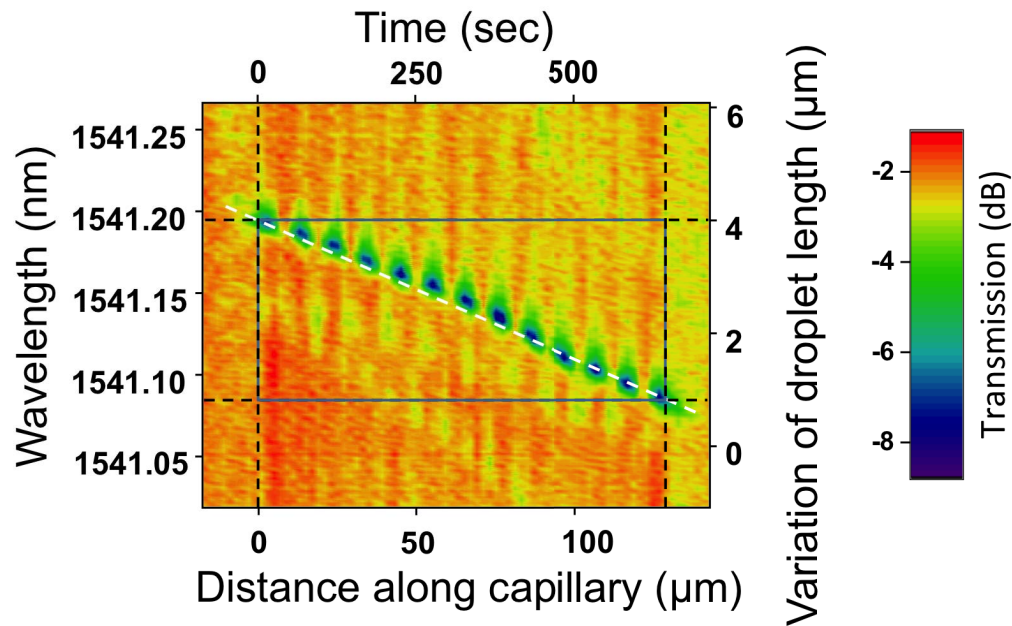


FIGURE 5.10: Magnified spectral region of the surface plot 5.8(a) containing the pathway of resonances with the axial quantum number $q = 12$ which was used for the analysis of the droplet evaporation.

For the model of the rectangular quantum well described by Eqs. 5.2 and 5.3, the change ΔL of the resonator length L can be determined from the shift $\Delta\lambda$ of the eigenvalue λ_{mpq} with large axial quantum number $q \gg 1$ by the equation

$$\Delta L = \frac{4n_{cap}^2 L^3}{q^2 \lambda_{mp}^3} \Delta\lambda \quad (5.5)$$

derived in Appendix C. From this equation and analysis of the pathway with axial quantum number $q = 12$ shown in Figure 5.10, we find that the total wavelength shift $\Delta\lambda_t = 0.11 \text{ nm}$, which the eigenvalue $\lambda_{mp,12} \approx 1.541 \text{ }\mu\text{m}$ acquires during the time of scan of the droplet region equal to 10.7 min , corresponds to the droplet reduction in length of $\Delta\lambda_t = 3.8 \text{ }\mu\text{m}$ and shrinking speed of $0.35 \text{ }\mu\text{m}/\text{min}$. Using Equation 5.5, the resolution of the measurement of the droplet length variation is found from the resolution of our optical spectrum analyzer equal to $\Delta\lambda_r = 0.13 \text{ pm}$ as $\Delta L_r = 4.5 \text{ nm}$. Due to geometric reasons, this remarkably high resolution is, nevertheless, two orders of magnitude worse than that achieved in SNAP technology for the effective variation of the optical fiber radius [4, 29, 108].

It is interesting to estimate the deformation of the capillary due to the surface tension induced by the droplet. The additional pressure P experienced by the capillary wall can be estimated by the **Young–Laplace equation**, $P = 2\gamma/R$ [111]. Assuming the characteristic value of the surface tension $\gamma \sim 0.1 \text{ N/m}$ and capillary and meniscus radii $r_{ext} \sim R \sim 100 \text{ }\mu\text{m}$, we find $P \sim 1 \text{ kPa}$. Depending on the actual values of the surface tension at the water – air, water – silica, and silica – air interfaces, which usually have the same order of magnitude [111], this pressure can be positive or negative.

Consequently, it can increase or decrease the effective radius of the capillary. The radius variation δr caused by the surface pressure can be found from the elasticity theory of thin-walled cylinders as $\delta r = Pr_{ext}^2 (E\Delta r)^{-1}$, where Δr is the capillary wall thickness and E is its Young modulus [112]. Since the effect of the stress-induced refractive index variation is usually smaller than that of the mechanical deformation, we estimate the corresponding shift of the capillary radius as $\delta r \sim 3 \text{ pm}$ and the cutoff wavelength as $\delta\lambda \sim \delta r \lambda / r_{ext} \sim \lambda_{mp} \gamma (E\Delta r)^{-1} \sim 0.1 \text{ pm}$. These values are much smaller than those observed in our experiment for WGMs with radial

quantum numbers $p > 2$. We suggest that the introduced shift can be detected by more accurate measurements of the cutoff wavelength shifts of WGMs with $p = 0$ since their evanescent coupling to the droplet is negligibly small.

Usually, a water droplet carries an electric charge e (see e.g., Refs. [113, 114]). The value of e is limited by the maximum charge-induced expanding force, which can be withheld by the surface tension. Estimating e by the Rayleigh formula for a spherical droplet, $e \leq 8\pi(\epsilon_0\gamma)^{1/2}R_0^{3/2}$, where ϵ_0 is the vacuum permittivity and $R_0 \sim 100 \mu m$ is the characteristic radius of the droplet, we find $e \leq 2 \times 10^{-11} C$.

Assuming that the distribution of charge along the droplet surface is uniform, we find that the charge induced effective radius variation of the capillary (limited by the droplet stability) has the same order of magnitude as the radius variation induced by the surface tension calculated above. However, the electrostatic calculations (see e.g., [115]) show that the distribution of charge at the droplet–capillary surface interface can be strongly nonuniform. The charge density can grow by an order of magnitude near the droplet edges where the introduced capillary radius variation can be significantly greater.

Another effect induced by the droplet charge is the DC Kerr effect [116, 117]. By modeling the droplet as a cylinder of length L and charge e , we estimate the electric field inside the capillary as $E = e/(2\pi\epsilon_0 n_{cap} L r_{ext})$. For $e \sim 10^{-11} C$, $L \sim 100 \mu m$ and $r_{ext} \sim 50 \mu m$, we have $E \sim 10^7 V/m$. The refractive index variation introduced by this field is expressed through the third-order electric susceptibility χ^3 as $\delta n_{DCKerr} = (3\chi^{(3)}/2n_{cap})E^2$ [117].

For silica, $\chi^{(3)} \sim 2 \times 10^{-22} m^2/V^2$ and the refractive index variation of the capillary introduced by the DC Kerr effect in the droplet region is estimated as $\delta n_{DCKerr} \sim 10^{-7}$. This corresponds to the cutoff wavelength shift of $\delta\lambda \sim \delta n_{DCKerr} \lambda_{mp}/n_{cap} \sim 0.1 pm$ having the same order of magnitude as the shifts introduced by the surface tension mechanically. From the above expressions for E and δn_{DCKerr} , we have $\delta n_{DCKerr} \sim L^{-2}$. Therefore, the DC Kerr effect can be increased by an order of magnitude for a droplet with three times smaller length. In addition, the DC Kerr effect, being proportional to the local charge density squared, is significantly greater near the droplet edges where, as noted above, the charge density maximizes.

5.5 Summary

We have shown, experimentally and theoretically, that a droplet positioned inside an optical microcapillary can trap the WGMs propagating along the capillary wall and localize them completely. The evanescent tails of WGMs penetrate into a thin layer of the droplet through the internal capillary surface. Consequently, the WGMs spectra characterize the medium, which is adjacent to the interface between the droplet and the capillary. In contrast to previous WGM microfluidic sensing methods [15–18], the presence of the droplet-induced microresonator allows us to monitor the droplet dynamics nonlocally with the fixed position of the input-output microfiber. For example, the resonance spacing measured at a single point z_0 in the droplet region [Fig. 5.3] allowed us to determine the immediate length of the droplet, which changed in the process of evaporation. More generally, examination of the WGM spectra measured at one or a few points along the droplet enables monitoring the behavior of the droplet away from these points. An important question remaining is whether the collected spectral data is sufficient to solve the inverse problem completely and determine the refractive index variation near the internal capillary surface.

Future research and development exploring the discovered phenomenon promises wide-ranging applications in microfluidics, surface science, and microphotonics. It is of great interest to apply the developed method to investigate the droplets of different liquids, simple and complex, including colloidal liquids [111]. As an example, the immediate positions and velocities of an individual and, presumably, a few micro/nanoparticles in a colloidal liquid can be determined from the dynamics of WGM spectrum measured at a fixed microfiber position. In contrast to the SNAP microfluidic sensor [38, 104], the microresonator enabling this nonlocal characterization of the droplet is naturally introduced and does not have to be fabricated.

It is expected that the size of particles that can be detected and monitored with our approach can achieve sub-nanoscale dimensions. In fact, it has been shown that a WGM microsphere resonator sensor enriched with plasmonic nanoparticles can detect single atoms [17]. Due to the analogy between the behavior of evanescent WGM at the periphery of a microsphere and at the interior of a capillary, we suggest that the similar resolution is feasible for plasmon enhanced WGM sensing inside a microcapillary. Remarkably, our method potentially enables the detection of the immediate axial coordinate of moving nanoparticles and molecules, which

was not possible in the previous approaches. More complex phenomena at the solid – liquid interfaces can be investigated [118–121].

Chapter 6

Conclusions and Outlook

Microfluidic sensing with optical whispering gallery modes (WGMs) circulating around the capillary is a fast developing detection method in modern microfluidics research. This method based on coupling between WGMs propagating along the wall of capillary and the interior region of the optical microcapillary. Engaging a SNAP microresonator, which is a new method to produce microscopic optical devices, at the microcapillary surface allows to remarkably advance this method. SNAP resonators are a new generation of WGM resonators consisting of an optical fiber with nanoscale variation of its effective radius. The ultra-low surface-limited loss (0.0001 dB/cm) of SNAP resonators leads to extremely good optical modes, with quality-factors (a figure of merit for optical confinement) which can reach values of ten million or higher.

In this work, we have first suggested a new low cost fabrication method to create SNAP optical microresonators on an optical fiber by pulling it using the flame brush technique. Using this well-established technique, we can create nanoscale variations in the effective radius of the fiber that localize light. We characterize the resulting resonators and find that they can host tens of axial modes with very high quality factors.

Then, we have developed a theory of SNAP platform and then experimentally present a first, to the best of our knowledge, demonstration of a sensing platform based on SNAP microresonator at a capillary fiber. The platform explores optical whispering gallery modes, which circulate inside the wall of a capillary and slowly propagate along its axis. Due to the small thickness of the capillary wall, these modes are sensitive to spatial and temporal variations of the refractive

index of the media adjacent to the internal capillary surface. In particular, the developed theory allows us to determine the internal effective radius variation of the capillary from the measured mode spectra. Experimentally, a SNAP resonator is created by local annealing of the capillary with a focused CO₂ laser followed by internal etching with hydrofluoric acid. The comparison of the spectra of this resonator in the cases when it is empty and filled with water allows us to determine the internal surface nonuniformity introduced by etching. The results obtained pave the ground way for a novel advanced approach in sensing of media adjacent to the internal capillary surface and, in particular, in microfluidic sensing.

Finally, we have shown that WGMs in a silica microcapillary can be fully localized (rather than perturbed) by evanescent coupling to a water droplet and, thus, form a high quality-factor microresonator. We have demonstrated that a droplet positioned inside an optical microcapillary can trap and completely localize the WGMs circulating along the capillary wall. The evanescent tails of WGMs penetrates into a thin surface layer of the water through the internal capillary surface. Thus, the WGMs spectra characterize the medium adjacent to the droplet-capillary interface. Since the axial modes are not confined near the point of contact with the microfiber, the spectra of the WGM measured at one point can depend on the properties of the droplet a distance away from that point. The discovered phenomenon of complete localization of light in liquid-filled optical microcapillaries suggests a new type of microfluidic photonic device as well as an ultra-precise method for microfluidic characterization. This phenomenon can also be utilized in a wide range of applications in surface science, and microphotonics. For example, the immediate positions and velocities of individual micro/nanoparticles in a colloidal liquid can be determined from the dynamics of the WGM spectrum measured at few points along the capillary. We expect that our approach can achieve molecular scale sensitivity.

Potentially, our method enables detection of the immediate axial coordinate of moving nanoparticles and local dynamic properties of microfluids which was not possible using existing approaches. More complex phenomena at the solid-liquid interfaces could also be investigated with this technique.

Bibliography

- [1] A. B. Matsko, V. S. Ilchenko, Optical resonators with whispering gallery modes i: basics, *IEEE J. Sel. Top. Quantum Electron* 12 (3) (2006) 3.
- [2] A. B. Matsko, Practical applications of microresonators in optics and photonics, CRC Press, 2009.
- [3] G. Righini, Y. Dumeige, P. Féron, M. Ferrari, G. Nunzi Conti, D. Ristic, S. Soria, Whispering gallery mode microresonators: fundamentals and applications, *Rivista del Nuovo Cimento* 34 (7) (2011) 435–488.
- [4] M. Sumetsky, Delay of light in an optical bottle resonator with nanoscale radius variation: dispersionless, broadband, and low loss, *Physical review letters* 111 (16) (2013) 163901.
- [5] W. Liang, D. Eliyahu, V. S. Ilchenko, A. A. Savchenkov, A. B. Matsko, D. Seidel, L. Maleki, High spectral purity kerr frequency comb radio frequency photonic oscillator, *Nature communications* 6 (2015) 7957.
- [6] M. Cai, O. Painter, K. Vahala, P. Sercel, Fiber-coupled microsphere laser, *Optics letters* 25 (19) (2000) 1430–1432.
- [7] M. Humar, A. Dobravec, X. Zhao, S. H. Yun, Biomaterial microlasers implantable in the cornea, skin, and blood, *Optica* 4 (9) (2017) 1080–1085.
- [8] J. M. Ward, Y. Yang, S. N. Chormaic, Glass-on-glass fabrication of bottle-shaped tunable microlasers and their applications, *Scientific reports* 6 (2016) 25152.

- [9] S. Yakunin, L. Protesescu, F. Krieg, M. I. Bodnarchuk, G. Nedelcu, M. Humer, G. De Luca, M. Fiebig, W. Heiss, M. V. Kovalenko, Low-threshold amplified spontaneous emission and lasing from colloidal nanocrystals of caesium lead halide perovskites, *Nature communications* 6 (2015) 8056.
- [10] F. Gu, F. Xie, X. Lin, S. Linghu, W. Fang, H. Zeng, L. Tong, S. Zhuang, Single whispering-gallery mode lasing in polymer bottle microresonators via spatial pump engineering, *Light: Science & Applications* 6 (10) (2017) e17061.
- [11] K. J. Vahala, Optical microcavities, *nature* 424 (6950) (2003) 839.
- [12] J. Volz, M. Scheucher, C. Junge, A. Rauschenbeutel, Nonlinear π phase shift for single fibre-guided photons interacting with a single resonator-enhanced atom, *Nature Photonics* 8 (12) (2014) 965.
- [13] H. J. Kimble, The quantum internet, *Nature* 453 (7198) (2008) 1023.
- [14] A. Reiserer, G. Rempe, Cavity-based quantum networks with single atoms and optical photons, *Reviews of Modern Physics* 87 (4) (2015) 1379.
- [15] X. Fan, I. M. White, Optofluidic microsystems for chemical and biological analysis, *Nature photonics* 5 (10) (2011) 591.
- [16] E. Kim, M. D. Baaske, F. Vollmer, Towards next-generation label-free biosensors: recent advances in whispering gallery mode sensors, *Lab on a Chip* 17 (7) (2017) 1190–1205.
- [17] M. D. Baaske, F. Vollmer, Optical observation of single atomic ions interacting with plasmonic nanorods in aqueous solution, *Nature Photonics* 10 (11) (2016) 733.
- [18] T. Reynolds, N. Riesen, A. Meldrum, X. Fan, J. M. Hall, T. M. Monro, A. François, Fluorescent and lasing whispering gallery mode microresonators for sensing applications, *Laser & Photonics Reviews* 11 (2) (2017) 1600265.
- [19] M. Aspelmeyer, T. J. Kippenberg, F. Marquardt, Cavity optomechanics, *Reviews of Modern Physics* 86 (4) (2014) 1391.
- [20] R. Dahan, L. L. Martin, T. Carmon, Droplet optomechanics, *Optica* 3 (2) (2016) 175–178.
- [21] M. Sumetsky, Lasing microbottles, *Light: Science & Applications* 6 (10) (2017) e17102.

- [22] B. Peng, Ş. Özdemir, S. Rotter, H. Yilmaz, M. Liertzer, F. Monifi, C. Bender, F. Nori, L. Yang, Loss-induced suppression and revival of lasing, *Science* 346 (6207) (2014) 328–332.
- [23] A. V. Dmitriev, M. Sumetsky, Tunable photonic elements at the surface of an optical fiber with piezoelectric core, *Optics letters* 41 (10) (2016) 2165–2168.
- [24] G. Bahl, K. H. Kim, W. Lee, J. Liu, X. Fan, T. Carmon, Brillouin cavity optomechanics with microfluidic devices, *Nature communications* 4 (2013) 1994.
- [25] K. H. Kim, G. Bahl, W. Lee, J. Liu, M. Tomes, X. Fan, T. Carmon, Cavity optomechanics on a microfluidic resonator with water and viscous liquids, *Light: Science & Applications* 2 (11) (2013) e110.
- [26] I. M. White, H. Oveys, X. Fan, Liquid-core optical ring-resonator sensors, *Optics letters* 31 (9) (2006) 1319–1321.
- [27] V. Zamora, A. Díez, M. V. Andrés, B. Gimeno, Refractometric sensor based on whispering-gallery modes of thin capillaries, *Optics Express* 15 (19) (2007) 12011–12016.
- [28] M. Sumetsky, J. Fini, Surface nanoscale axial photonics, *Optics express* 19 (27) (2011) 26470–26485.
- [29] M. Sumetsky, Nanophotonics of optical fibers, *Nanophotonics* 2 (5-6) (2013) 393–406.
- [30] M. Sumetsky, D. DiGiovanni, Y. Dulashko, J. Fini, X. Liu, E. Monberg, T. Taunay, Surface nanoscale axial photonics: robust fabrication of high-quality-factor microresonators, *Optics letters* 36 (24) (2011) 4824–4826.
- [31] M. Sumetsky, Localization of light in an optical fiber with nanoscale radius variation, in: *Lasers and Electro-Optics Europe (CLEO EUROPE/EQEC), 2011 Conference on and 12th European Quantum Electronics Conference*, IEEE, 2011, pp. 1–1.
- [32] M. Sumetsky, D. DiGiovanni, Y. Dulashko, X. Liu, E. Monberg, T. Taunay, Photo-induced snap: fabrication, trimming, and tuning of microresonator chains, *Optics express* 20 (10) (2012) 10684–10691.

- [33] D. L. Vitullo, S. Zaki, G. Gardosi, B. J. Mangan, R. S. Windeler, M. Brodsky, M. Sumetsky, Tunable snap microresonators via internal ohmic heating, *Optics letters* 43 (17) (2018) 4316–4319.
- [34] Q. Yu, Y. Du, Z. Xu, P. Wang, Z. Zhang, Z. Zhu, H. Cao, M. Sumetsky, X. Shu, Efficient postprocessing technique for fabricating surface nanoscale axial photonics microresonators with subangstrom precision by femtosecond laser, *Optics letters* 43 (23) (2018) 5729–5732.
- [35] K. Srinivasan, P. E. Barclay, M. Borselli, O. Painter, Optical-fiber-based measurement of an ultrasmall volume high-q photonic crystal microcavity, *Physical Review B* 70 (8) (2004) 081306.
- [36] V. Lefèvre-Seguin, Whispering-gallery mode lasers with doped silica microspheres, *Optical Materials* 11 (2-3) (1999) 153–165.
- [37] H. Ghali, P. Bianucci, Y.-A. Peter, Wavelength shift in a whispering gallery microdisk due to bacterial sensing: A theoretical approach, *Sensing and Bio-Sensing Research* 13 (2017) 9–16.
- [38] M. Sumetsky, Slow light optofluidics: a proposal, *Optics letters* 39 (19) (2014) 5578–5581.
- [39] M. Sumetsky, Microscopic optical buffering in a harmonic potential, *Scientific reports* 5 (2015) 18569.
- [40] V. Dvoyrin, M. Sumetsky, Bottle microresonator broadband and low-repetition-rate frequency comb generator, *Optics letters* 41 (23) (2016) 5547–5550.
- [41] M. Sumetsky, Optical bottle versus acoustic bottle and antibottle resonators, *Optics letters* 42 (5) (2017) 923–926.
- [42] M. Segev, Y. Silberberg, D. N. Christodoulides, Anderson localization of light, *Nature Photonics* 7 (3) (2013) 197.
- [43] C. A. de Carvalho, H. M. Nussenzveig, Time delay, *Physics Reports* 364 (2) (2002) 83–174.
- [44] M. Sumetsky, Snap: subangstrom precise and ultralow loss nanophotonic platform, in: *CLEO: Science and Innovations*, Optical Society of America, 2018, pp. SF2K–1.

- [45] M. Sumetsky, Miniature slow light delay lines and buffers: A review, in: Workshop on Specialty Optical Fibers and their Applications, Optical Society of America, 2015, pp. WW2A-4.
- [46] E. F. Burmeister, D. J. Blumenthal, J. E. Bowers, A comparison of optical buffering technologies, *Optical Switching and Networking* 5 (1) (2008) 10–18.
- [47] M.-Y. Ye, M.-X. Shen, X.-M. Lin, Ringing phenomenon based whispering-gallery-mode sensing, *Scientific reports* 6 (2016) 19597.
- [48] M. Sumetsky, Y. Dulashko, R. Windeler, Optical microbubble resonator, *Optics letters* 35 (7) (2010) 898–900.
- [49] Y. Yang, J. Ward, S. N. Chormaic, Quasi-droplet microbubbles for high resolution sensing applications, *Optics express* 22 (6) (2014) 6881–6898.
- [50] S. I. Shopova, Y. Sun, A. Rosenberger, X. Fan, Highly sensitive tuning of coupled optical ring resonators by microfluidics, *Microfluidics and nanofluidics* 6 (3) (2009) 425.
- [51] J. D. Suter, I. M. White, H. Zhu, X. Fan, Thermal characterization of liquid core optical ring resonator sensors, *Applied optics* 46 (3) (2007) 389–396.
- [52] R. W. Boyd, J. E. Heebner, Sensitive disk resonator photonic biosensor, *Applied Optics* 40 (31) (2001) 5742–5747.
- [53] J. M. Ward, N. Dhasmana, S. N. Chormaic, Hollow core, whispering gallery resonator sensors, *The European Physical Journal Special Topics* 223 (10) (2014) 1917–1935.
- [54] S.-H. Hsu, Y.-C. Yang, Y.-H. Su, S.-M. Wang, S.-A. Huang, C.-Y. Lin, Biosensing using microring resonator interferograms, *Sensors* 14 (1) (2014) 1184–1194.
- [55] H. Zhu, I. M. White, J. D. Suter, M. Zourob, X. Fan, Opto-fluidic micro-ring resonator for sensitive label-free viral detection, *Analyst* 133 (3) (2008) 356–360.
- [56] R. K. Chang, A. J. Campillo, *Optical processes in microcavities*, Vol. 3, World scientific, 1996.
- [57] Y. Sun, X. Fan, Optical ring resonators for biochemical and chemical sensing, *Analytical and bioanalytical chemistry* 399 (1) (2011) 205–211.

- [58] Z. Yu, S. Fan, Extraordinarily high spectral sensitivity in refractive index sensors using multiple optical modes, *Optics express* 19 (11) (2011) 10029–10040.
- [59] E. J. Smith, S. Schulze, S. Kiravittaya, Y. Mei, S. Sanchez, O. G. Schmidt, Lab-in-a-tube: detection of individual mouse cells for analysis in flexible split-wall microtube resonator sensors, *Nano letters* 11 (10) (2010) 4037–4042.
- [60] L. Rayleigh, Cxii. the problem of the whispering gallery, *The London, Edinburgh, and Dublin Philosophical Magazine and Journal of Science* 20 (120) (1910) 1001–1004.
- [61] Y. Wu, F. Vollmer, Whispering gallery mode biomolecular sensors, in: *Cavity-Enhanced Spectroscopy and Sensing*, Springer, 2014, pp. 323–349.
- [62] P. Bianucci, X. Wang, J. Veinot, A. Meldrum, Silicon nanocrystals on bottle resonators: Mode structure, loss mechanisms and emission dynamics, *Optics Express* 18 (8) (2010) 8466–8481.
- [63] A. M. Armani, Single molecule detection using optical microcavities, in: *Photonic Microresonator Research and Applications*, Springer, 2010, pp. 253–273.
- [64] P. Bianucci, Optical resonators and quantum dots: and excursion into quantum optics, quantum information and photonics, Ph.D. thesis (2007).
- [65] M. L. Gorodetsky, A. A. Savchenkov, V. S. Ilchenko, Ultimate q of optical microsphere resonators, *Optics letters* 21 (7) (1996) 453–455.
- [66] M. L. Gorodetsky, A. D. Pryamikov, V. S. Ilchenko, Rayleigh scattering in high-q microspheres, *JOSA B* 17 (6) (2000) 1051–1057.
- [67] G. P. Agrawal, *Fiber-optic communication systems*, Vol. 222, John Wiley & Sons, 2012.
- [68] G. M. Hale, M. R. Querry, Optical constants of water in the 200-nm to 200- μ m wavelength region, *Applied optics* 12 (3) (1973) 555–563.
- [69] C. Patel, A. Tam, Optical absorption coefficients of water, *Nature* 280 (5720) (1979) 302.
- [70] T. Hamidfar, [Fabrication and characterization of surface nanoscale axial photonics microresonators](#), Master’s thesis, Concordia University (April 2015).
URL <https://spectrum.library.concordia.ca/979887/>

- [71] M. Sumetsky, Theory of snap devices: basic equations and comparison with the experiment, *Optics express* 20 (20) (2012) 22537–22554.
- [72] M. Sumetsky, K. Abedin, D. DiGiovanni, Y. Dulashko, J. Fini, E. Monberg, Coupled high q-factor surface nanoscale axial photonics (snap) microresonators, *Optics letters* 37 (6) (2012) 990–992.
- [73] M. Rabeh, A. S. Samra, M. Abouheaf, Evanescent wave coupling between optical fiber and planar optical waveguide, in: *Proceedings of the Twenty Third National Radio Science Conference (NRSC'2006)*, IEEE, 2006, pp. 1–6.
- [74] Y.-L. Pan, R. K. Chang, Highly efficient prism coupling to whispering gallery modes of a square μ cavity, *Applied physics letters* 82 (4) (2003) 487–489.
- [75] M. Cai, O. Painter, K. J. Vahala, Observation of critical coupling in a fiber taper to a silica-microsphere whispering-gallery mode system, *Physical review letters* 85 (1) (2000) 74.
- [76] T. Kippenberg, S. Spillane, D. Armani, K. Vahala, Ultralow-threshold microcavity raman laser on a microelectronic chip, *Optics letters* 29 (11) (2004) 1224–1226.
- [77] S. Hagness, D. Rafizadeh, S. Ho, A. Taflove, FDTD microcavity simulations: design and experimental realization of waveguide-coupled single-mode ring and whispering-gallery-mode disk resonators, *Journal of lightwave technology* 15 (11) (1997) 2154–2165.
- [78] A. Melloni, F. Morichetti, M. Martinelli, Linear and nonlinear pulse propagation in coupled resonator slow-wave optical structures, *Optical and Quantum Electronics* 35 (4-5) (2003) 365–379.
- [79] L. Tong, M. Sumetsky, Micro/nanofiber optical sensors, in: *Subwavelength and Nanometer Diameter Optical Fibers*, Springer, 2010, pp. 187–214.
- [80] J. Heebner, R. Grover, T. Ibrahim, T. A. Ibrahim, *Optical microresonators: theory, fabrication, and applications*, Vol. 138, Springer Science & Business Media, 2008.
- [81] J. Bures, *Guided optics*, John Wiley & Sons, 2009.

- [82] L. Tong, J. Lou, E. Mazur, Single-mode guiding properties of subwavelength-diameter silica and silicon wire waveguides, *Optics Express* 12 (6) (2004) 1025–1035.
- [83] M. Abramowitz, I. A. Stegun, *Handbook of mathematical functions: with formulas, graphs, and mathematical tables*, Vol. 55, Courier Corporation, 1965.
- [84] A. W. Snyder, J. Love, *Optical waveguide theory*, Springer Science & Business Media, 2012.
- [85] L. D. Landau, E. M. Lifshitz, *Course of theoretical physics. volume 3: Quantum mechanics* (1965).
- [86] D. J. Griffiths, D. F. Schroeter, *Introduction to quantum mechanics*, Cambridge University Press, 2018.
- [87] M. Sumetsky, Whispering-gallery-bottle microcavities: the three-dimensional etalon, *Optics letters* 29 (1) (2004) 8–10.
- [88] M. Sumetsky, Localization of light in optical fibers: Cylinder, conical and bottle microresonators, in: *Transparent Optical Networks (ICTON), 2011 13th International Conference on*, IEEE, 2011, pp. 1–4.
- [89] M. Sumetsky, Mode localization and the q-factor of a cylindrical microresonator, *Optics letters* 35 (14) (2010) 2385–2387.
- [90] M. Sumetsky, Localization of light on a cone: theoretical evidence and experimental demonstration for an optical fiber, *Optics letters* 36 (2) (2011) 145–147.
- [91] M. Sumetsky, D. J. DiGiovanni, Y. Dulashko, J. M. Fini, X. Liu, E. M. Monberg, T. F. Taunay, Robust surface nanoscale axial photonics, in: *IEEE Photonic Society 24th Annual Meeting*, 2011, pp. 1–2. [doi:10.1109/PHO.2011.6110872](https://doi.org/10.1109/PHO.2011.6110872).
- [92] M. Sumetsky, Y. Dulashko, Snap: Fabrication of long coupled microresonator chains with sub-angstrom precision, *Optics express* 20 (25) (2012) 27896–27901.
- [93] S. Bhadra, A. Ghatak, *Guided Wave Optics and Photonic Devices*, CRC Press, 2016.

- [94] Q. Yu, F. Shen, Z. Xu, H. Cao, M. Sumetsky, X. Shu, Tuning effective fiber radius variation of snap structures with a femtosecond laser, in: CLEO: QELS Fundamental Science, Optical Society of America, 2018, pp. JW2A-1.
- [95] R. R. Gattass, E. Mazur, Femtosecond laser micromachining in transparent materials, *Nature photonics* 2 (4) (2008) 219.
- [96] M. Sumetsky, Y. Dulashko, Radius variation of optical fibers with angstrom accuracy, *Optics letters* 35 (23) (2010) 4006-4008.
- [97] T. A. Birks, Y. W. Li, The shape of fiber tapers, *Journal of Lightwave Technology* 10 (4) (1992) 432-438.
- [98] D. L. Vitullo, G. Gardosi, S. Zaki, K. V. Tokmakov, M. Brodsky, M. Sumetsky, Discovery of parabolic microresonators produced via fiber tapering, *Optics letters* 43 (20) (2018) 4977-4980.
- [99] J. Ward, A. Maimaiti, V. H. Le, S. N. Chormaic, Contributed review: Optical micro-and nanofiber pulling rig, *Review of Scientific Instruments* 85 (11) (2014) 111501.
- [100] J. Buck, H. Kimble, Optimal sizes of dielectric microspheres for cavity qed with strong coupling, *Physical Review A* 67 (3) (2003) 033806.
- [101] T. Hamidfar, K. V. Tokmakov, B. J. Mangan, R. S. Windeler, A. V. Dmitriev, D. L. Vitullo, P. Bianucci, M. Sumetsky, Localization of light in an optical microcapillary induced by a droplet, *Optica* 5 (4) (2018) 382-388.
- [102] M. R. Foreman, J. D. Swaim, F. Vollmer, Whispering gallery mode sensors, *Advances in optics and photonics* 7 (2) (2015) 168-240.
- [103] P. Bianucci, Optical microbottle resonators for sensing, *Sensors* 16 (11) (2016) 1841.
- [104] T. Hamidfar, A. Dmitriev, B. Magdan, P. Bianucci, M. Sumetsky, Surface nanoscale axial photonics at a capillary fiber, *Optics letters* 42 (16) (2017) 3060-3063.
- [105] T. Hamidfar, A. Dmitriev, B. Magdan, P. Bianucci, M. Sumetsky, Surface nanoscale axial photonics (snap) at the silica microcapillary with ultrathin wall, in: *Photonics Conference (IPC)*, 2017 IEEE, IEEE, 2017, pp. 271-272.

- [106] R. Brückner, Properties and structure of vitreous silica. i, *Journal of non-crystalline solids* 5 (2) (1970) 123–175.
- [107] Y. Li, F. Abolmaali, K. W. Allen, N. I. Limberopoulos, A. Urbas, Y. Rakovich, A. V. Maslov, V. N. Astratov, Whispering gallery mode hybridization in photonic molecules, *Laser & Photonics Reviews* 11 (2) (2017) 1600278.
- [108] N. Toropov, M. Sumetsky, Permanent matching of coupled optical bottle resonators with better than 0.16 ghz precision, *Optics letters* 41 (10) (2016) 2278–2281.
- [109] T. Hamidfar, K. V. Tokmakov, B. J. Mangan, R. S. Windeler, A. V. Dmitriev, D. L. Vitullo, P. Bianucci, M. Sumetsky, Droplet-induced optical resonator in a silica microcapillary, in: *CLEO: Science and Innovations*, Optical Society of America, 2018, pp. SW4A–5.
- [110] S. Flügge, *Practical quantum mechanics*, Springer Science & Business Media, 2012.
- [111] J. C. Berg, *An introduction to interfaces & colloids: the bridge to nanoscience*, World Scientific, 2010.
- [112] S. Timoshenko, S. Timoshenko, J. Goodier, *Theory of Elasticity*, by S. Timoshenko and JN Goodier,...., McGraw-Hill book Company, 1951.
- [113] L. P. Santos, T. R. Ducati, L. B. Balestrin, F. Galembeck, Water with excess electric charge, *The Journal of Physical Chemistry C* 115 (22) (2011) 11226–11232.
- [114] S. H. Behrens, D. G. Grier, The charge of glass and silica surfaces, *The Journal of Chemical Physics* 115 (14) (2001) 6716–6721.
- [115] R. W. Scharstein, Capacitance of a tube, *Journal of Electrostatics* 65 (1) (2007) 21–29.
- [116] N. Mukherjee, R. Myers, S. Brueck, Dynamics of second-harmonic generation in fused silica, *JOSA B* 11 (4) (1994) 665–669.
- [117] A. C. Liu, M. J. Digonnet, G. S. Kino, Dc kerr coefficient of silica: theory and experiment, in: *Doped Fiber Devices II*, Vol. 3542, International Society for Optics and Photonics, 1998, pp. 102–108.

- [118] J. D. Tice, H. Song, A. D. Lyon, R. F. Ismagilov, Formation of droplets and mixing in multiphase microfluidics at low values of the Reynolds and the capillary numbers, *Langmuir* 19 (22) (2003) 9127–9133.
- [119] D. Lis, E. H. Backus, J. Hunger, S. H. Parekh, M. Bonn, Liquid flow along a solid surface reversibly alters interfacial chemistry, *Science* 344 (6188) (2014) 1138–1142.
- [120] C. Hao, J. Li, Y. Liu, X. Zhou, Y. Liu, R. Liu, L. Che, W. Zhou, D. Sun, L. Li, et al., Superhydrophobic-like tunable droplet bouncing on slippery liquid interfaces, *Nature communications* 6 (2015) 7986.
- [121] O. Björneholm, M. H. Hansen, A. Hodgson, L.-M. Liu, D. T. Limmer, A. Michaelides, P. Pedevilla, J. Rossmeisl, H. Shen, G. Tocci, et al., Water at interfaces, *Chemical reviews* 116 (13) (2016) 7698–7726.
- [122] Y. A. Demchenko, M. L. Gorodetsky, Analytical estimates of eigenfrequencies, dispersion, and field distribution in whispering gallery resonators, *JOSA B* 30 (11) (2013) 3056–3063.

Appendix A

Data Collecting

As we explained in chapter 3, to increase the efficiency of the process of saving data, we use the following AutoHotkey script. This script uses the program of oscilloscope *OpenChoice Desktop* and stage *Micronix Motion Controller (WPF-MA10.exe)*.

```
Sleep 1000
n=0
loop {
tbegin:=A-TickCount
b:=++n
if b>100
{
    Send x
}

WinActivate,OpenChoice Desktop
Sleep 9000

Click 128,365    ;Get Data
Sleep 7000
Click 132,546    ;Save As
```

```
Sleep 3000

if b<10
{
    Send a000%b% {Enter}
}
if (b>9 and b<100)
{
    Send a00%b% {Enter}
}
if (b>99 and b<1000)
{
    Send a0%b% {Enter}
}
if b>999
{
    Send a%b% {Enter}
}
Sleep 30000

Click 519,388 ;Cancel
Sleep 1000

; WinActivate,WPF_MA10.exe - Shortcut
Click 1000,781
Sleep 500
Click 400,378

Sleep 2000
Click 448,177 ;<-
Sleep 1000
```

```
Click 647,523    ;Change axis
Sleep 2000
Click 647,547    ;Axis 1
Sleep 1000
Click 647,523    ;Change axis
Sleep 2000
Click 627,550    ;Axis 1
Sleep 1000
Click 647,523    ;Change axis
Sleep 1000
Click 647,547    ;Axis 1
Sleep 2000
Click 286,177    ;-
Sleep 500
Click 286,177    ;-
Sleep 500
Click 286,177    ;-
Sleep 500
Click 479,177    ;->
Sleep 1000
Click 647,523    ;Change axis
Sleep 1000
Click 647,584    ;Axis 3
Sleep 1000
Click 647,523    ;Change axis
Sleep 2000
Click 620,587    ;Axis 3
Sleep 1000
Click 647,523    ;Change axis
Sleep 2000
Click 647,584    ;Axis 3
```

```
Sleep 1000
Click 381,177    ;+
Sleep 500
Click 381,177    ;+
Sleep 500
Click 381,177    ;+
Sleep 500
;Click 381,177    ;+
;Sleep 1000
Click 479,177    ;->
Sleep 2000
```

```
Sleep 1000
tend:=A_TickCount
Sleep 5-tend+tbegin
}
return
```

```
x::ExitApp
```


Appendix B

Data Processing

In order to make a matrix from all our data and plot a spectra in chapter 3, during the processing of our data we used the following python scripts [B.1](#) and [B.2](#). In this appendix, we report details of these scripts by order of usage. In chapters 4 and 5, we use the Mathematica script in [B.3](#).

B.1 extract-intensity-to-matrix.py

```
import sys
import numpy
from scipy.signal import decimate

if len(sys.argv) !=3:
    print ("Usage:\n\t\tMDO-to-scope.py <infile> <outfile>\n");
    sys.exit(1)
infile = sys.argv[1]
outfile = sys.argv[2]

try:
```

```
        Tr = numpy.loadtxt (infile, usecols=(0,), unpack=True)
except:
    print ("Error in numpy.loadtxt")

try:
    m = Tr

except:
    print ("Error in reading the time")

for n in range (2, 101):

    try:
        print ("Trying file a%04d-cut.dat" % n)
        Transmission = numpy.loadtxt ("a%04d-cut.dat" % n, usecols=(0,), unpack=True)
        y = Transmission
    except:
        print ("Error in reading the transmission")

    try:
        m = numpy.c_[m, y]

    except:
        print ("Error at a%04d-cut.dat" % n)

else:
    #    print m.shape
    numpy.savetxt (outfile, m, delimiter='\t')
    print ("Well done")
```

B.2 concatenate-two-matrix.py

```
#!/usr/bin/python

import sys
import numpy

# Process command line arguments.
if len(sys.argv) != 4:
    print ("Usage:\n\t\tMDO-to-scope.py <infile1> <infile2> <outfile>\n");
    sys.exit(1)
infile1 = sys.argv[1]
infile2 = sys.argv[2]
outfile = sys.argv[3]

try:
    matrix1 = numpy.loadtxt(infile1, unpack=True)
except:
    print("Error in reading matrix1")
try:
    matrix2 = numpy.loadtxt(infile2, unpack=True)
except:
    print("Error in reading matrix1")

try:
    matrix12 = numpy.concatenate((matrix1.T, matrix2.T), axis=1)
except:
    print("Error in concatenate")

try:
```

```

numpy.savetxt (outfile, matrix12, delimiter='\t')
except:
    print("Error in saving")

```

B.3 Mathematica script

```

SetDirectory[NotebookDirectory[]];
cutoffNumber = 0;

n = 140;
imp = Array[0, n];
For[i = 1, i <= n, i++,
  imp1 = Import["a" <> IntegerString[(i), 10, 4] <> ".txt", "Table"];
  If[i == 1,
    step = imp1[[4, 7]];(*in pm*)
    wavelenghts = Flatten[Drop[imp1, 8, -2]];
    wavelenghts = Drop[wavelenghts, cutoffNumber];
    wavelenghts = Drop[wavelenghts, -cutoffNumber];
  ];
  imp1 = Drop[imp1, 8, 2];(*Drops first 8 rows and 2 columns*)
  imp1 = Drop[imp1, cutoffNumber];
  imp1 = Drop[imp1, -cutoffNumber];
  imp1 = Flatten[imp1];
  imp[[i]] = Normal[imp1]
];

ColorData["Gradients"]

{"AlpineColors", "Aquamarine", "ArmyColors", "AtlanticColors", \

```

```

"AuroraColors", "AvocadoColors", "BeachColors", "BlueGreenYellow", \
"BrassTones", "BrightBands", "BrownCyanTones", "CandyColors", \
"CherryTones", "CMYKColors", "CoffeeTones", "DarkBands", \
"DarkRainbow", "DarkTerrain", "DeepSeaColors", "FallColors", \
"FruitPunchColors", "FuchsiaTones", "GrayTones", "GrayYellowTones", \
"GreenBrownTerrain", "GreenPinkTones", "IslandColors", "LakeColors", \
"LightTemperatureMap", "LightTerrain", "MintColors", "NeonColors", \
"Pastel", "PearlColors", "PigeonTones", "PlumColors", "Rainbow", \
"RedBlueTones", "RedGreenSplit", "RoseColors", "RustTones", \
"SandyTerrain", "SiennaTones", "SolarColors", "SouthwestColors", \
"StarryNightColors", "SunsetColors", "TemperatureMap", \
"ThermometerColors", "ValentineTones", "WatermelonColors"}

```

```
interpolOrder = 0;
```

```

ListDensityPlot[Transpose[imp[[All, All]]],
  AspectRatio -> 1/GoldenRatio, InterpolationOrder -> None,
  ColorFunction -> "SunsetColors",
  PlotRange -> {Full, {1570, 1575}, All}, ImageSize -> Scaled[.8],
  DataRange -> {{0, 0.7}, {wavelengths[[1]], wavelengths[[-1]]}},
  PlotLegends -> Automatic]

```

Appendix C

Supporting Content

This appendix provides supplementary information to chapter 5.

C.1 Expanded Experimental Data and Processing Details

The 2D plot of the transmission power $P(z, \lambda)$ shown in Figure 5.4(a) of the main text is a fragment of the 2D plot measured in an expanded 10 nm bandwidth shown in Figure C.1. The spectral quasiperiod equal to 3.92 nm was measured from Figure C.1. The black rectangle in this figure, which contains a single period, outlines the region shown in Figure 5.4(a).

Figure C.2 illustrates the method we used to analyze the experimental data and, in particular, to determine the initial and finite droplet widths, the shift of the cutoff wavelength due to the presence of water, and the speed of the droplet evaporation. The left hand side (theory) and right hand side (experiment) plots in this figure are fragments taken from the theoretical and experimental plots of Figure 5.4.

With a good accuracy, the axial coordinates z_1 and z_2 of the contact circumferences between the droplet menisci and the capillary (Fig. 5.3) correspond to the actual edges of the droplet-induced resonator. In fact, since the contact angle between the menisci and capillary is finite, the characteristic transition length between the cutoff wavelength of the empty and water filled

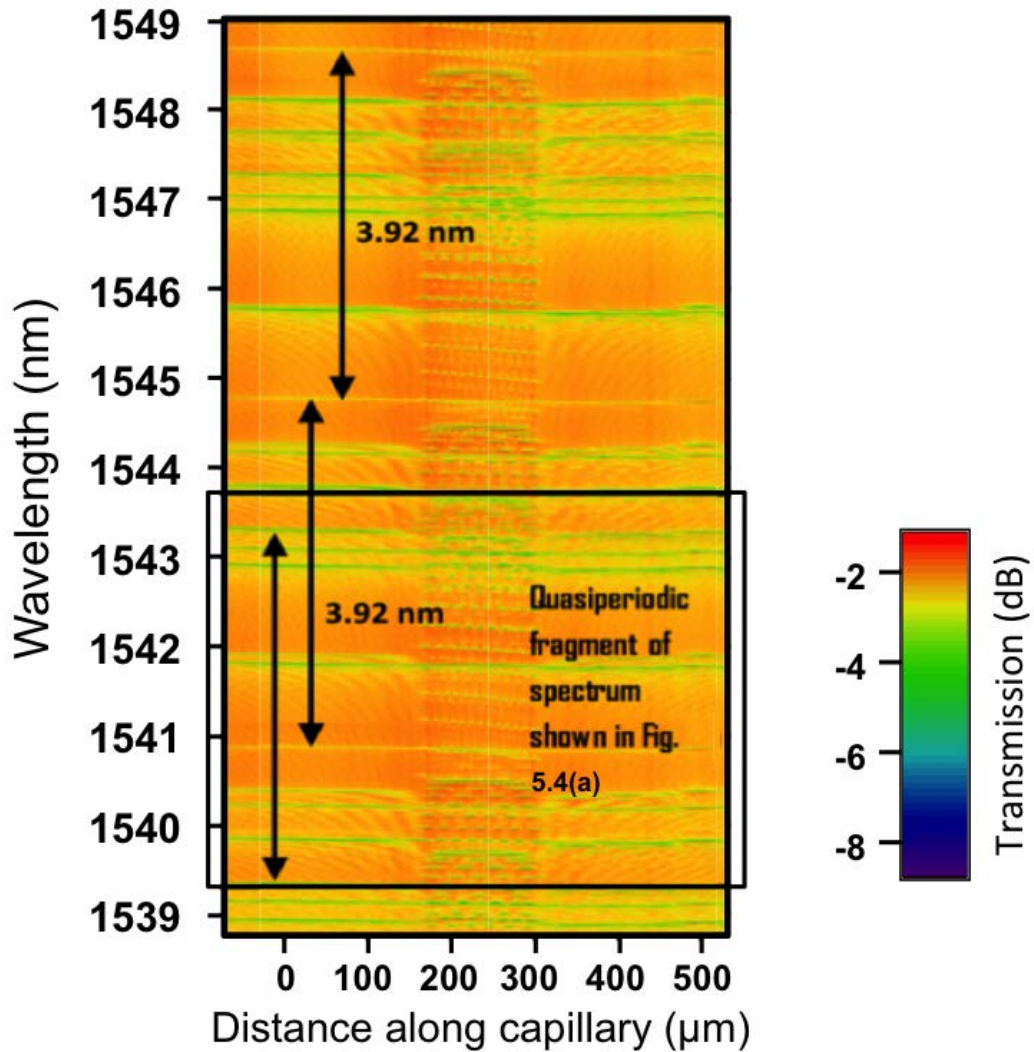


FIGURE C.1: The surface plot of the transmission power spectra in the bandwidth from 1539 nm to 1549 nm . The spectral (vertical axis) and spatial (horizontal axis) resolutions of the scan were 1.3 μm and 2 μm , respectively.

capillary has the same sub-micron scale as the penetration depth of the WGMs into the air. The latter fact justifies the model of rectangular resonator used in our simulations.

The experimental plot in Figure C.2 consists of magnified fragments of the experimental theoretical plots shown in Figure 5.4(a) and 5.4(b), respectively. The measured width of the droplet

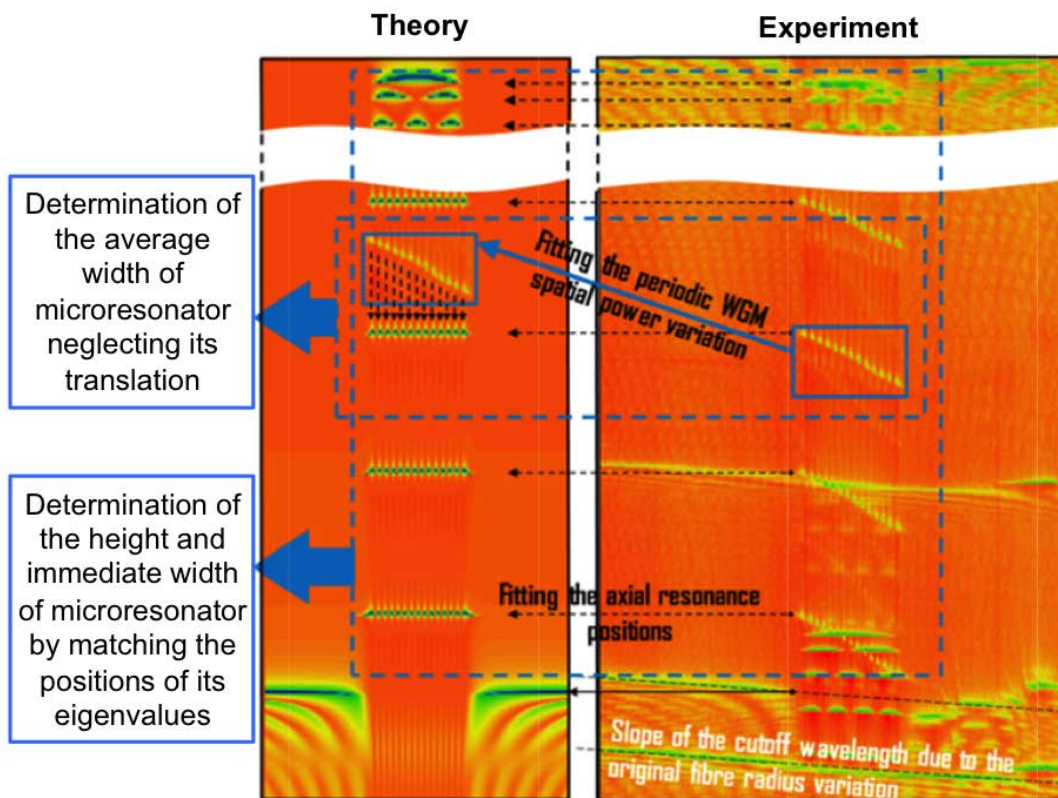


FIGURE C.2: Illustration of matching the theoretical and experimental data. The width of the resonator is determined by the comparison of single resonance pathways. The height of the resonator is determined by fitting the positions of all eigenvalues corresponding to the selected cutoff wavelength.

was first determined directly from the experimental Figure 5.4(a). Next, in a more accurate measurement, this width was determined from the comparison of numerical calculations of the transmission spectra using Eqs. (5.2)-(5.4) with the experimental data in Figure 5.4(a). The comparison method is illustrated in Figure C.2 We translated the square fragment of the experimental plot with an eigenvalue pathway inside outlined by a blue solid rectangular onto the theoretical plot of Figure C.2. The width of the resonator was determined by fitting the positions of the nodes of the experimental and theoretical plot indicated by vertical arrows. This method determines the final width of the resonator and does take into account its possible small displacement in the process of measurement.

Using the determined value of the resonator width as a first approximation, the cutoff wavelength shift (the resonator height) and immediate initial and finite resonator widths were found by

matching the theoretical and experimental positions of the resonator eigenvalues. This was performed for all the eigenvalues corresponding to the selected cutoff wavelength. The process of matching included both the variation of the resonator height and small adjustment of the resonator width. The remarkably accurate matching of these positions illustrated in Figure C.2 justified the rectangular model of the resonator. Notice that the values of the cutoff wavelengths shifts are independent of the droplet size and do not change in the process of measurement. For the examples considered in Figure 5.4, these values, equal to 3.85 nm and 0.7 nm, were first determined experimentally and then adjusted numerically in the process of fitting the wavelength eigenvalue positions. This fact allowed us to determine the actual initial and finite widths of the resonator and exclude the effect of its small translation. From the same figure, the slope of the cutoff wavelength due to the original fiber radius variation is 0.125 nm/mm. Thus, the total tilt of the cutoff wavelengths along the length $L = 130 \mu\text{m}$ of the droplet is as small as 0.017 nm and is neglected in our calculations.

C.2 Semiclassical Quantization Rule For WGMs in the Droplet-Induced Microresonator

If the WGM coupling to the capillary interior is ignored, the cutoff wavelengths λ_{mp}^{\pm} can be analytically determined for large mp azimuthal quantum numbers $m \gg p$ by the asymptotic equation (see e.g., Ref. [122]):

$$\lambda_{mp}^{\pm} \approx \frac{2\pi n_{cap} r_{ext}}{m} \left(1 + \zeta_p (2m^2)^{-1/3} + \frac{n_{cap}^{\pm 1}}{m(n_{cap}^2 - 1)^{1/2}} \right) \quad (\text{C.1})$$

where \pm corresponds to the TE/TM polarization and ζ_p are the zeros of the Airy function, $\zeta_0 = 2.338$, $\zeta_1 = 4.088$, $\zeta_2 = 5.521$, $\zeta_3 = 6.787$, and $\zeta_p \leq (\frac{3}{8}\pi(4p-1))^{2/3}$ for $p \gg 1$. From Equation C.1, at wavelength around $\lambda_0 = 1.54 \mu\text{m}$ the spectrum of cutoff wavelengths of our microcapillary is quasiperiodic along the azimuthal quantum number with the period of $\Delta\lambda = 3.95 \text{ nm}$. The latter value is an excellent agreement with the experimental $\Delta\lambda = 3.92 \text{ nm}$ found from Figure C.1. The cutoff wavelengths plotted in Figure 5.6 and found from Equation C.1.

The quantization rule for the WGMs localized in the region of the droplet $z_1 < z < z_2$ (Figure 5.3) is written as

$$\beta_{mp}^{(w)}(\lambda_{mpq}^{(w)})L = \pi(q + \kappa), \quad q = 0, 1, 2, \dots \quad (\text{C.2})$$

where $L = z_1 - z_2$ is the droplet length and $\kappa \sim 1$ is the parameter determined by matching solutions of Equation 5.3 at the droplet boundary [85]. Substitution of the expression for $\beta_{mp}^{(w)}(\lambda)$ given by Equation 5.2 into Equation C.2 yields the wavelength eigenvalues of the droplet induced microresonator:

$$\lambda_{mpq}^{(w)\pm} = \lambda_{mp}^{(w)\pm} - \frac{(q + \kappa)^2}{8n_{cap}^2 L^2} (\lambda_{mp}^{(w)\pm})^3 \quad (\text{C.3})$$

For large $q \gg 1$ we can ignore κ in Equation C.3 and the variation ΔL of microresonator length L is expressed through the variation $\Delta\lambda$ of eigenvalue $\lambda_{mpq}^{(w)\pm}$ by the equation

$$\Delta L = \frac{4n_{cap}^2 L^3}{q^2 \lambda_{mp}^3} \Delta\lambda \quad (\text{C.4})$$

used in the chapter 5.